SYNTHESIS AND CHARACTERIZATIONS OF NOVEL MAGNETIC AND PLASMONIC NANOPARTICLES

by

NAWEEN DAHAL

B.S., TRIBHUVAN UNIVERSITY, 1995
M.S., TRIBHUVAN UNIVERSITY, 1997

AN ABSTRACT OF A DISSERTATION

Submitted in partial fulfillment of the requirements for the degree

DOCTOR OF PHILOSOPHY

DEPARTMENT OF CHEMISTRY
COLLEGE OF ARTS AND SCIENCES

KANSAS STATE UNIVERSITY
Manhattan, Kansas

2010

Abstract

This dissertation reports the colloidal synthesis of iron silicide, hafnium oxide core-gold shell and water soluble iron-gold alloy for the first time. As the first part of the experimentation, plasmonic and superparamagnetic nanoparticles of gold and iron are synthesized in the form of core-shell and alloy. The purpose of making these nanoparticles is that the core-shell and alloy nanoparticles exhibit enhanced properties and new functionality due to close proximity of two functionally different components. The synthesis of core-shell and alloy nanoparticles is of special interest for possible application towards magnetic hyperthermia, catalysis and drug delivery. The iron-gold core-shell nanoparticles prepared in the reverse micelles reflux in high boiling point solvent (diphenyl ether) in presence of oleic acid and oleyl amine results in the formation of monodisperse core-shell nanoparticles.

The second part of the experimentation includes the preparation of water soluble iron-gold alloy nanoparticles. The alloy nanoparticles are prepared for the first time at relatively low temperature (110 ^{o}C). The use of hydrophilic ligand 3-mercapto-1-propane sulphonic acid ensures the aqueous solubility of the alloy nanoparticles. Next, hafnium oxide core-gold shell nanoparticles are prepared for the first time using high temperature reduction method. These nanoparticles are potentially important as a high κ material in semiconductor industry.

Fourth, a new type of material called iron silicide is prepared in solution phase. The material has been prepared before but not in a colloidal solution. The Fe_3Si obtained is superparamagnetic. Another phase β-$FeSi_2$ is a low band gap (0.85 eV) semiconductor and is sustainable and environmentally friendly.

At last, the iron monosilicide (FeSi) and β-$FeSi_2$ are also prepared by heating iron-gold core-shell and alloy nanoparticles on silicon (111) substrate. The nucleation of gaseous silicon precursor on the melted nanoparticles results the formation of nanodomains of FeSi and β-$FeSi_2$. A practical application of these nanoparticles is an important next step of this research. Further improvement in the synthesis of β-$FeSi_2$ nanoparticles by colloidal synthetic approach and its application in solar cell is a future goal.

SYNTHESIS AND CHARACTERIZATIONS OF NOVEL MAGNETIC AND PLASMONIC NANOPARTICLES

by

NAWEEN DAHAL

B.S., TRIBHUVAN UNIVERSITY, 1995
M.S., TRIBHUVAN UNIVERSITY, 1997

A DISSERTATION

Submitted in partial fulfillment of the requirements for the degree

DOCTOR OF PHILOSOPHY

DEPARTMENT OF CHEMISTRY
COLLEGE OF ARTS AND SCIENCES

KANSAS STATE UNIVERSITY
Manhattan, Kansas

2010

Approved by:

Major Professor
VIKTOR CHIKAN

Copyright

Abstract

This dissertation reports the colloidal synthesis of iron silicide, hafnium oxide core-gold shell and water soluble iron-gold alloy for the first time. As the first part of the experimentation, plasmonic and superparamagnetic nanoparticles of gold and iron are synthesized in the form of core-shell and alloy. The purpose of making these nanoparticles is that the core-shell and alloy nanoparticles exhibit enhanced properties and new functionality due to close proximity of two functionally different components. The synthesis of core-shell and alloy nanoparticles is of special interest for possible application towards magnetic hyperthermia, catalysis and drug delivery. The iron-gold core-shell nanoparticles prepared in the reverse micelles reflux in high boiling point solvent (diphenyl ether) in presence of oleic acid and oleyl amine results in the formation of monodisperse core-shell nanoparticles.

The second part of the experimentation includes the preparation of water soluble iron-gold alloy nanoparticles. The alloy nanoparticles are prepared for the first time at relatively low temperature (110 ^{o}C). The use of hydrophilic ligand 3-mercapto-1-propane sulphonic acid ensures the aqueous solubility of the alloy nanoparticles. Next, hafnium oxide core-gold shell nanoparticles are prepared for the first time using high temperature reduction method. These nanoparticles are potentially important as a high κ material in semiconductor industry.

Fourth, a new type of material called iron silicide is prepared in solution phase. The material has been prepared before but not in a colloidal solution. The Fe_3Si obtained is superparamagnetic. Another phase β-$FeSi_2$ is a low band gap (0.85 eV) semiconductor and is sustainable and environmentally friendly.

At last, the iron monosilicide (FeSi) and β-$FeSi_2$ are also prepared by heating iron-gold core-shell and alloy nanoparticles on silicon (111) substrate. The nucleation of gaseous silicon precursor on the melted nanoparticles results the formation of nanodomains of FeSi and β-$FeSi_2$. A practical application of these nanoparticles is an important next step of this research. Further improvement in the synthesis of β-$FeSi_2$ nanoparticles by colloidal synthetic approach and its application in solar cell is a future goal.

Table of Contents

List of Figures

List of Tables

Acknowledgements

First of all, I would like to express my sincere gratitude to my doctorate advisor, Professor Viktor Chikan, at Kansas State University, for the honor to work under his guidance. I am really proud of being the first PhD student graduating from his group. I greatly appreciate the freedom opportunity he has given me to pursue my research in my own way. It is noteworthy to mention that I decided to pursue my doctorate degree in Chemistry at KSU due to his priceless guidance and encouragement that have made my life easier and my research better.

It is my pleasure and honor to thank my Graduate Committee Members: Professor Christopher M. Sorensen, Professor Stefan Bossmann, Professor Paul Smith, and Professor Mohammad Hosni. Thank you very much for your valuable time, suggestions and discussions. It's my pleasure to thank Professor Mohammad Hosni to be the outside chairperson of my graduate committee. A special thanks to Professor Christer B. Aakeroy and other chemistry faculty members for the opportunity to come to K-State and attend graduate school. I am very much grateful and want to thank Professor Kenith J. Klabunde for his inspiration in the field of nanotechnology. A special thanks to all group members of the Chikan group during my time here at KSU; Christopher Tuinenga, Pinar Dagatepe, Raj Kumar Dani, Santanu Roy and Brett Vaughn.

I sincerely would like to thank Earline Dikeman for her help in teaching courses. Thank you to all ladies in the office for helping with all kinds of things! Thank you very much Richard Bachamp, Ron Jackson, Tobe Eggers and Jim Hodgson for fixing my equipment whenever needed!. Thank your very much Agnas Chikan for your valuable time for proof-reading this document. It will just less to thank my wife, Ranjana Ojha (Dahal), for her everlasting love and moral support to

achieve this goal. Thanks to my daughter, Niharika Dahal, and Son, Nirab Dahal for making me as a cheerful dad! Lastly, I also would like to thank my father and mother (Krishna Prasad Dahal & Dhana Maya Dahal) for their unlimited love, encouragement and support to come to the United States of America for advanced degree.

Dedication

To my parents

(Mother Dhana Maya Dahal and father Krishna Prasad Dahal)

To my wife

Ranjana Ojha (Dahal)

Preface

Nano is just not small!! (1 nm = $1x10^{-9}$ m)

CHAPTER 1 - Introduction

Importance of nanoparticles and nanochemistry

A new direction of synthetic chemistry to produce new type of matter beyond the atoms and molecules started in the early 1990s. Neither quantum chemistry nor classical physics theories apply to this new type of matter. A nanoparticle is a term used more generally for a solid particle in the 1-1000 nm range that could be crystalline, an aggregate of crystallite, or a single crystallite and possesses properties different from either atoms or the bulk materials.[1] In the early days, synthetic methods focused on creating nanoscale building blocks of any compositions. For example the combination of inorganic, organic and polymeric materials can produce new ones with different properties from their constituents. In these efforts, chemistry is used to achieve nanoscale-level control of the size, shape, surface structure, charge, and functionality of these building blocks at nanoscale. Continuous efforts have been made to prepare hierarchical structures of different functions to accomplish a desired goal. The important aspect of nanochemistry lies on the effective ways of rebuilding known materials in nanoscale level with desired properties and applications.[2-4] Currently, a major focus of this field is to synthesize nanoparticles of new materials with understanding of the theory of crystallization and dispersibility in solution. While controlling shapes, sizes and monodispersity of nanomaterials is another purpose.

The advancement of nanochemistry is highlighted by its wide range of applications in different branches of physics, chemistry and biology.[5-21]Nanoparticles of metals, semiconductor or magnetic materials possess very different properties from their bulk counterpart. Metals like gold, silver and copper show plasmonic band in the visible region of the electromagnetic

spectrum in nano from. The core-shell or alloy nanoparticles containing one of these metals also show the plasmonic behavior. Similarly, the magnetic property is changed from ferromagnetic to superparamagnetic in nano form as in the case of iron, cobalt, nickel, iron oxides and iron silicide nanoparticles. Quantum confinement, a special feature of semiconductor material, becomes dominant in a semiconductor material when the material size is smaller than exciton Bohr radius. The following paragraphs explain in brief the plasmonic, magnetic and semiconducting properties associated with the nanoparticles and discussed in this dissertation.

Plasmonic nanomaterials

Electrodynamical effects and the modification of the dielectric environments produce the optical effects in metallic nanostructures.[22] As a result of these optical effects, a new type of resonance called plasmon or surface plasmon resonance localized between the metal nanostructure and the surrounding dielectric produces an enhanced electromagnetic field at the interface. The plasmon oscillations localize between the metal nanostructures and the surrounding dielectric medium are referred to as localized surface plasmons. These bands are excited by absorption of light in the nanoparticles. The specific wavelengths of light absorption producing plasmon oscillations are called surface plasmons bands (SPB) or simply plasmon bands.[23] The new growing field of research dealing with light-metal interactions is known as plasmonic.[24, 25] The miniaturized plasmonics materials have potentially applicable in photonic devices, sensors, and photonic circuits as well as in a medical diagnostics and therapeutics.[24-30]

The wavelength of the absorption peak maximum of the surface plasmon band depends on the shape, size, and dielectric environment surrounding the particles.[31] If the size of plasmonic nanoparticles is significantly smaller than the wavelength of light, light absorption will take place within a narrow wavelength range. In case of subnanometer metal nanoparticles,

the surface plasmon band usually does not shift but the broadening of plasmonic peak is observed. On the other hand, large plasmonic nanoparticles exhibit the red shift.[32, 33] Rod-shaped plasmonic materials usually show two surface plasmon bands due to longitudinal and transverse oscillation of free electrons along to the long axis of the rod. Transverse mode resonance is very similar to that of spherical particles but the longitudinal mode resonance which is significantly red shifted is determined by the aspect ratio of the rod.[23] The origin of these shifts is not due to quantum confinement. However, the quantization derived from the confinement does affect the conductive properties of the metal. For instance, Schultz *et al.* studied the effects of shape on the spectral response of individual silver nanoparticles.[22, 34] They concluded that the triangular shaped particles appear mostly red, pentagonal nanoparticles appear green, and spherical nanoparticles appear blue. Jin *et al.* induced a shape transformation from silver nanospheres to nanoprisms, and they also observed a spectral shift from blue to red.

The general requirement for the use of surface plasmon resonance is that the metal should have the conduction band electrons resonating with light at a suitable wavelength. Gold and silver are the best choices because they display surface plasmon resonance at the visible wavelength range. At these wavelengths the optical properties of the metal nanoparticles are described by complex wavelength dependent dielectric constant. When a plasmonic metallic nanoparticle is exposed to the photon of incident frequency, the nanoparticle surface produces oscillating dipoles along the field direction where the electrons are driven to the surface of the nanoparticles as shown in Figure 1-1.[35]

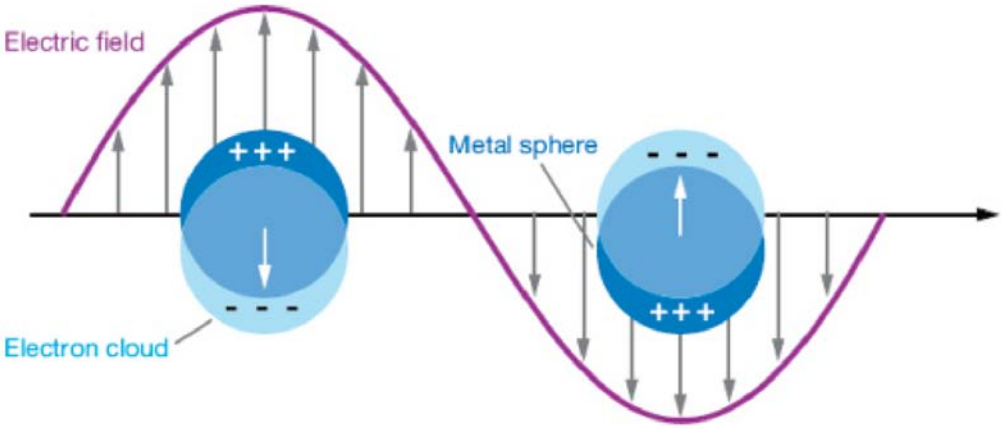

Figure 1-1 Schematics of plasmon oscillation in a metal nanosphere.[33]

This dipolar type displacement is applicable for the particle diameter'd' is much smaller than the incident wavelength of light λ and it produces an extinction coefficient k_{ex}. According to the classical Mie theory,[36] the extinction coefficient is the measure of absorption and scattering strength and is given by the following equations[33]

$$k_{ex} = \frac{18\pi NV\varepsilon_h^{3/2}}{\lambda} \frac{\varepsilon_2}{[\varepsilon_2 + 2\varepsilon_h]^2 + \varepsilon_2^2} \qquad (1)$$

In equation (1), λ is the wavelength of light, and ε_h is the dielectric constant of the surrounding medium. The dielectric constant of the metal is given by the equation $\varepsilon_m = \varepsilon_1 + i\varepsilon_2$, where ε_1 and ε_2 are the real and imaginary part dielectric constants of the metal and depend upon the frequency of light (ω). If ε_2 is small or weakly dependent on ω, the absorption maximum corresponding to the resonance condition is produced. A surface plasmon resonance absorption is produced at frequency ω when $\varepsilon_h = -2\varepsilon_h$ is fulfilled. The size dependence of surface plasmons is originated from the size dependence of the dielectric constant of metal. There is a red shift in surface plasmon bands with increasing size because of electromagnetic retardation. Kreibig and

Vollmer explained that this is due to the polaritonic red-shift and the various phases of light across particles with different sizes. And they also found that the width of the surface plasmon increases with size. This is caused by radiation damping and is explained by Drude model.[33]

The alloy and core-shell nanoparticles are referred to as heterostructures nanoparticles. The change of surface plasmon bands on those structures is dramatic, compared to single component nanoparticle systems. The optical property of these nanoshells is governed by the plasmon resonance and is shifted in much longer wavelength due to large effect of core dielectric constant.[37] When the core size is kept constant and the thickness of the shell is varied a change in the surface plasmon band position can be observed.

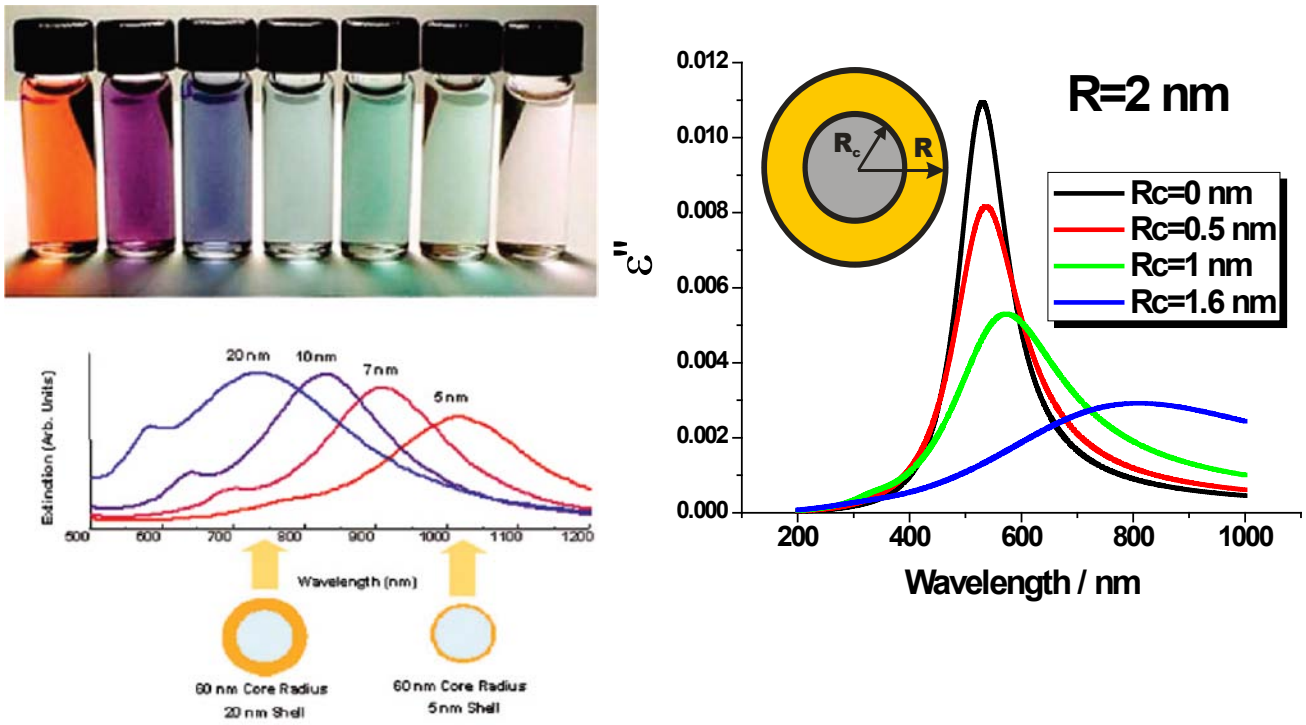

Figure 1-2 (a) Visual demonstration of the tunability of metal nanoshells (top), and optical spectra of Au shell-silica core nanoshells (the labels indicate the corresponding Au shell thickness).[35] (b) Calculated plasmon band shift of iron oxide-gold core shell nanoparticle based on core radius (right).

In other words, while changing the radius of the core it will also change the thickness of the shell as show in Figure 1-2a. The calculation is based on the dielectric constant of core & shell and their radius, which shows the red shift of the surface plasmon peak position with increasing core radius. The theoretical calculation shows approximately 200-250 nm red shifting of plasmon band upon decreasing the shell thickness to 0.4 nm from 1.5 nm. Manipulating the shell thickness is essential to use core-shell nanoparticles as a heater for lasers induce hyperthermia. The iron-gold core shell is effective for this purpose because of high absorption of laser and fast electron relaxation caused by a thin shell. In addition, commercially convenient laser frequency up to 800 nm can be manipulated as shown in Figure 1-2 b by controlling the shell thickness or core radius of the core-shell nanoparticles. When the thickness of the shell is increased, the plasmon band shifts to the shorter wavelength similarly if thickness decreases the surface plasmon band shifts to the longer wavelength. By varying the metallic shell thickness it is possible to obtain a broad spectral range of surface plasmon bands.[37] Figure 1-2 clearly indicates the experimental plasmon resonance spectra of different shell thickness of gold on a silica core of 60 nm radius.[37] In this dissertation iron-gold core-shell, iron-gold alloy and hafnia-gold core shell nanoparticles are presented as model systems.

Magnetic nanomaterials

The lodestone compass, the first invention utilizing magnetic materials, was critical in aiding 12th century explorers to navigate across unexplored parts of the world. Magnetic nanoparticles are considered as a miniature counterpart of lodestone compass that acts as a navigator guide for researchers to better understanding the inside of living organism. It is interesting, that many of the migratory animals and some microbes posses magnetic nanoparticles that are utilized as a natural biomagnetic compass.[38] The recent advancement in colloidal synthetic chemistry

established easy methods to synthesize highly crystalline and monodisperse artificial magnetic nanoparticles. Over the past decade, a wide range of magnetic nanoparticle with several composition and structures has been synthesized by using wet chemical methods.[39-45] The most common of these materials are the iron oxides (Fe_2O_3 and Fe_3O_4), known for their high magnetic moments and biological compatibility, and their corresponding ferrites (e.g.,$MnFe_2O_4$ and $CoFe_2O_4$).[39, 43] Metals and alloys such as Mn_3O_4, Fe, Co, Ni, FePt and FePd are less commonly employed, in part because of their rapid oxidation in air or potential for cytotoxicity.[46, 47] There are several challenges associated with the most widely used magnetic iron oxide nanoparticles. For example, different types of magnetic behavior exist in iron oxide depending on its crystal structure and size. When magnetic iron oxides are used as the material for magnetic resonance (MR) contrast agents, they can exhibit either ferromagnetism or superparamagnetism.[48] Superparamagnetic materials are generally preferred for MR contrast agents, as they exhibit relaxation effects that are generally stronger per millimole of iron than ferromagnetic particles.

Many novel and interesting phenomenon can be observed in nanoscale magnetic materials that are different from their bulk counterpart. The fundamental magnetic properties such as coercivity, magnetic susceptibility can be altered according to shape size and composition as represents in Figure 1-3.[49] As a result the scaling relationships can be used to tune magnetism from ferromagnetic regime (very high magnetic energy product, BH_{max}) to the superparamagnetic regime (zero coercivity in nanoscale regime).[50, 51] Therefore, the nanoscaling laws of engineered magnetic nanoparticles are important not only to understand the behavior of existing materials, but also to develop novel materials with superior properties.

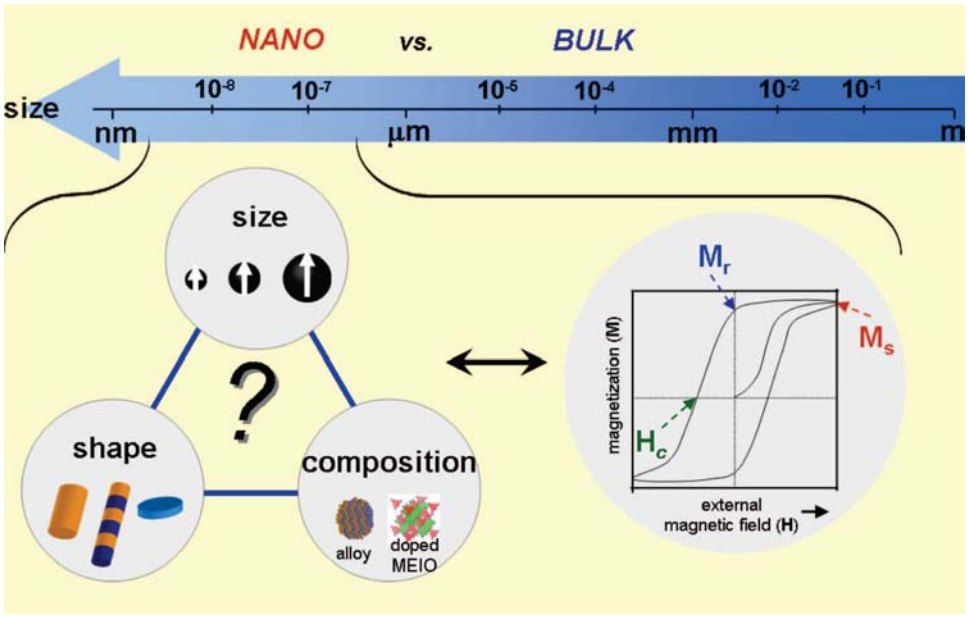

Figure 1-3 In nanometer scale, parameters such as size, shape, composition, and magnetocrystalline anisotropy strongly affect the magnetism (e.g., coercivity, mass magnetization, remanence) of nanoparticles.[50]

One of the interesting size-dependent phenomena of nanoparticles is superparamagnetism. The magnetic anisotropic energy barrier from a spin-up state to spin-down state of the magnet is proportional to the product of the magnetic anisotropic constant (K_u) and the volume (V) of the magnet. While bulk materials have magnetic anisotropic energies that are much larger than the thermal energy (kT) (Figure 1-4 (blue line)), the thermal energy of the nanoparticle is sufficient to readily invert the magnetic spin direction, although it is insufficient to overcome the spin–spin exchange coupling energy (Figure 1-4 (red line)). Such magnetic fluctuation leads to a net magnetization of zero, and this behavior is called superparamagnetism.

The transition temperature from ferromagnetism to superparamagnetism is referred to as the blocking temperature (T_b) and is defined by the relationship $T_b = K_uV/25k$.[49]

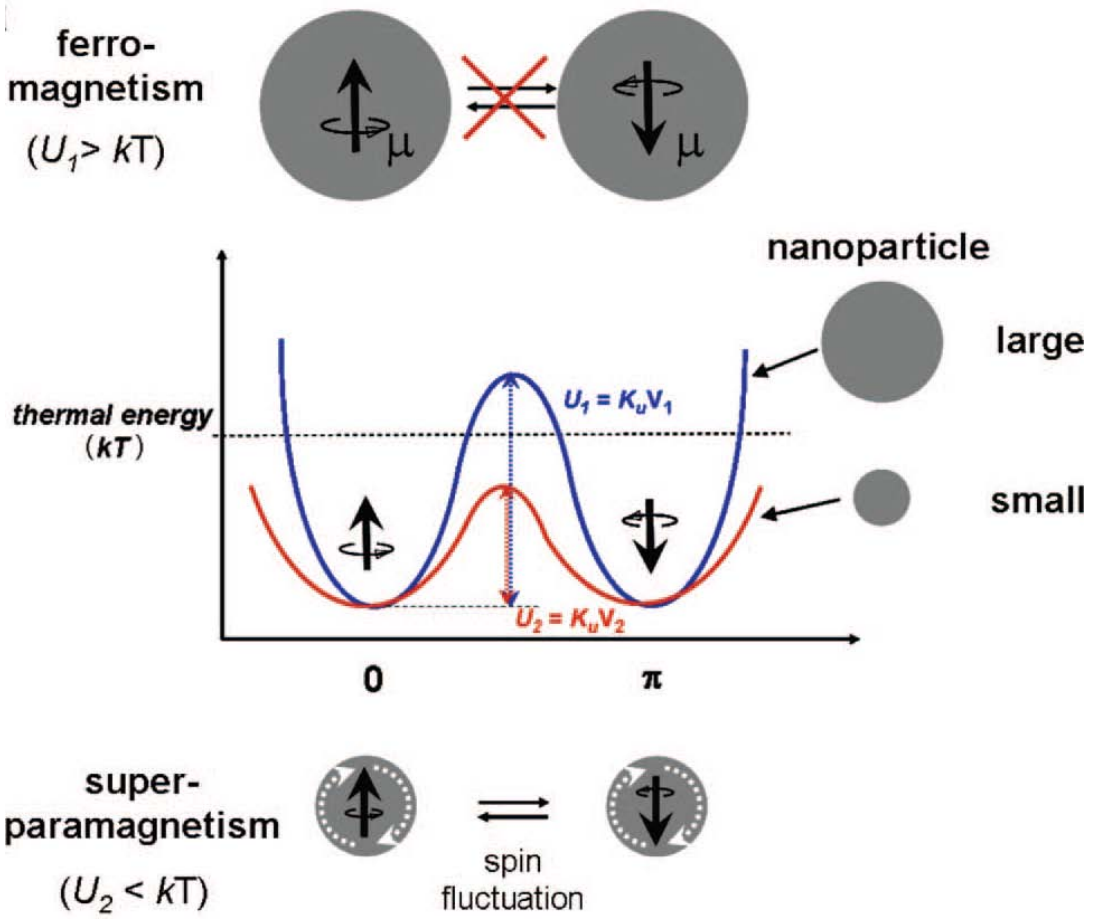

Figure 1-4 Nanoscale transition of magnetic nanoparticles from ferromagnetism to superparamagnetism: (a) energy diagram of magnetic nanoparticles with different magnetic spin alignment, showing ferromagnetism in a large particle (top) and superparamagentism in a small nanoparticle (bottom).[53]

The interest in core-shell and alloy type of hybrid magnetic and plasmonic material such as iron-gold, iron oxides-gold, cobalt- gold is increasing. There are quite a few examples in the

literature. The important features of these magnetic nanoparticles are the surface character of gold shell and the high magnetic moments of iron, iron oxide or cobalt core. Most importantly, gold coating on oxidation susceptible iron or iron oxides preserves the magnitude of magnetic moments. The magnetic moment of bulk iron is 172-218 emu/g and that of iron oxide (Fe_3O_4) is 64-84 emu/g.[52] Therefore, the thickness of the gold shell has some effect on the induced moment distribution in the gold shells; but has little effect on the magnetic moment of the iron core. The large magnetic moment of iron core is very well retained.[52] This is a desirable property in magnetic drug delivery and hyperthermia treatment. The gold coating improves the biocompability and provides a platform for magnetic particles to be functionalized. Because of these reasons, a new synthetic strategy by manipulating the existing reverse micelles and two phase reduction system have been utilized to prepare the iron-gold, core shell, and iron-gold alloy nanoparticles. The preparation of hafnium oxide-gold core shell nanoparticles is also presented as a potential plasmonic and high-k dielectric material. The details of the synthesis and characterizations methods are presented in chapter 2, 3, & 4 of this dissertation. Synthesis and characterization of a new class of ferromagnetic material (Fe_3Si) nanoparticles that show less reactivity compared to iron oxide in biological environment is also presented in chapter 5.

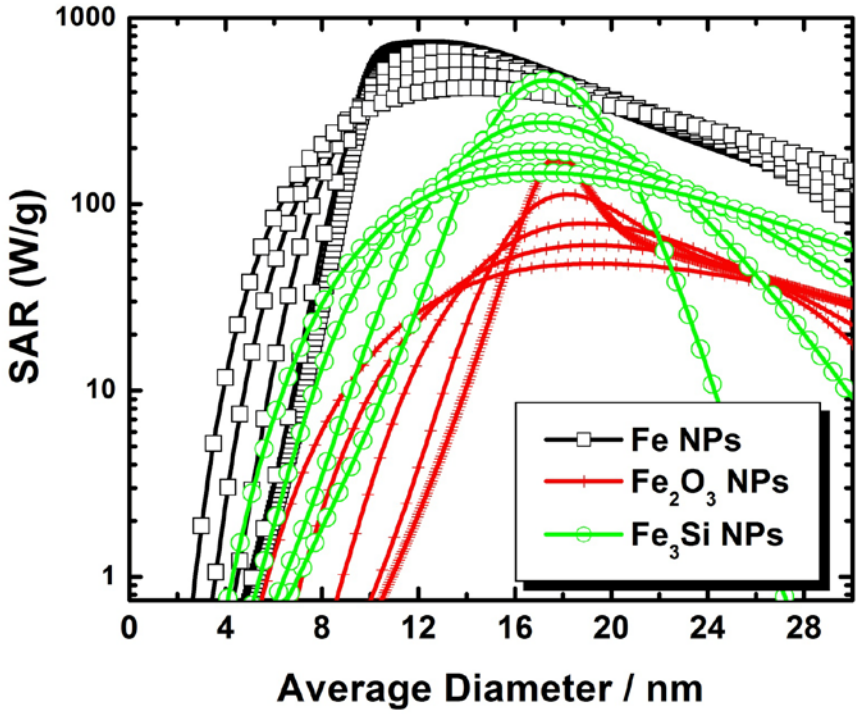

Figure 1-5 shows the theoretical cartoon showing the heating efficacy among pure iron, ironoxide (Fe_2O_3), and iron silicide (Fe_3Si) nanoparticles.

A novel synthetic method is developed to prepare the superparamagnetic iron silicide (Fe_3Si) nanoparticles in solution phase in our lab and this is reported first time in the literature. The nanoparticles are assumed to be nontoxic, cheap and environmentally friendly. The material is made from most abundant elements in the earth crust. Because of their superparamagnetic and non-toxic nature, the particles can be used as effective heater for the hyperthermia process. The heating efficiency of the nanoparticles is expressed in terms of specific loss power (SLP) also called the specific absorption rate (SAR) which is defined as the thermal power dissipation divided by the mass of magnetic material.[53]

Figure 1-5 shows that iron nanoparticle have the highest SAR value and are the best heater for hyperthermia. However, highly pyrophoric and oxidative nature of iron nanoparticles makes them difficult to handle. On the other hand, iron oxides nanoparticles are the most frequently used nanoparticles for hyperthermia and targeted tumor treatment. There are number of problems associated with iron oxides. Some of the examples are: iron oxide undergoes aggregation in physiological condition and blood stream, susceptible for opsonization, usually needed a large amount 1 mg to 25 mg of Fe/Kg, and internalization of iron oxide by macrophages and loosing the specificity and sensitivity are the major challenges.[21, 54] The theoretical calculation (Figure 1-5) shows that the much less (~ factor of two) of iron silicide is required compared to iron oxide for effective heating in the presence of A-C magnetic field. Iron silicide nanoparticles (Fe_3Si) appear to be better than iron oxide. Therefore, designing, and controlling the synthetic conditions to obtain narrow size distribution of iron silicide (Fe_3Si) nanoparticles is important part of this dissertation.

Semiconducting nanoparticles /quantum dots

The definitions of nanoparticles, nanocrystals or quantum dots are often ambiguous. Nanocrystal is referred to as well-defined crystalline material and is a single crystal in the nanometer size range, whereas nanoparticle is a term used more generally for a solid particle in the 1-1000 nm range that could be crystalline, an aggregate of crystallite, or a single crystallite.[23] A quantum dot is a nanoparticle in the size range of 1-10 nm that exhibits properties of quantum confinement. When a system moves from bulk to nanocrystals to quantum dots, drastic changes can be seen in the optoelectronic properties of the materials. Quantum dots that exhibit quantum confinement effect are zero dimensional and the density of states (DOS) leads to discrete set of allowed energies. Confinement of all three dimensions leads to discrete states with a complete

loss of periodic symmetry, as opposed to continuous bands seen in bulk system. In some sense, nanocrystals and quantum dots are much more difficult to model, because it is no longer possible to simplify the problem using the periodicity of the structure, since the wave functions are extending beyond and thus interact with the physical boundaries of the system. Here the states at the boundary (edge effects) play an enormous role in determining the electronic properties.[55] However, one of the best models for nanocrystals was proposed by L.E. Brus to simplify the electronic properties of nanoparticles and the quantum confinement effect into a single equation. The energy of the first exciton state of the nanocrystal, where E_{gap} is the bandgap associated with the bulk system is given by

$$\Delta E_{np} = E_{gap} + \frac{h^2}{8\mu_{eh}R^2} - \frac{1.8e^2}{4\pi\varepsilon\varepsilon_0} \text{ ---------- (1)}$$

where μ_{eh} is the reduce mass of electron and hole and is given by the equation

$$\frac{1}{\mu_{eh}} = \frac{1}{m_e^*} + \frac{1}{m_h^*} \text{ ---------- (2)}$$

where m_e^* and m_h^* are the effective mass of electron and hole. The second term that includes R^2 dependence, is a confinement term, and originates from solving the Schrödinger equation just as you would for the particle in a box model. The third term is a coulombic term, sometimes referred to as the free energy term accounts for the increase energy of attraction of the electron-hole pair. Smaller terms such as the exchange term are often ignored unless exciton fine structure is studied. It is easy to see that as the nanocrystal grows smaller in size the second term begins to dominate. This term is mainly responsible for the absorption and emission of photons with increased energy. As R grows larger both terms approaches zero. When the higher order terms are neglected in equation 1, only the bandgap equivalent to bulk material is left. Many semiconducting materials show this property and help to tune the band gap based on their sizes.

For example CdSe, CdTe, InP, GaAs, CdS, GaN are some commonly used semiconductors. Many of these materials absorb only in a small region of solar energy spectrum as shown in Figure 1-6b and are toxic and carcinogenic. There is no effective and safe recycling study of these materials so far. As an alternative material β-$FeSi_2$ nanoparticles could take an important role. The quantum confinement model can also be applied to smaller size β-$FeSi_2$ nanoparticles and its band gap can be tuned all the way from visible to infrared. Figure 1-6b shows the complete solar spectrum range covered by most common semiconductor nanoparticles. Upon quantum confinement, the β-$FeSi_2$ nanoparticles can cover a wide range in solar spectrum and band gap also can change from indirect to direct transition.[56] Additionally, iron silicides are non-toxic; acquire high temperature stability; and ecologically friendly material. The calculation of the abundance of the most common semiconductor in unit of Kg/ per 1000 Kg of the earth crust shows that the β-$FeSi_2$ is the most sustainable materials after silicon compare to other common semiconductors as shown in Figure 1-6a. Therefore, development of this material in control synthetic conditions could replace the highly toxic and less sustainable semiconductors in terms of relative abundance in earth crust like CdSe, CdTe, InP, GaAs, CdS, GaN etc. Therefore, a key issue is to address the technology sustainability of solar energy conversion materials, specifically in terms of energy and environmental impacts, availability, toxicity and recyclability. As explained previously, the availability of β-$FeSi_2$ is almost five orders greater than the common semiconductors. These features support that β-$FeSi_2$ is ideal materials for optical fiber communication, infrared detectors, thermo electronic, and photovoltaic applications.[57-61] However, significant efforts are needed for the optimization of growth processes in the nanometer size range. None of the conventional methods are able to produce β-$FeSi_2$ in desirable size, shape; that is independent from a silicon substrate. We believe the synthetic methods

presented in this dissertation in chapter 5 and 6 add a new avenue for the synthesis of iron silicide nanoparticles in colloidal solution.

Furthermore, the interest in nanostructure iron silicide is not only by its potentially important roles as robust, stable, environmentally green, and inexpensive material,[62, 63] but also could take a critical role in the next generation of nanomaterials with a wide range of potential applications in photovoltaic and semiconductor industry. The bulk phase diagram of iron and silicon shows at least five known iron silicide compounds (Fe_3Si, Fe_5Si_3, FeSi, β-$FeSi_2$, and α-$FeSi_2$).[64] We are particularly interested in the synthesis of the semiconducting β-$FeSi_2$ and ferromagnetic Fe_3Si nanoparticles. Electrons (holes) or phonon can be confined in nano-crystallites β-$FeSi_2$ that influence on the electron conduction of grown structures, light absorption and emission. β-$FeSi_2$ is a p-type direct band gap semiconductor the band gap of 0.85 eV[65-67]. The holes concentration in β-$FeSi_2$ is larger than 10^{18} cm^{-1}. β-$FeSi_2$ generates very high resonance absorption coefficient due to Fe 3d electron-LO phonon interaction.[65-67] The optical absorption coefficient is higher than 10^5 cm^{-1} at 1eV, which is 50 times larger than that of crystalline silicon.[68, 69] The large absorption coefficient of β-$FeSi_2$ makes this material an ideal candidate to be used in solar cells.

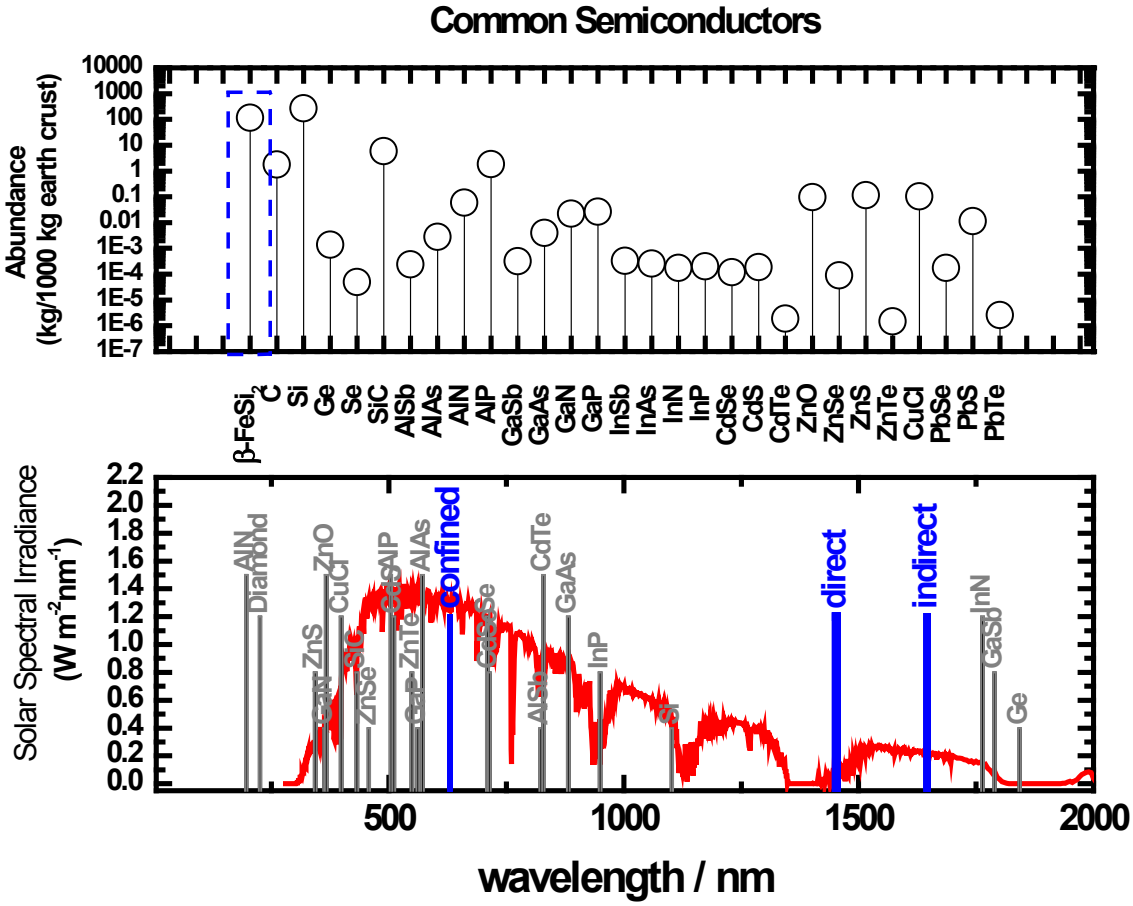

Figure 1-6 (a) A graph of the abundance of most common semiconductors on earth crust in terms of mass of common semiconductor in Kg per 1000 Kg earth crust. (b) Graph of the solar spectrum along with the bulk bandgaps of the most common semiconductors.

Nucleation and growth in colloidal synthesis

Control over the size and shape of nanoparticles is the most important aspect of the solution-based colloidal synthesis. Colloidal synthesis is cheap and utilizes a simple set of equipments and chemicals but still capable of producing high quality materials.[70] The colloidal synthesis generally involves several consecutive steps including nucleation, growth and isolation of the particles to achieve the desired size from a reaction solution. Narrow size distribution of the particles is achieved by using different techniques either by temporarily separating the nucleation from the growth or by the steady heating of the reaction mixture.[71] When the precursor molecules are rapidly injected into the hot solvent, that lead to subsquent temperature drop and helps to separate the nucleation step from the growth step.[70] Nucleation and growth of nanoparticles occur in the solution phase in the presence of surfactant molecules. The surfactant molecules play a key role to determine the kinetics of nucleation and growth.[71, 72] For example when nucleation is too fast the solution produces bulk material and when nucleation is too slow, the reaction simply produces small molecular clusters. Therefore, the balancing of these intrinsically different mechanisms is challenging. This problem is addressed empirically by choosing the 'good' combination of surfactants, solvents, reaction conditions and concentration of precursor molecules. Achieving a reproducible synthetic condition with desired shape, morphology, size and composition is very important to implement a material for practical applications.

In our synthetic approach as used in this dissertation, several reducing agents such as sodium borohydride, glycol, diol, amine, and superhydride are used in the presence of ligands and surfactant molecules. Most of the synthesis is carried out in inert atmosphere of either argon or nitrogen. In many of the reactions refluxing is carried out in high boiling point solvent to

provide a wide window of reaction temperature. Heating is applied in between 200-300 ^{o}C to anneal the defects in crystalline lattice and form highly crystalline nanoparticles.[71, 72] Different strategies are applied to tune the size of the nanoparticles during synthesis. Usually, the growth of the metal nanoparticles takes place rapidly and difficult to terminate the reaction at a desired state.[73] Better reaction controls can be obtained if the particles size is adjusted by growing the small seed nanoparticles and adding finite amounts of precursor molecules. When the precursor concentration is constant, the fast nucleation provides more nuclei and produce smaller nanoparticles. On the other hand, slow nucleation provides low concentration of seeds consuming the same amount of precursor resulting in large nanoparticles. The balance between the nucleation and growth is challenging as the nucleation has higher activation barrier than the growth process.[74] In general, increasing reaction temperature allows obtaining smaller nanoparticles. The other factors that help to tune the size of the nanoparticles are physical and chemical properties and concentration of capping agent, surfactant, molar concentration of precursors, and duration of particles growth. Semiconductor nanoparticles in colloidal solution usually grow via Ostwald ripening process.[75] In Ostwald ripening, the largest particles in solution grow at the expense of smaller ones resulting in an increase in the size of the nanoparticles over time.

Bringing together components of intrinsically different functionality constitutes a powerful route to creating novel functional materials with synergetic properties found in neither of the constituents. Some new aspect of synthetic chemistry is described in this dissertation based on solid state properties and solution dispersibility for intrinsically different materials. Solution dispersibility is a necessary prerequisite to study the solid state properties of colloidal nanocrystal. Ligand chemistry is key to understand the solution-solid properties of nanocrystal.

Several ligands and their combination are applied for better control of size and dispersibility of the nanoparticles. Right choices of reducer, temperature and concentration of precursor and ligand have been tested for the synthesis of several nanoparticles. High boiling point solvents are used in synthesis; as better quality nanoparticle can be obtained at high temperatures. At high temperature, the surfactants molecules are dynamically adsorbed to the surface of growing crystal. The process helps to stabilize the particles in solution and mediating their growth. The surfactants can also be exchanged with other organic molecules with different functional groups and polarity. Different way of addition of reducing agents plays a significant role to obtain a desired form of nanoparticles. For example, stepwise additions of sodium borohydride in preparation of gold iron core-shell nanoparticles lead to form the alloy nanoparticles due to coarsening of the shell. This dissertation is essentially focus on the synthesis and detail characterizations of plasmonic iron-gold, hafnia-gold core shell, iron-gold alloy, & magnetic (Fe_3Si) and semiconducting (β-$FeSi_2$) iron silicide nanoparticles. The quality of the nanoparticles is examined based on size, purity, morphology, and crystal structure.

References:

1. Klabunde, K. J., *Nanoscale Material in Chemistry*. John wiley & sons: 2001; Vol. 1.
2. Prasad, B. L. V.; Sorensen, C. M.; Klabunde, K. J., *Chem. Soc. Rev.* **2008**, 37, (9), 1871-1883.
3. Prasad, B. L. V.; Stoeva, S. I.; Sorensen, C. M.; Klabunde, K. J., *Chem. Mater.* **2003**, 15, (4), 935-942.
4. Prasad, B. L. V.; Stoeva, S. I.; Sorensen, C. M.; Klabunde, K. J., *Langmuir* **2002**, 18, (20), 7515-7520.
5. Huang, H.; Yin, S. C.; Kerr, T.; Taylor, N.; Nazar, L. F., *Adv. Mater.* **2002**, 14, (21), 1525-1528.
6. Achermann, M.; Petruska, M. A.; Kos, S.; Smith, D. L.; Koleske, D. D.; Klimov, V. I., *Nature* **2004**, 429, (6992), 642-646.
7. Bessel, C. A.; Laubernds, K.; Rodriguez, N. M.; Baker, R. T. K., *J. Phys. Chem. B* **2001**, 105, (6), 1115-1118.
8. Brien, P. G. O.; Kherani, N. P.; Zukotynski, S.; Ozin, G. A.; Vekris, E.; Tetreault, N.; Chutinan, A.; John, S.; Mihi, A.; Míguez, H., *Adv. Mater.* **2007**, 19, (23), 4177-4182.
9. Dresselhaus, M. S.; Chen, G.; Tang, M. Y.; Yang, R. G.; Lee, H.; Wang, D. Z.; Ren, Z. F.; Fleurial, J. P.; Gogna, P., *Adv. Mater.* **2007**, 19, (8), 1043-1053.
10. Christian, J. W., *The Theory of Transformation in Metals and Alloys*. 1975.
11. Goldberger, J.; Fan, R.; Yang, P., *Acc. Chem. Res.* **2006**, 39, (4), 239-248.
12. Pileni, M. P., *Acc. Chem.l Res.* **2008**, 41, (12), 1799-1809.
13. Wu, M.-H.; Park, C.; Whitesides, G. M., *Langmuir* **2002**, 18, (24), 9312-9318.

14. Chen, J. I. L.; von Freymann, G.; Choi, S. Y.; Kitaev, V.; Ozin, G. A., *Adv. Mater.***2006**, 18, (14), 1915-1919.

15. Elghanian, R.; Storhoff, J. J.; Mucic, R. C.; Letsinger, R. L.; Mirkin, C. A., *Science* **1997**, 277, (5329), 1078-1081.

16. Huang, C. C.; Chang, H. T., *Anal. Chem.* **2006**, 78, 8332.

17. Jadzinsky, P. D.; Calero, G.; Ackerson, C. J.; Bushnell, D. A.; Kornberg, R. D., *Science* **2007**, 318, (5849), 430-433.

18. Khalid, S.; Yuhuang, W.; Joseph, F.; Rafael, A. V.; Chang, L.; Chad, A. M., *Angew.Chem. Int.* **2006**, 45, (43), 7220-7223.

19. Li, M., Tang, H.X.,Roukes, M.L., *Nat. Nanotechnol.* **2007**, 2, 114.

20. Panyam. J. Labhasetwar, V., *Adv.Drug Delivery Rev.* **2003**, 55, 329.

21. Chan, C. K.; Peng, H.; Twesten, R. D.; Jarausch, K.; Zhang, X. F.; Cui, Y., *Nano Lett.* **2007**, 7, 490.

22. Mock, J. J.; Smith, D. R.; Schultz, S., *Nano Lett.* **2003**, 3, 485.

23. Prasad, P. N., *Nanophotonics*. John Wiley & Sons, Inc.: 2004; Vol. I.

24. Atwater, H. A., *Sci. Am.* **2007**, 296, 56.

25. Ozbay, E., *Science* **2006**, 311, 189.

26. Bozhevolnyi, S. I.; Volkov, V. S.; Devaux, E.; Ebbesen, T. W., *Phys. Rev. Lett.* **2005**, 95, 046802.

27. Haes, A. J.; Van Duyne, R. P., *J. Am. Chem. Soc.* **2002**, 124, 10596.

28. Hu, M.; Chen, J.; Li, Z. Y.; Au, L.; Hartland, G. V.; Li, X.; Marquez, M.; Xia, Y., *Chem. Soc. Rev.* **2006**, 35, 1084.

29. Malyarchuk, V.; Hua, F.; Mack, N. H.; Velasquez, V. T.; White, J. O.; Nuzzo, R. G.; Rogers, J. A., *Opt. Express* **2005**, 13, 5669.

30. Nath, N.; Chilkoti, A., *Anal. Chem.* **2002**, 74, 504.

31. Ghosh, S. K.; Nath, S.; Kundu, S.; Esumi, K.; Pal, T., *J. Phys. Chem. B* **2004**, 108, 13963.

32. Kelly, K. L.; Coronado, E.; Zhao, L. L.; Schatz, G. C., *J. Phys. Chem. B* **2003**, 107, 668.

33. Kreibig, U.; Vollmer, M., *Optical Properties of Metal Clusters; Springer: Berlin* 1995, 25, 532.

34. Mock, J. J.; Barbic, M.; Smith, D. R.; Schultz, D. A.; Schultz, S., *J. Chem. Phys.* **2002**, 116, 6755.

35. Willets, K. A.; Van Duyne, R. P., *Ann. Rev. Phys. Chem.* **2006**, 58, 267.

36. Mie, G., *Ann. Phys.* **1908**, 25, 377.

37. Muduli, P.; Friedland, K.; Herfort, J.; Schonherr, H.; Ploog, K., *J.Appl. phys.* **2009**, 105, (7), 07B104.

38. Walker, M.; Diebel, C.; Haugh, C.; Pankhurst, P.; Montgomery, J.; Green, C., *Nature* **1997**, 390, 371.

39. Sakamoto, M.; Tachikawa, T.; Fujitsuka, M.; Majima, T., *Adv. Funct. Mater.* **2007**, 17, 857.

40. Sun, S., *Adv. Mater.* **2006**, 18, 393.

41. Sun, S.; Zeng, H.; Robinson, D. B.; Raoux, S.; Rice, P. M.; Wang, S. X.; Li, G., *J. Am. Chem. Soc.* **2004**, 126, 273.

42. Sun, S. H., *Adv. Mater.* **2006**, 18, 393.

43. Sun, S. H.; Zeng, H.; Robinson, D. B.; Raoux, S.; Rice, P. M.; Wang, S. X.; Li, G. X., *J. Am. Chem. Soc.* **2004**, 126, 273.

44. Park, J.; An, K. J.; Hwang, Y. S.; Park, J. G.; Noh, H. J.; Kim, J. Y.; Park, J. H.; Hwang, N. M.; Hyeon, T., *Nat. Mater.* **2004**, 3, 891.

45. Lee, Y.; Lee, J.; Bae, C. J.; Park, J. G.; Noh, H. J.; Park, J. H.; Hyeon, T., *Advanced Functional Materials* **2005**, 15, (3), 503-509.

46. Latham, A. H.; Tarpara, A. N.; Williams, M. E., *Anal. Chem.* **2007**, 79, 5746.

47. Latham, A. H.; Williams, M. E., *Acc. Chem. Res.* **2008**, 41, (3), 411-420.

48. Jun, Y.-w.; Seo, J.-w.; Cheon, J., *Acc. Chem.l Res.* **2008**, 41, (2), 179-189.

49. Jales, D., *Introduction to Magnetism and Magetnic Materials*. **1998**.

50. Mahajan, S.; Abdelsalam, M.; Sugawara, Y.; Cintra, S.; Russell, A.; Baumberg, J.; Bartlett, P., *Phys. Chem. Chem. Phys.* **2007**, 9, 104.

51. Mirkin, C. A.; Niemeyer, C. M., *Nanobiotechnology II: More Concept and Applications*. **2007**.

52. Sun, Q.; Kandalam, A. K.; Wang, Q.; Jena, P.; Kawazoe, Y.; Marquez, M., *Phys. Rev. B* **2006**, 73, (13), 134409.

53. Fortin, J.-P.; Wilhelm, C.; Servais, J.; MÃ©nager, C.; Bacri, J.-C.; Gazeau, F., *J. Am. Chem. Soc.* **2007**, 129, (9), 2628-2635.

54. Namdeo, M.; Saxena, S.; Tankhiwale, R.; Bajpai, M.; Mohan, Y. M.; Bajpai, S. K., *J. Nanosci. Nanotechnol.* **2008**, 8, (7), 3247-3271.

55. Talapin, D. V.; Lee, J.-S.; Kovalenko, M. V.; Shevchenko, E. V., *Chem. Rev.* **2009**, 110, (1), 389-458.

56. Yoshiaki, N.; Ryota, S.; Masafumi, U.; Sung-Pyo, C.; Nobuo, T.; Masakazu, I., *Appl. Phys. Lett.* **2006**, 89, (12), 123104.

57. Martinelli, L.; Grilli, E.; Migas, D. B.; Miglio, L.; Marabelli, F.; Soci, C.; Geddo, M.; Grimaldi, M. G.; Spinella, C., *Phys. Rev. B* 2002, 66, (8), 085320.

58. Liu, Z., Wang, S., Otogawa, N., Osamura, M., Ootsuka, T., Mise, T., suzuki, Y., Fukuzawa, Y., Nakayama, Y., tanoue, H., Makita, Y., *3rd World conference on Photovoltaic Energy Conversion May 11-18, 2003 Osaka, Japan* 2003, poster 126-129.

59. Buonassisi, T.; Istratov, A. A.; Marcus, M. A.; Lai, B.; Cai, Z. H.; Heald, S. M.; Weber, E. R., *Nat. Mater.* **2005**, 4, (9), 676-679.

60. Ayache, R.; Bouabellou, A.; Eichhorn, F.; Richter, E.; Mucklich, A., *Review of Scientific Instruments* 2006, 77, (3).

61. Akiyama, K.; Kaneko, S.; Kimura, T.; Funakubo, H., *Jpn. J. Appl. Phys.* **2005**, 44, (4B), 2496-2501.

62. Zichichi, A., *Silicides Fundamentals and Applications, World Scientific Publishing Co.pte.Ltd. singapore*. **2000**.

63. Borisenko, V. E., Semiconducting Silicides. *Springer: Berlin* **2000**, 39.

64. Hansen, M. P. A., K.rer.nat.; , *Constitution of Binary Alloys*. Second ed.; McGraw- Hill Book Company: **1958** ,page no.713.

65. Matsumoto, M.; Sugie, K.; Kawauchi, T.; Fukutani, K.; Okano, T., *Jpn. J.Appl. Phys.* **2006**, 45, (3B), 2390-2394.

66. Liu, Z. X.; Osamura, M.; Ootsuka, T.; Wang, S. N.; Fukuzawa, Y.; Suzuki, Y.; Kuroda, R.; Mise, T.; Otogawa, N.; Nakayama, Y.; Tanoue, H.; Makita, Y., *Opt. Mater.***2005**, 27, (5), 942-947.

67. Liu, Z.; Osamura, M.; Ootsuka, T.; Kuroda, R.; Makita, Y.; Tanoue, H.; Fukuzawa, Y.; Otogawa, N.; Nakayama, Y., *Thin Solid Films* **2006**, 515, (4), 1532-1538.

68. Kakemoto, H.; Makita, Y.; Sakuragi, S.; Tsukamoto, T., *Jpn. J.Appl. Phys.* **1999**, 38, (9A), 5192-5199.

69. Kwon, S. G.; Piao, Y.; Park, J.; Angappane, S.; Jo, Y.; Hwang, N.-M.; Park, J.-G.; Hyeon, T., *J. Am. Chem. Soc.* **2007**, 129, (41), 12571-12584.

70. Shevchenko, E. V.; Talapin, D. V.; Schnablegger, H.; Kornowski, A.; Festin, Ã. r.; Svedlindh, P.; Haase, M.; Weller, H., *J. Am. Chem. Soc.* **2003**, 125, (30), 9090-9101.

71. Sadoh, T.; Takeuchi, H.; Ueda, K.; Kenjo, A.; Miyao, M., *Jpn. J. Appl. Phys.,* **2006**, 45, (4B), 3598-600.

72. Rout, B.; Sundaravel, B.; Das, A. K.; Ghose, S. K.; Sekar, K.; Mahapatra, D. P.; Dev, B. N., *J. Vac. Sci. B* **2000**, 18, (4), 1847-1852.

73. Celso, de Mello D.; Peter, L.; Daniel, V., *Small* **2005**, 1, (12), 1152-1162.

74. Talapin, D. V.; Rogach, A. L.; Kornowski, A.; Haase, M.; Weller, H., *Nano Lett.* **2001**, 1, (4), 207-211.

75. Ando, Y.; Hamaya, K.; Kasahara, K.; Ueda, K.; Nozaki, Y.; Sadoh, T.; Maeda, Y.; Matsuyama, K.; Miyao, M., *J. Appl. Phys.* **2009**, 105, (7).

CHAPTER 2 - Synthesis and characterizations of Fe-Au core-shell Nanoparticles

Introduction

During the past decade, several studies focused on core-shell structured nanoparticles. The enhanced optical, electronic and magnetic properties of the core-shell nanoparticles compared to the single component ones make them an attractive candidate for future applications.[1] For core-shell nanoparticles, it is necessary to understand how the shape, size and their surface properties affect the physical and chemical properties relevant to applications. The combination of either iron or iron oxide core and gold shell is specifically appealing because gold is a noble metal, provides a good platform for surface functionalization and modification.[2-6] In addition, the shell layer protects against oxidation and helps to maintain the long-term stability of the particles.[1, 7-12] Biocompatibility is particularly important because these particles are frequently used in magnetic targeted drug delivery and hyperthermia treatment.[1, 7, 11, 13-15]Because of magnetic iron core, the nanoparticles hold higher magnetic moment than iron oxides. When iron is oxidized its magnetic moment is decreased approximately by factor of three. The presence of gold shell protects the particles from oxidation.[3, 16, 17] Here, a reverse micelles method is reported to prepare the iron core-gold shell nanoparticles with plasmon resonance peaks in the range 555 nm to 595 nm. The iron core-gold shell nanoparticles prepared here are suitable candidates for combined AC magnetic field and the laser induced hyperthermia.[14, 18]In laser induced hyperthermia, the heating takes place by absorption of light at the frequency of the surface plasmon resonance of the metal core-shell nanoparticles. The spectral shift of the gold plasmon resonance to the near IR is desirable as shown in Figure 1-3b because of the lesser absorption and scattering of the human tissue. Despite their attractive application, precise control of the uniform metal coating,

monodispersity of the size and shape, and resistance to oxidation are still major challenges.[5, 7, 9, 11, 12, 19-22] Iron or iron oxide core-gold shell particles are superparamagnetic[5, 11, 15, 23-25]and possible applications include magnetic seals, printing, recording, magnetic resonance imaging (MRI) agents, cell tagging and sorting.[1] Iron or iron oxide core-gold shell nanoparticles have been prepared by other groups and their properties have been investigated.[3, 12, 13, 15-17, 22, 24, 26-28] In all study it is found that the chemical states of the core materials, uniformity of metal coating, thickness of shell and core radius, size and shape monodispersity issues are the key challenges to overcome. Two phase reduction, sequential reduction and digestive ripening are the common methods to prepare many metal nanoparticles, but these methods are not applied for the core-shell nanoparticles. In this experiment, first core-shell nanoparticles are prepared in reverse micelles and digestive ripening is carried out in several solvents in presence of different ligands to improve the quality of gold shell.

Experimental

Over the years, several methods of nanoparticle synthesis have been developed. Two main soft-chemical routes are: in situ synthesis in the hydrophilic core of reverse micelles developed in the 1980s by Pileni et al.[20, 29-31] and the phase-transfer method developed by Brust et al. in the 1990s.[32-34] In the first method, the inner core of the reverse micelles is considered as a nanoreactor, and the size of the nanocrystals is controlled by the state of the water molecules inside the hydrophilic core. The dynamic collisions and exchange among the reverse micelle contains enable the reaction to proceed.[35] Since the reaction is confined within the reactor cavity, the growth of crystal beyond the dimension of cavity is inhibited. The typical reverse micelles nanoreactor is made of hydrophilic head group and hydrophobic tell group as shown in Figure 2-1.

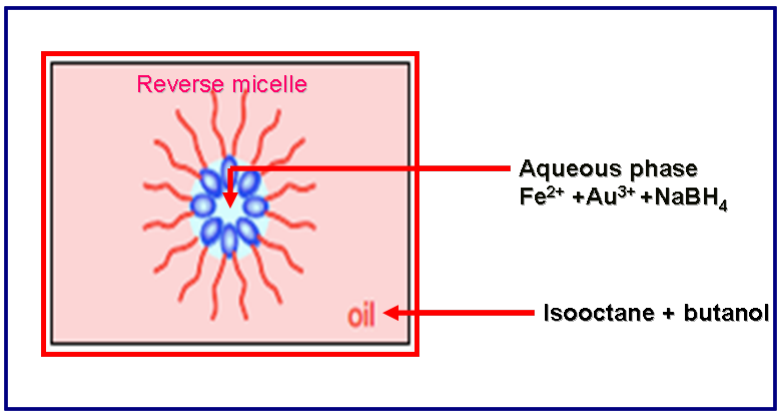

Figure 2-1 Schematic representation of a reverse micelle.

In this study, reverse micelles experimental method is presented to produces iron core and gold shell nanoparticles with size distribution from 5 to 10 nm. The nanoparticles exhibit large spectral shift in their plasmon resonance in agreement with the predictions from Mie scattering theory. The peak position can be controlled by varying the synthetic conditions. All chemicals are purchased from Aldrich and used without further purification. Distilled water is used throughout. All liquid starting materials are degassed for 2 h prior to the experiment. Fe-Au nanoparticles are prepared in a reverse micelle of dodecyldimethylammonium bromide (DDAB), using 1-butanol as a cosurfactant and isoctane as the hydrophobic phase. A water solution containing metal ions is added to the solution. The molar ratio of water to DDAB (ω=H_2O/DDAB) 40 is selected to prepare the iron nanoparticles. The size of the reverse micelle is determined by the molar ratio of water to surfactant. It has been demonstrated that the hydrophilic core diameter is related to the water content, of the droplet w = H_2O/DDAB, by D (nm) = 0.3 w of the droplet.[36] The procedure and components for the experiment are schematically shown in Figure 2-2. First the iron nanoparticles are prepared within the micelles by reduction of Fe^{2+} using sodium borohydride. Iron nanoparticles are obtained inside the

micelles after stirring for an hour. Gold precursor is added together withadditional components as shown in Figure 2-2 and the entire solution is stirred for two hours.

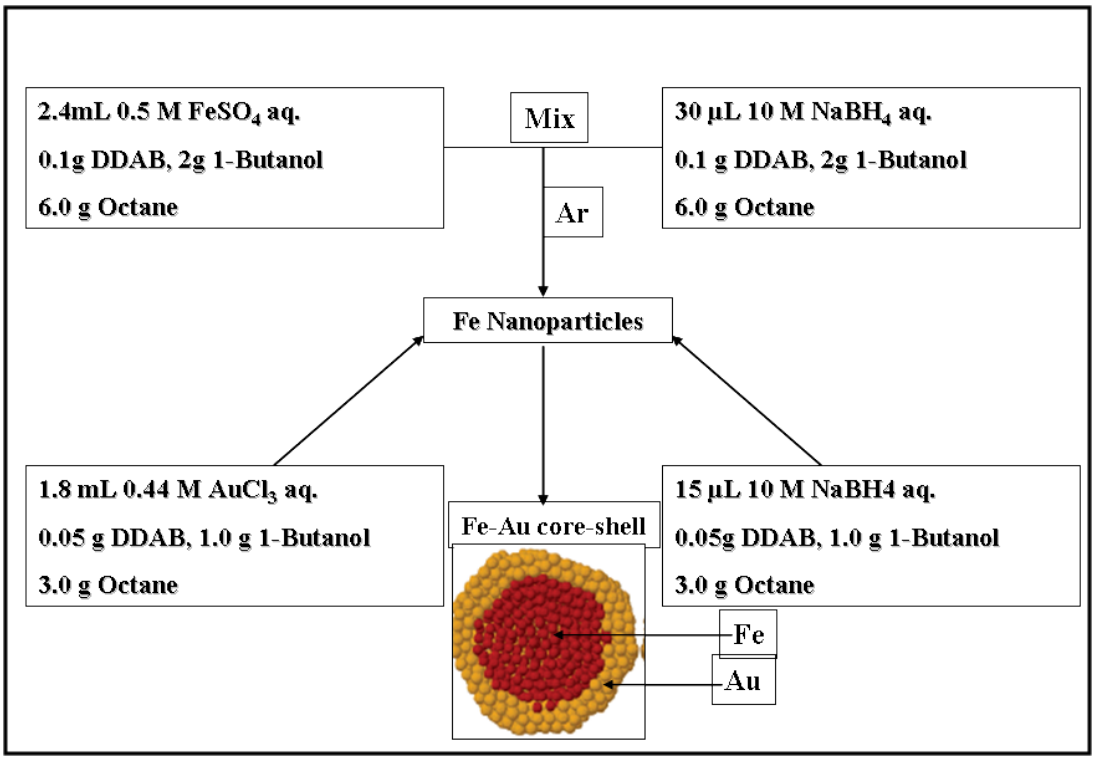

Figure 2-2 Schematic diagram of the procedure to prepare Fe-Au core-shell nanoparticles.

After 3 h of reaction, stabilizing agent dodecylamine (1.5 mL) or dodecylthiol (60 µL) was added to the reaction mixture, which is left for another one hours. The isooctane is removed by evaporation, and the waxy residue is redispersed in 50 mL of ethanol, followed by centrifugation at 8000 rpm for 20 minutes. The purple-brown precipitate is redispersed in 40 mL of ethanol. The iron-containing nanoparticles are then separated from those particles that contained just gold using a strong magnet (5 Tesla) and a centrifuge. The repetitive centrifuging

and dissolving is continued until the supernatant is colored due to presence of nanoparticles. The colored supernatants are collected after each washing step until the obtained supernatant is again transparent after centrifugation. After evaporation of the collected colored supernatant the solid residue is collected and dissolved in hexane. The dissolution is carried out in presence of 1.5 mL of oleic acid and oleyl amine. After refluxing the solution in 20 mL diphenyl ether for an hour, the excess solvent and ligands are removed by repetitive washing with ethanol and centrifugation. Ethanol washing and centrifugation are employed for size selective precipitation.[12] The three different sizes (9, 7 and 6 nm) of Fe –Au core-shell nanoparticles are prepared. The final solid is dissolved in hexane and further characterizations are performed.

Results and discussion

Figure 2-3 shows the UV-visible absorption spectrum for iron core-gold shell nanoparticles prepared by using different concentration ratios of iron to gold. The surface plasmon band of the particles is formed due to interaction between the core and the shell. The plasmon peak position of iron-gold core-shell nanoparticle is shifted significantly (~ 65 nm) compare to pure gold nanoparticle (~ 530 nm) prepared under identical conditions. Surprisingly the width of the plasmon peak of 1:2 and 1:4 concentrations ratios of iron to gold is very broad probably due to large distribution of micelles sizes. Several factors may contribute to the line shape of plasmon resonance. One of the important factors is the nonuniform size distribution of the nanoparticles due to random micelles size distribution. Another possible broadening mechanism of the plasmon peak is the non uniform shell thickness on the iron core of the nanoparticless.[37, 38]

The thin shell causes the scattering length to decrease resulting in pear broadening.

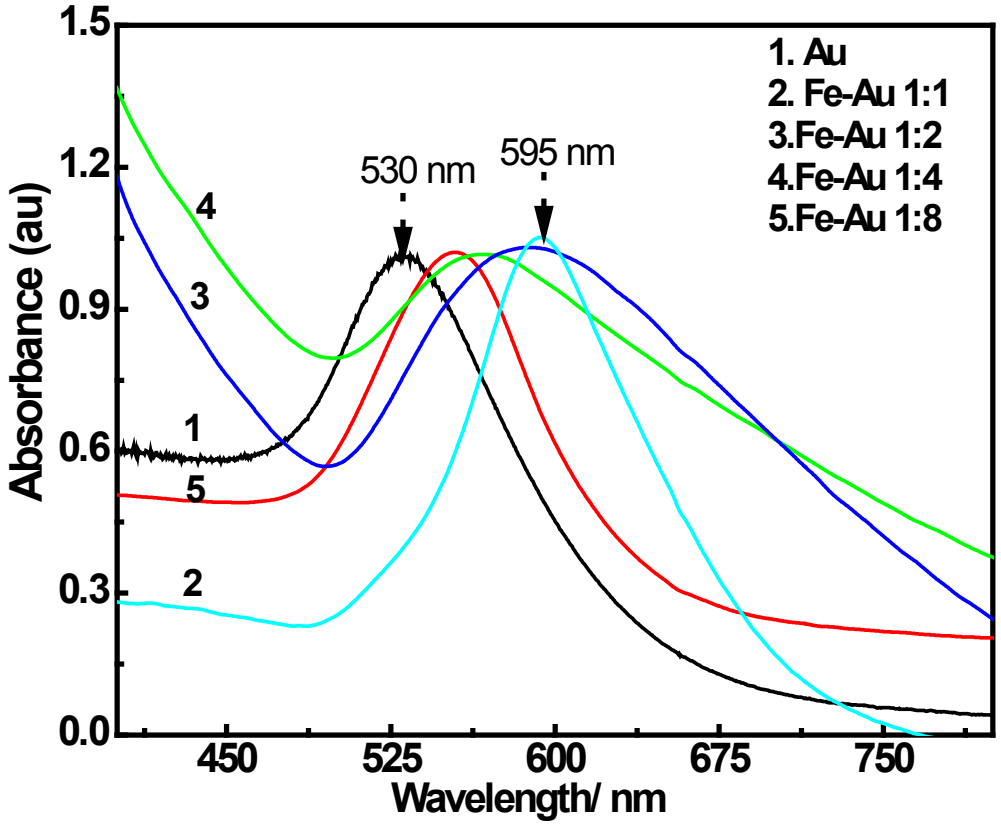

Figure 2-3 Shows UV-visible absorption spectra in toluene for gold and iron-gold core-shell nanoparticles with various concentrations ratios of gold and iron precursors.

The absorption peak of the nanoparticles is tunable depending on the thickness of the shell. In the gold coated nanoparticles, there is red shift in the surface plasmon peaks position with decreasing of shell thickness and blue shift with increasing of shell thickness as the calculation shows in Figure 1-3b.[39, 40]Similarly, the experiment in Figure 2.3 shows the tunable plasmon peak position when the concentrations ratios of gold and iron precursor is varied. It is

clearly indicated that there is red shift in plasmon peak position with decreasing amounts of gold. When the Fe-Au concentration ratio is 1:1 the plasmon peak position is at 595 nm. On the other hand, when the concentrations ratio of gold is increased from 1:1 to 1:8 the plasmon peak positions shifted to the blue. For the 1:8 concentration ratio of Fe-Au, the maximum of the plasmon peak position is located at 555 nm. Due to small size of nanoparticles, the conduction band electrons are confined in narrow energy range and mostly present in the visible or ultraviolet part of the electromagnetic spectrum. The shift in plasmon peak position is due to perturbation of electrons cloud oscillation of surface gold atoms by iron atoms.[41-43]

Figure 2-4 shows the XRD pattern of iron core-gold shell nanoparticles which are obtained from Fe (2+) precursor. The patterns reveal that the sample is crystalline. The 2θ angles of iron-gold core-shell nanoparticles are located at 38.4^{o}, 44.62^{o}, 65.13^{o} and 82.43^{o} corresponds to Au (111), Au (200) Fe (110), Au (220) Fe (200), and Au (222) Fe (211) planes.[5, 7, 11] There are no prominent peaks of iron oxides. For comparison, the XRD patterns of pure gold and iron are also presented in Figure 2.4. Theoretically, both core and shell phases should appear in diffraction pattern of core-shell structured nanoparticles. When iron or iron oxide-gold core-shell nanoparticles are concerned, it is found that only the peaks of gold are observable in spectra of powder XRD. This is due to heavy atom effect displayed by gold on iron or iron oxide as explained by Wang et al.[12, 44] The crystallite size of nanoparticles is determined using Debye-Scherrer equation: $L = (0.088\lambda) / (\beta \text{Cos}\theta)$, where λ is the X-ray wavelength in nm, β is the intrinsic peak width in radians (2θ), θ is the Bragg angle and 0.88 is the Debye-Scherrer constant.[45] The size of iron-gold core-shell nanoparticles is calculated from the most intense Fe-Au fcc (111) electronic reflection is 8.1± 0.3 nm. The large value of particle size compared to TEM measurement is due to detection of nanoparticles in an ensemble by XRD as opposed to

individual nanoparticles in TEM measurements. When calculating the particles size using Scherrer equation the most intense peak is fitted to a Gaussian function in each experiment. The error on the fitting determines the error in the size distribution of the particles. For the baseline correction two sets of baseline data are used in approximately 3 degrees on either side of each peak (this is to minimize any angular dependence on the background). For this calculation, instrumental broadening as well as stress-related broadening coefficient both considered for the accuracy.

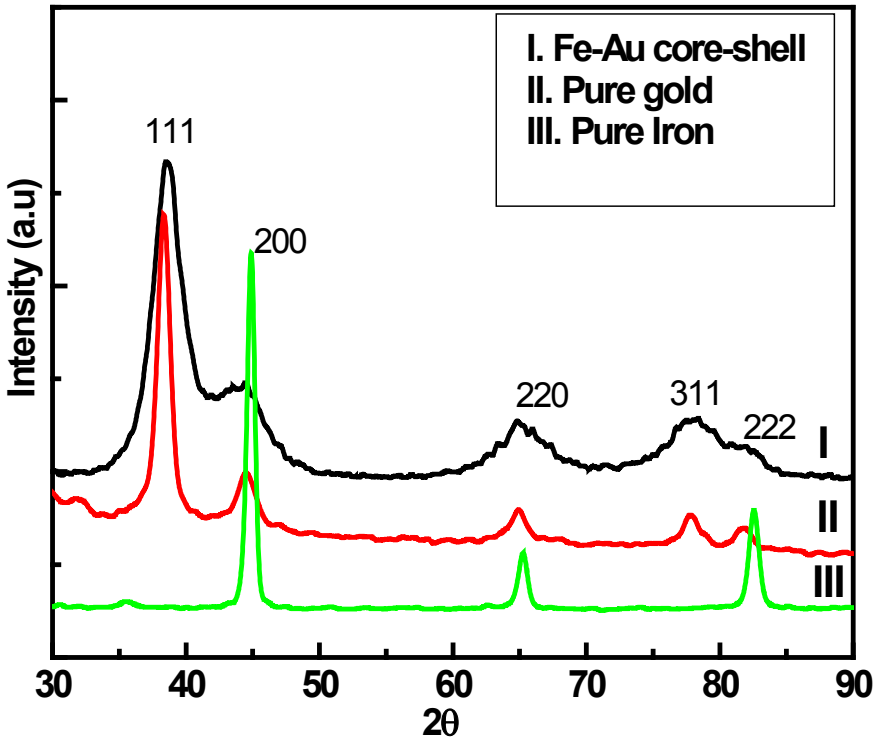

Figure 2-4 Shows the XRD patterns of Fe-Au core-shell nanoparticles (I) together with pure gold (II) and pure iron nanoparticles (III).

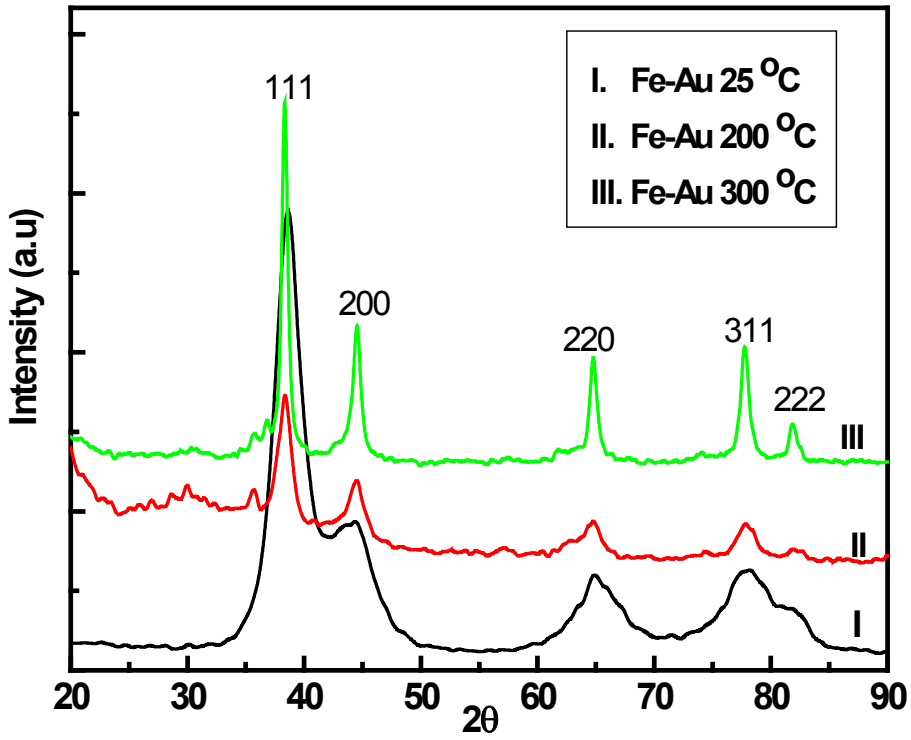

Figure 2-5 XRD patterns of Fe-Au core-shell nanoparticles at 25 ^{o}C (I) and annealed at 200 (II) and 300 ^{o}C (III).

To investigate whether or not there is amorphous iron or iron oxide present, an experiment is carried out to asses the effect of annealing. The core shell nanoparticles are heated to 200 and 300 ^{o}C in air for overnight. Under these conditions, any amorphous iron will oxidize and crystallize. The experimental results are shown in Figure 2-5.

The results show that the core-shell nanoparticles are quite stable. Narrowing the XRD peaks is observed due to crystallization of nanoparticles during heating. An appearance of a peak at 34.8 2θ degree is indicative appearance of amorphous iron oxide (Fe_3O_4) during annealing. However, the prominent XRD peaks of iron-gold core-shell nanoparticle remain and no shift in

XRD peak position is observed. Therefore, the particles are core-shell, crystalline and not alloyed during annealing. No phase segregation of the nanoparticles is observed during heating.

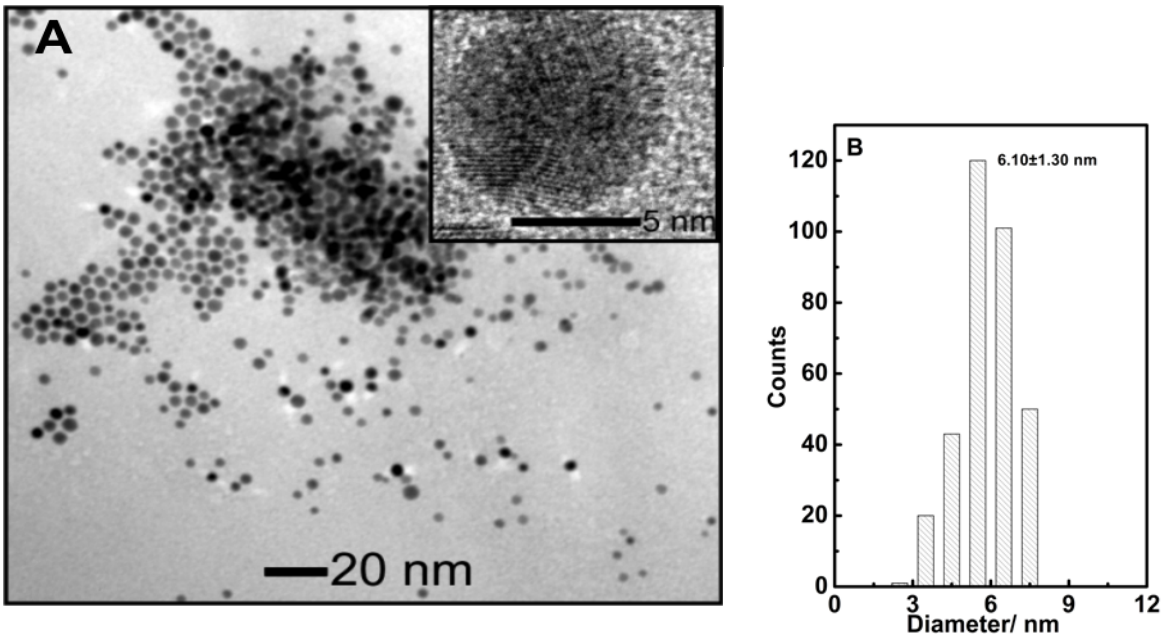

Figure 2-6 (A) TEM image of Fe-Au core shell nanoparticles as prepared by reverse micelles method in presence of dodecyl amine and dodecyl thiol stabilizers; Inset shows the HRTEM image of same nanoparticles. (B) Histogram shows the corresponding size distribution of the nanoparticles.

TEM image shows that Fe-Au core-shell nanoparticles are spherical and nearly monodisperse; the average size distribution of the nanoparticles is 6.1 ± 1.3 nm as shown in Figure 2.6b. There is little aggregation in this case due to effective binding of dodecyl amine and dodecyl thiol on the nanoparticles surface. The better binding efficiency of the ligands probably is attributed to the reaction taking place in a micro heterogeneous medium with water droplets stabilized by a combination of DDAB, the alkyl amine and alkyl thiol rather than homogeneous organic medium.[46] The inset shows the HRTEM image of Fe-Au nanoparticles revealing the

core-shell structure with high crystallinity. The lattice fringes of the shell is found to be 0.24 nm, which is the d (111) lattice spacing of gold.[47] The thickness of the gold shell measured form the HRTEM is~ 2.0 nm and the core diameter is approximately 4.0 ± 0.8 nm.

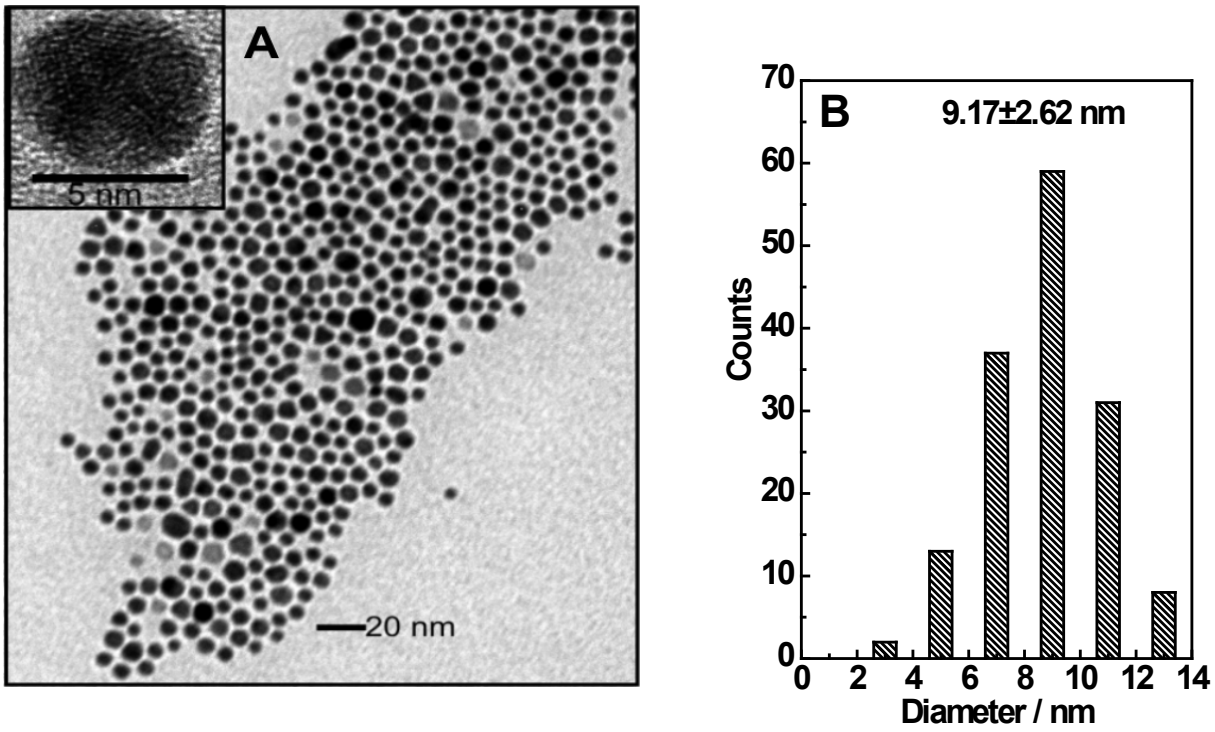

Figure 2-7 TEM image of Fe-Au core-shell nanoparticles obtain after refluxing the nanoparticles in diphenyl ether in presence of oleic acid and oleyl amine. (B) Size histogram on nanoparticles shown in the TEM image.

Figure 2.7a shows the Fe-Au nanoparticles obtained after refluxing the nanoparticles in presence of oleic acid and oleyl amine in diphenyl ether for one hour at 250 ^{o}C. The extent of aggregation of the nanoparticles is significantly less compared to the initial nanoparticles. The average size distribution is increased to 9.1 ± 2.6 nm due to the binding of large ligands to the surface of the nanoparticles. The large ligands render the better solubility of the nanoparticles in

the organic solvents. The inset in Figure 2-7a shows the HRTEM image of the Fe-Au core-shell nanoparticle; the nanoparticle retain the core-shell structure even after refluxing.

The size selective precipitation of these nanoparticles is carried out by repetitive dissolution of the particles in hexane than washing with excess amount of ethanol and centrifuging at 8000 rpm for 30 minutes. The average size of the Fe-Au nanoparticles after 2nd washing and centrifugation for 30 minutes is found to be 7.0 ± 2.1 nm as shown in Fig 2.8b. As expected particles are begin to order in the form of superlattices (Figure 2.8a). After 3rd washing and additional 30 minutes of centrifugation at 8000 rpm average size of the particles is changed to 6.1 ± 1.9 nm (Figure 2.8d). As in Figure 2.8c the particles form superlattices that are larger than the previous step.

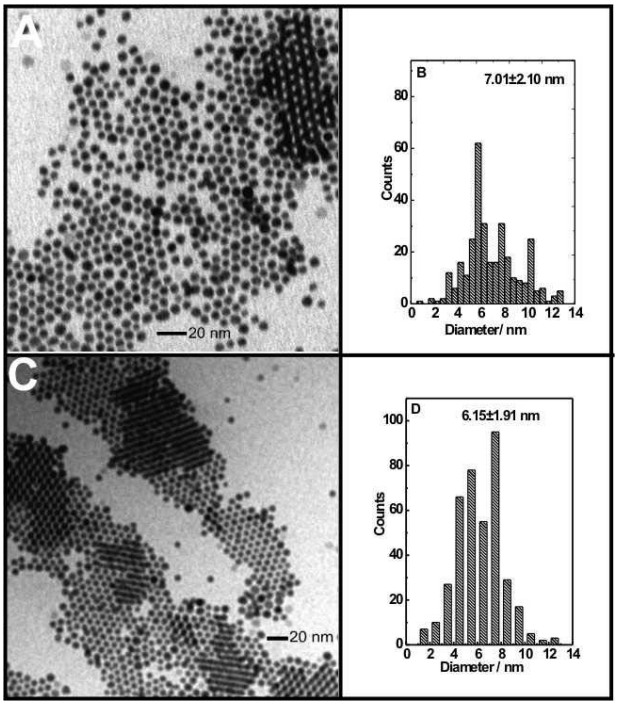

Figure 2-8 represent the TEM images of Fe-Au core-shell nanoparticles after 1st and 2nd size selective precipitation (A) and (C). The respective size distributions are represented by the histograms (B) & (D).

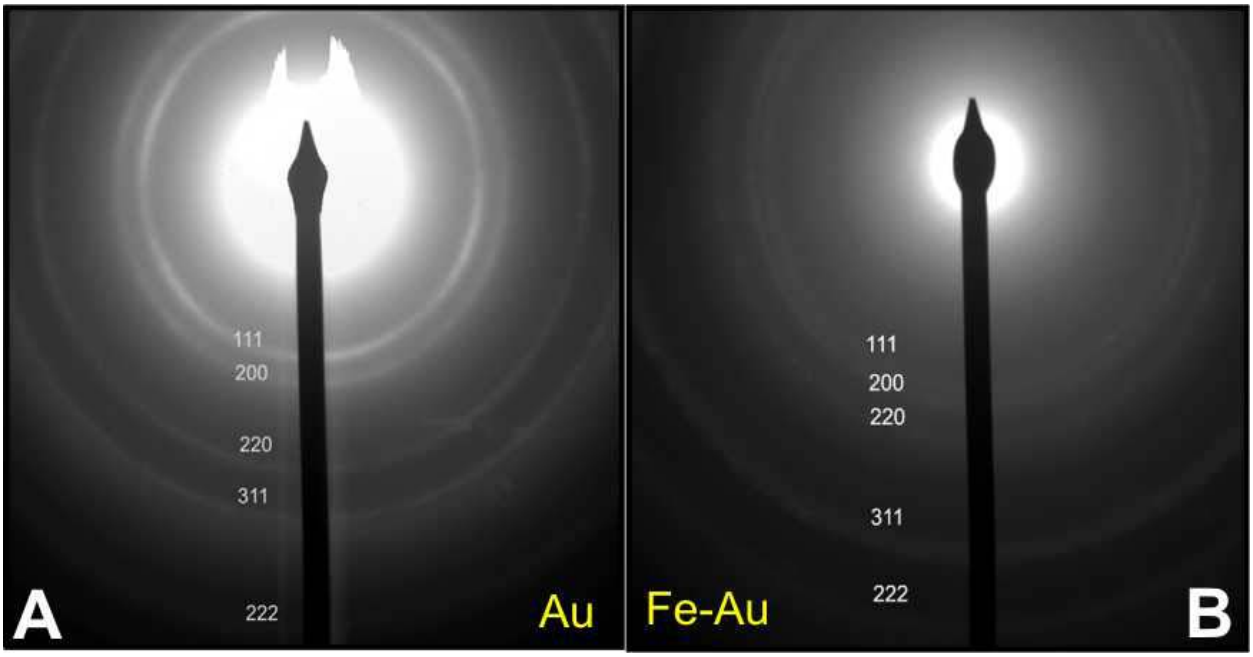

Figure 2-9 represents electron diffraction of pure gold (A) and Fe-Au core-shell nanoparticles (B).

Figure 2.9a & b are selected area electron diffraction patterns of the pure gold and iron-gold core-shell nanoparticles respectively. Crystal structure of gold is face center cubic (fcc) with lattice constant a = 0.408 nm; iron has body center cubic (bcc) structure with lattice constant of a = 0.287 nm. Therefore, the diffraction rings appear very close to each other (Figure 2.9b). Due to slight lattice mismatch the difference can be resolved from the broaden diffraction rings of Fe-Au nanoparticles due to overlapping of (200), (220), & (222) electronic reflection of gold to that of iron (110), (200), & (211) electronic reflections.

The composition of core-shell nanoparticles is analyzed by energy dispersive X-ray spectroscopy (EDX). Figure 2.10 shows a typical EDX spectrum for the iron-gold core-shell nanoparticle. The appearance of many prominent peaks for gold and iron confirm the presence of iron and gold in the core-shell nanoparticles. The average composition of iron is 78 ±1.3 atomic % in the Fe-Au core shell nanoparticles. The peak due to oxygen may be due to some residual iron oxide or from ligand such as oleic acid. The presence of copper is from the copper grid itself. From the atomic % of iron to gold; the calculated shell thickness and the core radius are 1.8 ± 0.4 nm and 4.4 ± 0.3 nm. These values agree well with the results of the inductively coupled plasma (ICP) analysis and HRTEM measurements.

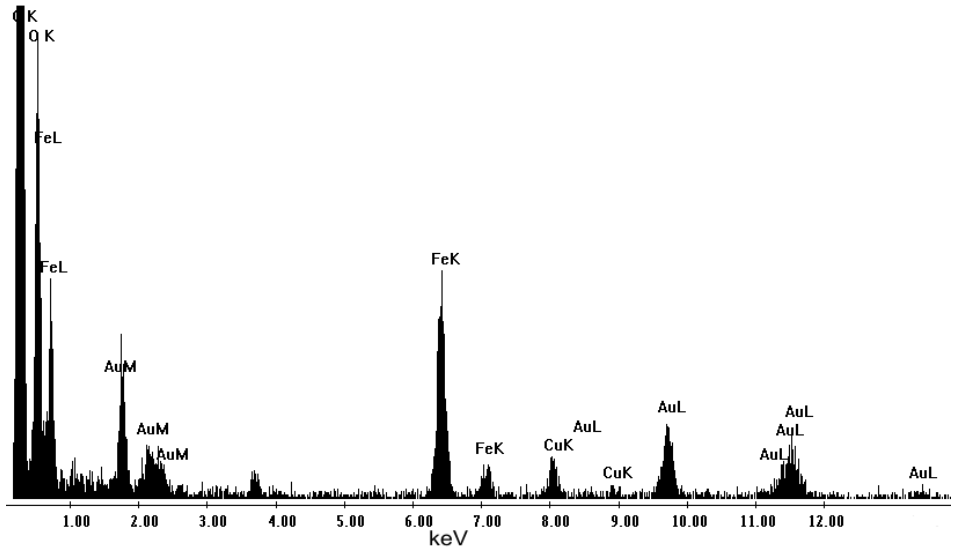

Figure 2-10 EDX spectra obtained from~ 7nm Fe-Au core-shell nanoparticle.

The shell thickness and core size has also been calculated using ICP analysis. In order to carry out ICP analysis; samples are prepared by dissolving (0.02g) the known amount of core shell nanoparticles in 10 mL aqua-regia (1:3 ratios by volume of HNO_3 and HCl) and are diluted to 200 mL. The final 200 mL solution is used for the chemical analysis. The amount of iron and gold are found to be ~75% ± 1.12 and ~25 % ± 1.23 respectively. This value agrees with the simulated shell and core radius based on their plasmons peak positions, HRTEM measurements, and EDX analysis.

The spontaneous self-assembling of nanoparticles depends on the balances of interparticle forces and the monodispersity of the nanoprticles. An additional term called magnetostatic force is considered as an important factor for ordering of magnetic nanoparticle. In the presence of external magnetic field the magnetostatic force favors the formation of magnetically aligned chains of magnetic dipoles, rather than two or three dimensional structures.[24]The self assembling of iron-gold nanoparticles is carried out under magnetic field between the poles of a strong magnet (5 Tesla) and the assembly is examined by TEM. The chain lengths of assembled nanoparticles range from 500 nm to 1μm (Figure 2-11a and b). Dodecyl thiol and dodecyl amine are the ligands; attached on the particles of Figure 2-11b. Figure 2-11a shows the nanoparticles prepared with oleic acid and oleyl amine.

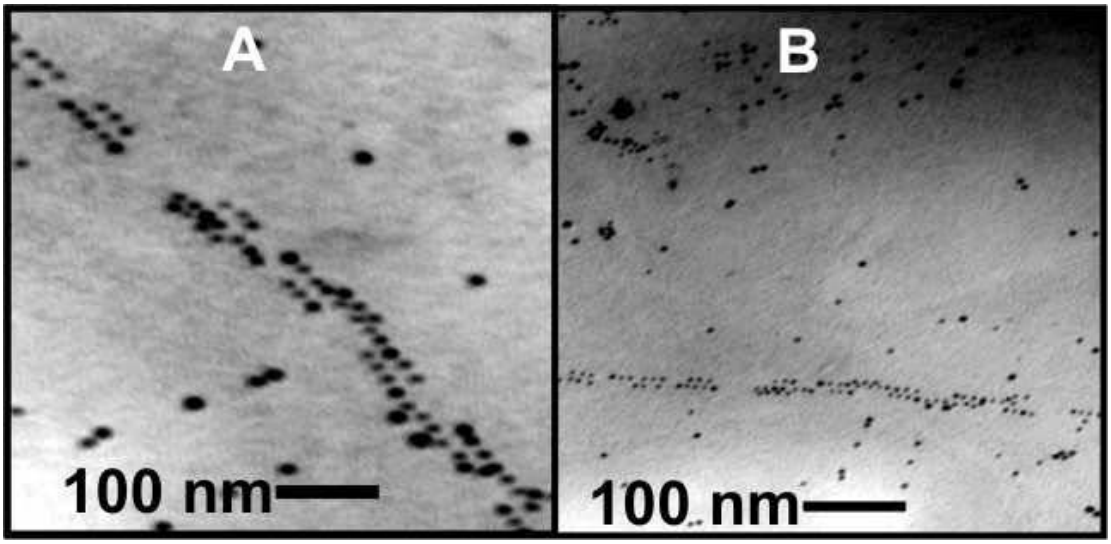

Figure 2-11 Shows self-assembling of iron-gold core-shell nanoparticles in presence of magneticfield, as prepared nanoparticles (B); after refluxing and centrifuging (A).

Magnetic properties of the large Fe-Au core-shell nanoparticles are studied by using a commercial superconducting quantum interference device (SQUID) magnetometer. The field dependence of the magnetization of Fe-Au core-shell nanoparticles is studied from 10 K to 280 K as represented by the Figure 2.12. The hysteresis is negligible above 50 K; however it shows significant hysteresis at temperature 10 K and 50 K. The magnification of the magnetization curve near origin clearly shows the hysteresis at 10 K and 50 K as shown in Figure 2.12b. The particles near room temperature show the superparamagnetic behavior as there is absence of magnetic hysteresis loops. The absence of hysteresis; which is a special signature of a

ferromagnetic material, is attributed to the small particle size and finite size effect in the nanoparticles.[48]

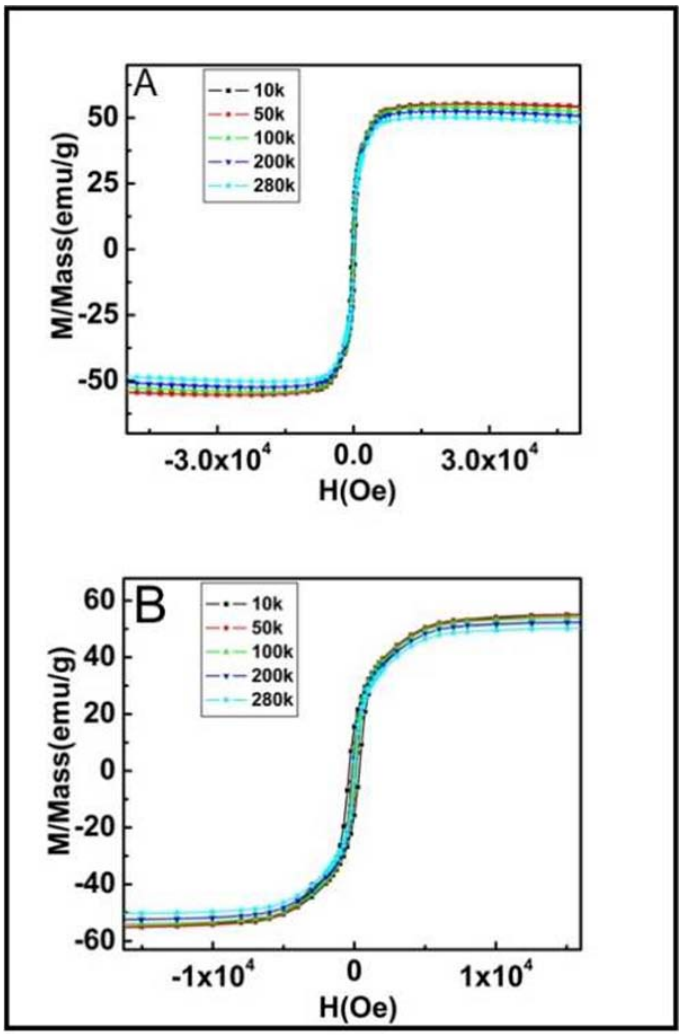

Figure 2-12 Shows the saturation magnetization curve for Fe-Au core-shell nanoparticles at 10 K to 280 K (A). Magnified form near the origin of the figure a (B).

Conclusions:

Gold-iron core-shell nanoparticles are synthesized by using DDAB as a cationic surfactant in a reverse micelles nanoreactor. Refluxing the nanoparticles in oleic acid and oleyl amine increase the size of the nanoparticles.The size selective precipitation helps to separate different sizes of nanoparticles, multiple washing, and precipitation and redispersion yield nanoparticles superlattice. The core-shell nanoparticles show similar plasmonic behavior to that of gold and display the plasmon peaks positions in between 555 nm to 595 nm. The plasmon peaks are significantly red shifted compare to pure nanoparticles and tunable depending upon the amount of gold precursor. The higher gold concentration causes the plasmon peaks shift to blue due to increase in shell thickness. The particles self-assemble in the presence of external magnetic field and show superparamagnetic behavior at room temperature. The digestive ripening process is applied first time for the core-shell nanoparticles prepared from reverse micelles.

References:

1. Tartaj, P.; Morales, M. D.; Veintemillas-Verdaguer, S.; Gonzalez-Carreno, T.; Serna, C. J., *J.Phys. D-Appl. Phys.* **2003,** 36, (13), R182-R197.
2. Carpenter, E. E.; Kumbhar, A.; Wiemann, J. A.; Srikanth, H.; Wiggins, J.; Zhou, W. L.; Connor, C. J., *Mater. Sci. Eng., A* **2000,** 286, 81.
3. Chang, W. S.; Park, J. W.; Rawat, V.; Sands, T.; Lee, G. U., *Nanotechnology* **2006,** 17, (20), 5131-5135.
4. Chiang, I. C.; Chen, D. H., *Adv. Funct. Mater.* **2007,** 17, (8), 1311-1316.
5. Cho, S. J.; Jarrett, B. R.; Louie, A. Y.; Kauzlarich, S. M., *Nanotechnology* **2006,** 17, (3), 640-644.
6. Crespo, P.; LitraÌ□n, R.; Rojas, T. C.; Multigner, M.; de la Fuente, J. M.; SaÌ□nchez-LoÌ□pez, J. C.; GarciaÌ□, M. A.; Hernando, A.; PenadeÌ□s, S.; FernaÌ□ndez, A., *Phys. Rev. Lett.* **2004,** 93, 087204-1.
7. Levin, C. S.; Hofmann, C.; Ali, T. A.; Kelly, A. T.; Morosan, E.; Nordlander, P.; Whitmire, K. H.; Halas, N. J., *ACS Nano* **2009,** 3, (6), 1379-1388.
8. Lisiecki, I., *J. Phys. Chem B* **2005,** 109, 12231.
9. Liu, H. L.; Wu, J. H.; Min, J. H.; Lee, J. H.; Kim, Y. K., *J.Nanosci. Nanotechnol.* **2009,** 9, (2), 754-758.
10. Prodan, E.; Radloff, C.; Halas, N. J.; Nordlander, P., *Science* **2003,** 302, (5644), 419-422.
11. Sun, Q., *Phys. Rev. B,* **2006,** 73, (13).
12. Wang, L. Y.; Luo, J.; Fan, Q.; Suzuki, M.; Suzuki, I. S.; Engelhard, M. H.; Lin, Y. H.; Kim, N.; Wang, J. Q.; Zhong, C. J., *J.Phys. Chem. B* **2005,** 109, (46), 21593-21601.

13. Chen, M.; Yamamuro, S.; Farrell, D.; Majetich, S. A., *J. Appl. Phys.* **2003,** 93, (10), 7551-7553.

14. Gangopadhyay, P.; Gallet, S.; Franz, E.; Persoons, A.; Verbiest, T., *Ieee Transactions on Magnetics* **2005,** 41, (10), 4194-4196.

15. Zelenakova, A.; Kovac, J.; Kavecansky, V.; Zelenak, V *Acta Physica Polonica A* **2008,** 113, (1), 533-536.

16. Ban, Z. H.; Barnakov, Y. A.; Golub, V. O.; O'Connor, C. J., *J.Mater. Chem.* **2005,** 15, (43), 4660-4662.

17. Carpenter, E. E.; Kumbhar, A.; Wiemann, J. A.; Srikanth, H.; Wiggins, J.; Zhou, W. L.; O'Connor, C. J., *Mater. Sci. Eng.* **2000,** 286, (1), 81-86.

18. Fortin, J.-P.; Wilhelm, C.; Servais, J.; MÃ©nager, C.; Bacri, J.-C.; Gazeau, F., *J. Am. Chem.Soc.* **2007,** 129, (9), 2628-2635.

19. Grieve, K.; Mulvaney, P.; Grieser, F., *Curr. Opin. Colloid Interface Sci.* **2000,** 5, 168.

20. Pileni, M. P., *Nat. Mater.* **2003,** 2, 145.

21. Pileni, M. P. J., *J. Exp. Nanosci.* **2006,** i.

22. Zhou, W. L.; Carpenter, E. E.; Lin, J.; Kumbhar, A.; Sims, J.; O'Connor, C. J., *Eur. Phyi. J. D* **2001,** 16, (1-3), 289-292.

23. Halas, N. J., *MRS Bull.* **2005,** 30, 362.

24. Lin, J.; Zhou, W. L.; Kumbhar, A.; Wiemann, J.; Fang, J. Y.; Carpenter, E. E.; O'Connor, C. J., *J.Solid State Chem.* **2001,** 159, (1), 26-31.

25. Yin, M.; Oâ€™Brien, S., *J. Am. Chem. Soc.* **2003,** 125, 10180.

26. Chiang, I. C.; Chen, D. H., *Adv. Funct. Mater.* **2007,** 17, 1311.

27. Cho, S. J.; Jarrett, B. R.; Louie, A. Y.; Kauzlarich, S. M., *Nanotechnology* **2006,** 17, 640.

28. Park, J.; An, K.; Hwang, Y.; Park, J. G.; Noh, H. J.; Kim, J. Y.; Park, J. H.; Hwang, N. M.; Hyeon, T., *Nat. Mater.* **2004,** 3, 891.

29. Petit, C.; Pileni, M. P., *J. Phys. Chem.* **1988,** 92, 2282.

30. Pileni, M. P., *J. Phys. Chem.* **1993,** 97, 6961.

31. Pileni, M. P., *Langmuir* **2001,** 17, 7476.

32. Brust, M.; Bethell, D.; Kiely, C. J.; Schiffrin, D., *J. Langmuir* **1998,** 14, 5425.

33. Brust, M.; Bethell, D.; Schiffrin, D. J.; Kiely, C., *J. Adv. Mater.* **1995,** 7, 795.

34. Brust, M.; Walker, M.; Bethell, D.; Schiffrin, D. J.; Whyman, R., *J. Chem. Soc., Chem. Commun.* **1994**, 801.

35. Prasad, B. L. V.; Stoeva, S. I.; Sorensen, C. M.; Klabunde, K., *J. Langmuir* **2002,** 18, 7515.

36. Pileni, M. P., *Langmuir* **1997,** 13, (13), 3266-3276.

37. Prodan, E.; Nordlander, P.; Halas, N. J., *Chem. Phys. Lett.* **2003,** 368, 94.

38. Prodan, E.; Radloff, C.; Halas, N. J.; Nordlander, P., *Science* **2003,** 302, 419.

39. Saha, D. K.; Koga, K.; Takeo, H., *Nanostructured Mater.* **1997,** 8, (8), 1139-1147.

40. Shevchenko, E. V.; Bodnarchuk, M. I.; Kovalenko, M. V.; Talapin, D. V.; Smith, R. K.; Aloni, S.; Heiss, W.; Alivisatos, A. P., *Adv. Mater.* **2008,** 20, 4323.

41. Kalyuzhny, G.; Schneeweiss, M. A.; Shanzer, A.; Vaskevich, A.; Rubinstein, I., *J. Am. Chem. Soc.* **2001,** 123, 3177.

42. Kelly, K. L.; Coronado, E.; Zhao, L. L.; Schatz, G. C., *J. Phys. Chem. B* **2003,** 107, 668.

43. Kreibig, U.; Vollmer, M., *Optical Properties of Metal Clusters; Springer: Berlin* **1995,** 25, 532.

44. Wang, L. Y.; Luo, J.; Maye, M. M.; Fan, Q.; Qiang, R. D.; Engelhard, M. H.; Wang, C. M.; Lin, Y. H.; Zhong, C. J., *J.Mater. Chem.* **2005,** 15, (18), 1821-1832.

45. Dahal, N.; Chikan, V.; Jasinski, J.; Leppert, V. J., *Chem. Mater.* **2008,** 20, (20), 6389-6395.

46. Wikander, K.; Petit, C.; Holmberg, K.; Pileni, M.-P., *Langmuir* **2006,** 22, (10), 4863-4868.

47. Gole, A.; Stone, J. W.; Gemmill, W. R.; zur Loye, H. C.; Murphy, C. J., *Langmuir* **2008,** 24, 6232.

48. Morrish, A. H., *The Physical Principles of Magnetism*. 1965.

CHAPTER 3 - Synthesis and characterizations of Water-Soluble Iron-Gold Alloy Nanoparticles

Introduction

Bimetallic nanoparticles are promising to significantly extend the functionality of single component metallic catalysts. Bimetallic nanoparticles containing gold as one of the elements have begun to show opportunities for developing constituents of fuel cell catalysts.[1-4] Several research groups have already demonstrated diverse production techniques of bimetallic nanoparticles of this type. A large portion of the studies focus on Fe-Au core-shell nanoparticles.[5-11] The combination of either iron or iron oxide core and gold shell is specifically appealing because gold is a noble metal and provides an established platform for surface functionalization.[10, 11] Additionally, the shell provides protection against oxidation and helps to maintain long-term stability of the particles.[5-11] Unfortunately, the core-shell particles have their own challenges. First, the gold shell forms a poor diffusion barrier because of the high density of the grain boundaries at the gold surface.[12-14] Second, it is somewhat difficult to control the uniformity and thickness of the metal coating. On the other hand, with Fe-Au alloy nanoparticles, these effects may be minimized.

Fe-Au alloy nanoparticles are solid solutions where iron atoms substitute gold sites in the face center cubic lattice. At low iron content the gold-rich fcc solid solution is the predominant phase and exhibits magnetic spin glass properties.[15-17] Incorporation of even a little amount of iron increases the density of defective sites in the alloy nanoparticles and helps to increase the catalytic activity. In the literature, there are only a few reports concerning the preparation of Fe-Au alloy nanoparticles; pulsed laser deposition,[15] carbon film deposition at very high temperature

(1600 K) in the presence of helium flow[12] and electro deposition.[13] Very recently Chiang et al. prepared Fe-Au alloy nanoparticles by reduction of gold acetate and thermal decomposition of iron pentacarbonyl at 300^{o}C.[14] At this point, a more robust synthesis is needed to better assist the broader exploitation of the Fe-Au nanoparticles.

In this paper, a relatively low temperature synthesis of Fe-Au alloy nanoparticles is presented using two different iron precursors. The size of the nanoparticles ranges between 4 to 6 nm. The iron content of the Fe-Au nanoparticles that is calculated form Vegards law is ~14.8± 4.7 mole % of iron.[12, 13, 15] The UV-visible absorption spectra of Fe-Au alloy nanoparticles are different from pure iron or gold nanoparticles. Namely, if the plasmon resonance of the gold nanoparticle is considered as a reference, then the alloy nanoparticles show a significant red shift (approximately 100 nm).

Experimental Section

Table 1 shows the synthesis condition, particle size, composition and stability of Fe-Au alloy nanoparticles.

Sample Prepared	Precursors		Temperature	Ligand used	Reducing agent	Particle size / nm	Composition at 1:1 mole ratio
	Iron	Gold					
Fe-Au alloy	$Fe(CO)_5$	$HAuCl_4.3H_2O$	110^{o}C	3-mercapto-1-propane Sulphonic acid	$NaBH_4$	3.8±1.0	14.8 ± 4.7 mole % of iron
Fe-Au alloy	$FeSO_4.7H_2O$	$HAuCl_4.3H_2O$	110^{o}C	3-mercapto-1-propane Sulphonic acid	$NaBH_4$	4.9±1.0	Not calculated

Fe-Au nanoparticles are produced via iron sulphate heptahydrate and iron pentacarbonyl. The description of the synthesis is described below. The synthesis condition, precursors used during the synthesis, their composition, size and stability of the samples are presented in table 1.

Preparation of Fe-Au Alloy Nanoparticles from Iron Sulphate Heptahydrate:

In a typical synthesis, (0.08 mole) of (di-n-dodecyl) dimethylammonium bromide (99%) (DDAB) is dissolved in 20 ml of toluene (99%) in a three neck flask under argon atmosphere. The solution is stirred for 15 minutes at 110^{o}C. (0.02 mole) of freshly prepared aqueous iron sulphate heptahydrate (99 %) in 0.5 ml double distilled water is injected rapidly. The solution becomes turbid right away. After two minutes, 1.5 ml of sodium borohydride (98 %) 2M in aqueous solution is added. The solution turns to ash color with black colloids floating all around the solution. 20 minutes later, a solution containing gold chloride is injected into the iron nanoparticle seed solution. The 1.5 ml gold chloride solution consists of (0.02 mole) of gold (III) chloride trihydrate, (99 %) and (0.6 milli mole) 3-mercapto-1-propansulphonicacid sodium salt (90 %). When the color of the solution turns red, 1.5 ml 2M aqueous sodium borohydride is again added to reduce the gold chloride to gold. The color of the solution turns purple and slowly the purple color disappears. The final solution has a very faint reddish color. The solution is stirred for 30 minutes. Finally, 0.5 ml of 2M aqueous sodium borohydride is added to the solution. The entire solution is heated at 84^{o}C for three hours.

Preparation of Fe-Au Alloy Nanoparticles from Iron Pentacarbonyl:

Alternatively, Fe-Au alloy nanoparticles are prepared under argon atmosphere via thermal decomposition of iron pentacarbonyl. In a typical synthesis, (0.002 mole) of iron pentacarbonyl (99 %) is injected at 110^{o}C into a three-neck flask containing (0.08 mole) DDAB and 20 ml of toluene. Initially, the color of the solution is yellow and it immediately turns to reddish color. A black solution is obtained after heating it for 20 minutes. Gold precursors and ligands are added as mentioned above. 2 ml of aqueous sodium borohydride is added dropwise into the entire solution. Finally, a black greenish shining powder of iron-gold alloy nanoparticles is obtained. For purification, the crude mixture is mixed with ethanol (99 %) and centrifuged for 15 minutes at 7000 rpm. In the first step, the precipitate is washed with ethanol and chloroform. This step is repeated several times. The dark greenish solid sample is collected and vacuum dried for 10 hours. The dried sample is placed in magnetic field for magnetic separation. Only the magnetic part is collected for further characterization. The nanoparticles are easily dispersed in water. The approximate yield of the reactions is 30% by weight.

Results and Discussion

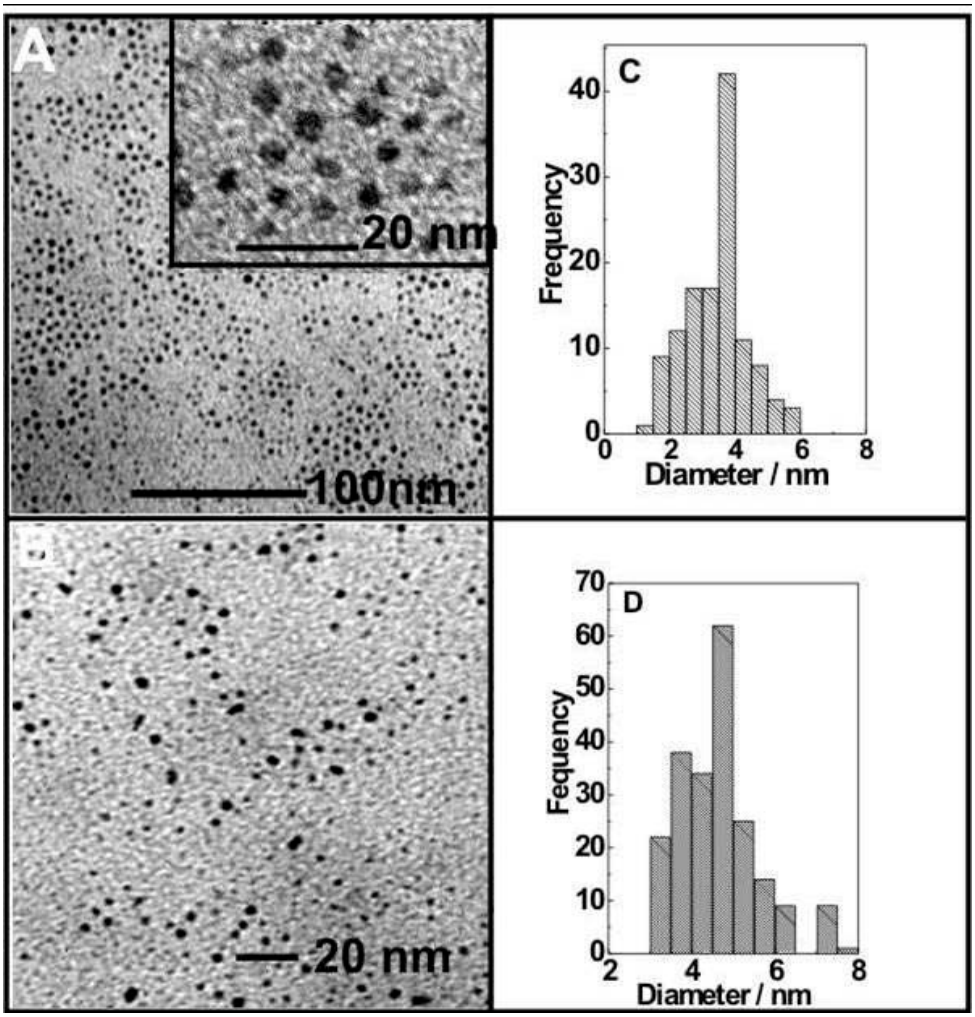

Figure 3-1a TEM image of iron-gold alloy nanoparticles obtained from Fe^0 precursor. Fig. 3-1b shows TEM images of iron-gold alloy nanoparticles obtained from Fe^{2+} precursor Fig. 3-1c is the size histogram of alloy nanoparticles from Fe^0 precursor. Fig. 3-1d is the size histogram of alloy nanoparticles from Fe^{2+} precursor.

Figure 3-1a represents the low resolution Transmission Electron Microscope (TEM) image of Fe-Au alloys obtained from Fe^0 precursor, iron pentacarbonyl with initial molar ratio of

1:1. Figure 3-1c shows the histogram of the corresponding particles obtained from Fe^0 precursor. The average size of the particles is calculated to be 3.8±1.0 nm. Figure 3-1b represents the TEM image of Fe-Au alloy obtained from Fe^{2+} precursor revealing the inhomogeneous nucleation of iron on gold. The particle distribution shows some degree of polydispersity. The histogram of the Fe-Au nanoparticles from Fe^{2+} precursor is indicated in Figure 3-1d. The average size of these particles is found to be 4.9±1.0 nm. Figure 3-1a inset shows the higher magnification image of the Fe-Au nanoparticles obtained form Fe^0 precursor. Within the resolution of the low resolution TEM, the image reveals irregularly shaped, multifaceted nanocrystals with sharp edges.

Figure 3-2 shows the UV-visible absorption spectra of Fe-Au alloy nanoparticles prepared using either Fe^{2+} or Fe^0 as an iron source. Both alloy nanoparticles show two dominant absorption peaks. The nanoparticles that are obtained from Fe^0 precursor shows the first absorption peak at 395 nm and the second peak at 650 nm. The initial molar ratio of the iron to gold precursor used in this case is 1:2. On the other hand, nanoparticles obtained from Fe^{2+} precursor shows the peaks at approximately 395 nm and 662 nm, which are shifted relative to the surface plasmon peak of the gold nanoparticles. Gold nanoparticles were prepared under identical conditions to that of alloy nanoparticles. No gold absorption peak has been observed in the plasmon peak of alloy Fe-Au nanoparticles prepared from both Fe^{2+} and Fe^0 precursor. In the case of gold nanoparticles, there is an absence of first peak at shorter wavelength region and shows only the characteristics peak of gold nanoparticles at 534 nm is observed.

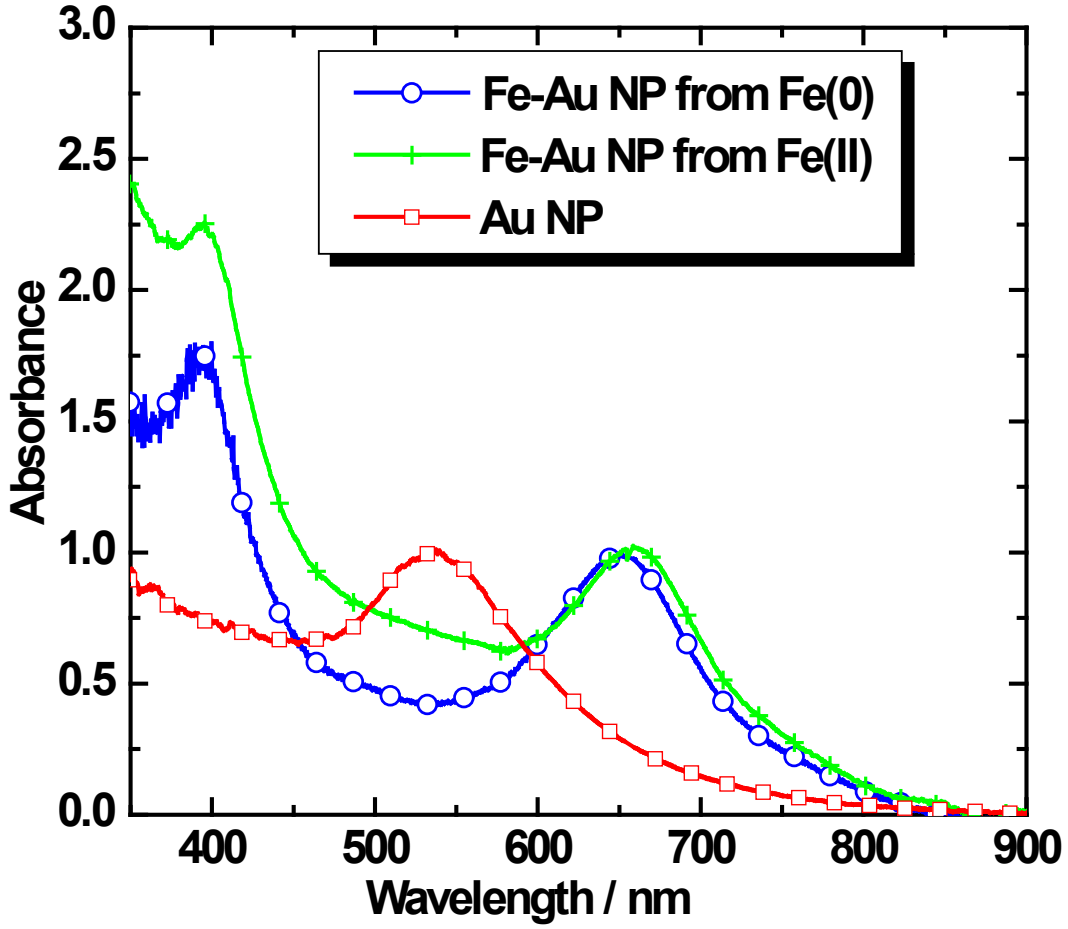

Figure 3-2 UV-visible absorption spectra (in water) of pure gold nanoparticles (open square) and gold iron alloy nanoparticles (NP) obtained from Fe^{2+} (plus) and Fe^{0} precursor(circle).

The shifted absorption peaks of the Fe-Au alloy nanoparticles relative to the gold nanoparticles could be the result of change in the electron density or the result of the sharp edges of icosahedral structure. A shift in the position of a plasmon peak due to sharp edges has been reported previously in the case of silver nanoparticles with triangular geometry.[18] The concept of

hybridization of plasmon bands[19, 20] and cavity resonance; obviously does not apply since the nanoparticles are not core/shell structures. Another plausible explanation based on literature for the shift is the perturbation of electron cloud oscillation due to surface gold atoms. Specifically, a thin gold layer on the alloy nanoparticles could increase the dielectric constant of the immediate proximity of the particle, plus the plasmon oscillation of a thin gold layer could couple with plasmon oscillation of the alloy nanoparticles and the gold may also transfer electrons to the alloy nanoparticles, resulting in a shift of the plasmon peak.[4, 8, 14, 21] This explanation seems to correlate reasonably well with experiment. The absorption peak is slightly tunable depending on the amount of iron incorporated into gold. In case of gold coated nanoparticles, there is usually a red shift in the surface plasmon peak position with the decrease of shell thickness and a blue shift with the increase of shell thickness.[8, 11, 14, 22] Figure 3-3 shows a trend similar to that of core-shell nanoparticles, but less pronounced (20 nm and 12 nm). There is a blue shift in the 662 nm peak position with increasing amount of gold. When the Fe /Au molar ratio is 1:1, the plasmon peak position is located at 662 nm. On the other hand, when Fe-Au molar ratio is changed to 1:2 the plasmon peak position is blue shifted to 650 nm and 642 nm for 1:3 initial molar ratio of iron to gold precursor. For the first peak, the trend is identical and blue shifted from 397 nm for 1:1 initial molar ratio of iron to gold and 385 nm for 1:3 initial molar ratio of iron to gold precursor. For comparison, the spectrum of water-soluble gold nanoparticles prepared in the absence of iron is also presented in Figure 3-3. The plasmon peak position of gold nanoparticles is centered at 534 nm. If the amount of gold during the synthesis of Fe-Au alloy nanoparticles is further increased, the gold plasmon peak appears at approximately 506 nm along with the alloy nanoparticle peaks. The nucleation of the gold nanoparticle occurs at about 1:10 initial molar ratios of Fe-Au, which agrees well with the molar composition of the alloy nanoparticles. This

observation holds an important clue as to how these nanoparticles are formed. From this, it can be concluded that no heterogeneous nucleation takes place, but gold seems to nucleate along with iron to form the alloy nanoparticles. The lack of heterogeneous nucleation suggests that the alloy particles are thermodynamically more stable than separate gold nanoparticles. No similar statements can be made in comparison with iron nanoparticles since the iron nanoparticle have no distinct plasmon absorption in the visible spectrum.

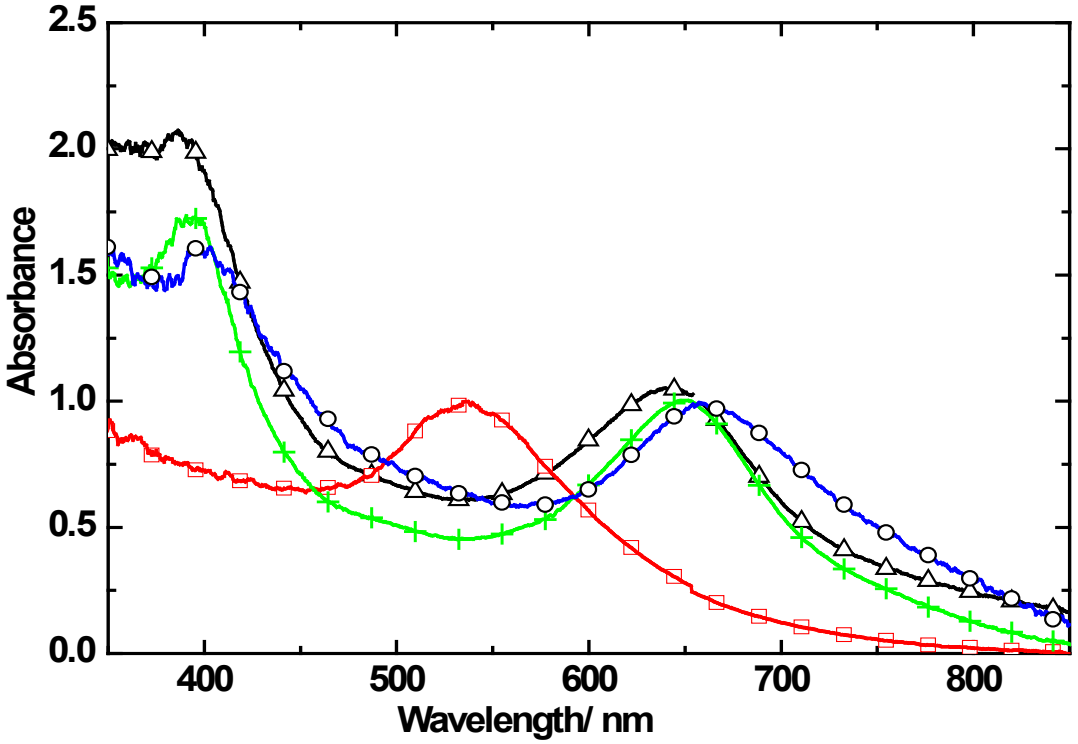

Figure 3-3 represents UV-Visible absorption spectra (in water) for pure gold and iron-gold alloy nanoparticles synthesized from Fe^0 precursor with various molar ratios. The molar ratios of iron and gold are 1:1, 1:2 and 1:3 indicate by circle, cross and triangle, respectively.

Figure 3-4 curve I shows the XRD patterns of pure gold nanoparticles and curve II and III represent the Fe-Au alloy nanoparticles which are obtained from Fe^0 and Fe^{2+} with 1:1 initial molar ratio of precursor's molecules. The XRD pattern of the alloy nanoparticles obtained from the Fe^0 precursor (curve II) reveals that the samples are crystalline. There is broadening due to smaller particle size and considerable change in 2θ angle compared to pure gold nanoparticles prepared under identical conditions. The shifting of each peak position to higher 2θ values in the alloy sample obtained from Fe^0 indicates softening of the lattice constant and this is due to incorporation of iron into the gold surface. Figure 3-4 inset shows the change in 2θ angle of 111 atomic reflections of alloy nanoparticles from the Fe^0 precursor that are taken form (curve II) and pure gold nanoparticles (curve I). The 2θ angles at 38.67°, 44.81°, 65.32°, 78.05° and 82.54° in Figure 4a curve II and III correspond to (111), (200), (220), (311) and (222) fcc atomic reflections planes of alloy nanoparticles.[7, 8, 10] The degree of crystallinity and homogeneity of the sample is best displayed by the alloy nanoparticles obtained from the Fe^0 precursor. The XRD data shows that there is no phase segregation of the elements in the alloy nanoparticles from Fe^0 precursor. The XRD pattern of the alloy particles obtained from the Fe^{2+} precursor is also (curve III) displayed in Figure 3-4. The features of the alloy nanoparticle from Fe^{2+} precursor indicate poor crystallinity and inhomogeneity of sample. Specifically, Figure 4a (curve III) shows the peaks of gold and iron alloy and the various reflections of iron oxide (Fe_3O_4) nanoparticles. The XRD peaks at 2θ, 30.2° 35.5°,43.2°, 53.2°, 57.2° and 62.8° correspond to (220), (311), (400), (422), (511) and (440) lattice planes for Fe_3O_4 nanoparticles.[8, 22, 23] This is different form the work of Glavee et al in which they reported the formation of mixed oxides of iron, iron and iron boride nanoparticles upon $NaBH_4$ reduction of Fe^{2+} in aqueous solution.[24] A plausible explanation of this present experimental observation is that some of the iron atoms on the surface

of alloy nanoparticles are oxidized while using Fe^{2+} precursor. In the Fe^{2+} sample, the (220), (311) and (222) atomic reflection planes for the Fe-Au alloy nanoparticles are small. Synthesis of alloy nanoparticles from the Fe^{2+} precursor results in a mixture of iron oxide (Fe_3O_4) and gold. From these results, one can conclude that Fe^0 precursor is better source to obtain alloy nanoparticles under the experimental conditions used in this study.

The crystallite size of nanoparticles is determined by using the Debye-Scherrer equation: $L = (0.88\lambda) / (\beta Cos\theta)$, where λ is the X-ray wavelength in nm, β is the intrinsic peak width in radians (2θ), the β value is calculated by Gaussian fitting of the most intense atomic reflection (111) peak of iron/gold alloy nanoparticles, θ is the Bragg angle and 0.88 is the Debye-Scherrer constant.[10] The crystallite size of Fe-Au alloy nanoparticles prepared from Fe^{2+} precursor calculated from the Fe-Au (111) atomic reflection plane is 6±1.0 nm and the crystallite size of the nanoparticles obtained from Fe^0 precursors is 4.9±1.0 nm . These values are slightly higher than the TEM data (4.9±1.0 nm and 3.8±1.0 nm), but consistent with the HRTEM images.

Table 2 shows the 2θ angles of Au and Fe-Au alloy nanoparticles. The data in table 2 indicate that the 2θ angles of Fe-Au alloy nanoparticles of different planes are higher than the corresponding 2θ angles of pure gold. The changes in 2θ angles indicate the reduction of the lattice constant due to alloying gold with iron.[13] The reason of reduction lattice constant is that the atomic radius of iron (126 pm) is smaller than pure gold (144 pm); therefore the incorporation of iron into gold reduces the lattice constant. An important question here is why the structure is not collapsed after the incorporation of iron. A possible explanation is that the bulk strain of the alloyed particles would become lower by mixing lower atomic radius iron, even if the alloyed nanoparticles grow larger than the critical size of gold

nanoparticles.

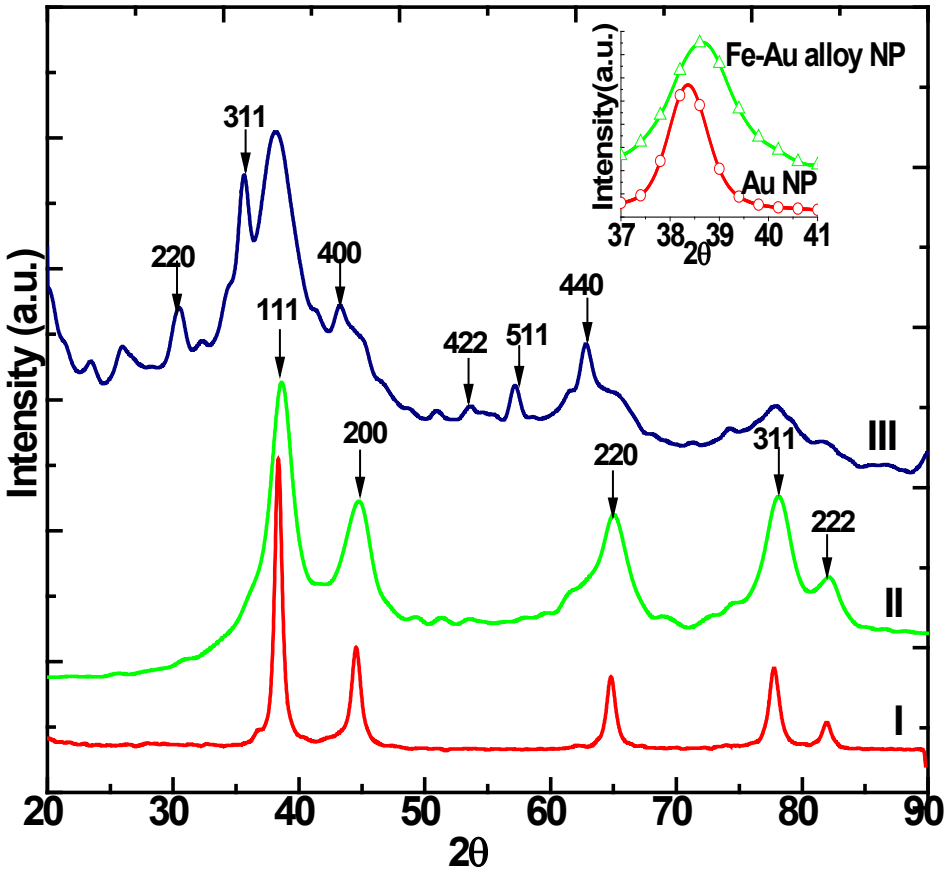

Figure 3-4 XRD patterns of pure gold nanoparticles prepared under identical conditions to that of alloy nanoparticles (curve I) and iron-gold alloy nanoparticles obtained from Fe^0 (curve II) and Fe^{2+} (curve III) precursors. Fig 3-4a inset shows the shift of the (111) atomic reflection plane of iron-gold alloy nanoparticles from Fe^0 precursor (open triangle) relative to gold nanoparticles (open circle).

Table 2 Lattice constants of Fe-Au alloy and pure gold nanoparticles obtained from (111), (200), (220), (311) and (222) atomic reflections.

Pure Au Nanoparticles					Fe-Au Alloy Nanoparticles from Fe^0				
2θ	Lattice spacing d in Å	Lattice planes	Lattice constant in Å	Average lattice constant in Å	2θ	Lattice spacing d in Å	Lattice planes	Lattice constant in Å	Average Lattice constant in Å
38.38	2.344	111	4.061		38.67	2.327	111	4.031	
44.62	2.030	200	4.060		44.81	2.022	200	4.044	
64.83	1.437	220	4.067	4.067±0.0375	65.32	1.428	220	4.040	4.044±0.0375
77.79	1.227	311	4.071		78.05	1.224	311	4.058	
81.86	1.176	222	4.076		82.54	1.168	222	4.048	

The Fe-Au sample which is obtained from the Fe^{2+} precursor is susceptible to oxidation and mostly it remains in the mixture of iron oxide and gold as examined by XRD analysis. Therefore, the lattice constant and composition is calculated based on alloy sample prepared form Fe^0 precursor. The average lattice constants of pure gold and Fe-Au alloy nanoparticles are 4.067±0.037 Å and 4.044±0.037 Å, respectively. The reported literature values of pure gold and Fe-Au alloy nanoparticles are 4.078 Å and 4.055 Å, [13] 4.031±0.050, [15] 4.035 and 3.995 Å [25, 26] respectively. Therefore, the lattice constants observed herein are within 0.2-0.3 % of experimental error. The reported value of the corresponding lattice constant of fcc bulk iron is

3.590 Å. Obviously, the magnitude of lattice constant of the Fe-Au alloy nanoparticles is between pure gold and pure iron nanoparticles. The substitution incorporation of impurity element allows the application of Vegard's law to estimate the relative portion of the constituents of an alloy sample. According to Vegard's law, there is a linear relationship between the impurity concentration and the lattice constant. The lattice constant of alloy as a function of iron composition *x* can be approximated using the following formula. [27]

$$a_{Fe-Au} = (1-x)a_{Au} + xa_{Fe} \qquad (1)$$

where, a_{Fe-Au} is the lattice constant of the alloy nanoparticles prepared from Fe^0 precursor, a_{Au} and a_{Fe} are the lattice constant of gold and iron, respectively. While using the experimental and calculated lattice constant for pure gold and Fe-Au alloy in equation 1 the molar fraction of iron in the alloyed nanoparticles is found to be 4.7±1.5 %. When the lattice parameters of the bulk Fe-Au alloys (15.7 % and 20 % of iron content) [15, 25, 26] are used instead of the pure gold and iron, the composition is 14.8± 4.7% of iron.[28] This result is agrees well with the composition that is obtained from energy disperse X-ray analysis and compositions of the previously synthesized Fe-Au alloy nanoparticles (6.50 %, [13] 11 %, [12] and 17 % [15] of iron).

The washed, dry sample can be stored for several months. Figure 3-5 curve (I) shows the XRD pattern of the Fe-Au alloy obtain from Fe^0 precursor stored in air tight vessel for six months. The XRD pattern shows that there is not a phase segregation of alloy nanoparticles. The XRD pattern is similar to Figure 3-4 (curve I) which is obtained immediately after synthesis. When the sample is stored dissolved in water for several days, the distinct green color of the sample disappears and brown precipitates form. The XRD pattern of the precipitate is shown in Figure 4b (II). The pattern still shows the position of alloy peaks, but broader with additional peaks of iron oxides (Fe_3O_4) due to oxidation of iron. The additional peaks are due to iron oxide

(Fe_3O_4) and correspond to (220), (311), (422) and (440) atomic reflections. This result shows that there is a change in morphology and size of alloy nanoparticles due to oxidation of iron and the phase segregation of gold. When the sample is annealed at 500^oC in air (Figure 3-5 (III)) sharp peaks due to aggregation and crystal growth is observed. Comparison of the (111) reflection of the annealed Fe-Au alloy nanoparticles and the oxidized samples are shown in the inset of Fig. 4b. The annealed sample peak position is shifted completely to the peak position of gold whereas the oxidized sample is not completely shifted to the original peak position of gold (38.2^o). The results imply that there is complete phase segregation in case of the annealed sample while with the oxidized sample only partial phase segregation. The major driving force for the segregation of alloy nanoparticles is to minimize its surface energy. At room temperature the surface free energies for thin film of iron and gold is 2.9 Jm^{-2} and 1.9 Jm^{-2} respectively, [29] which suggests that in the absence of oxygen the gold is favored at the surface of the particles.

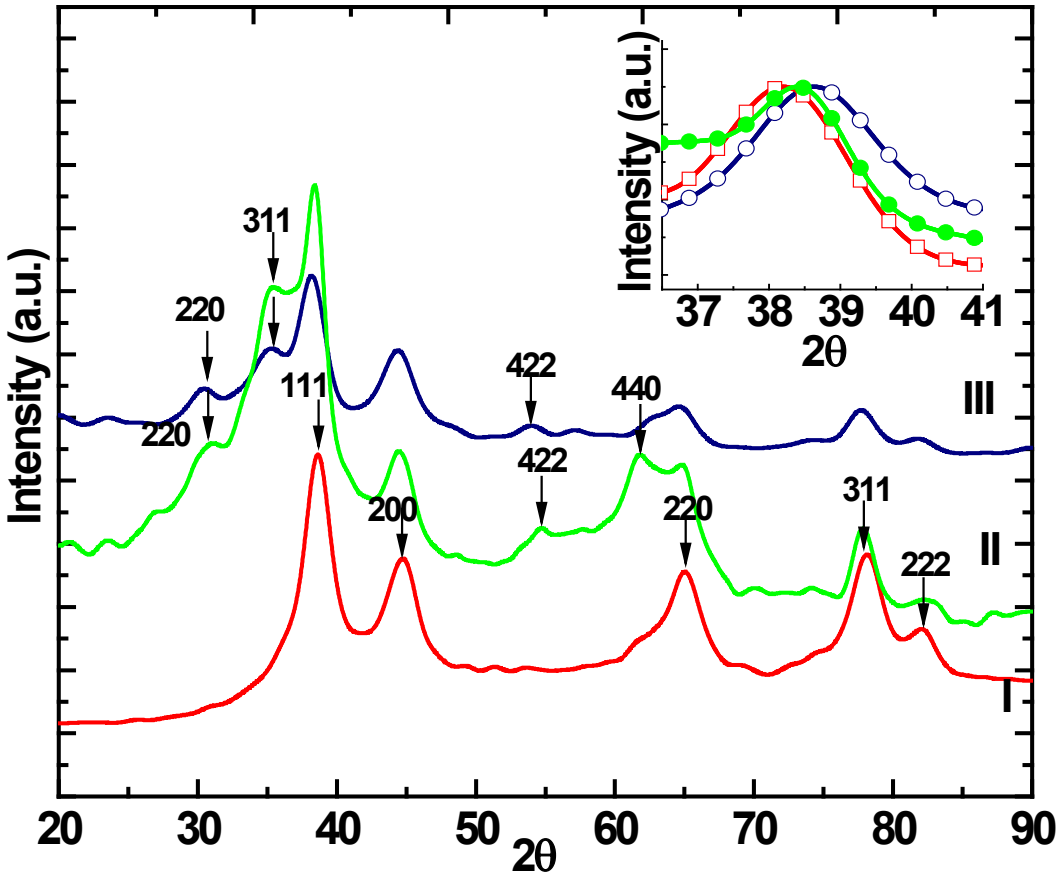

Figure 3-5 (I) is the powder XRD of Fe-Au alloy prepared form Fe^0 precursor and stored in air tight vessel for several months. (II) is the powder XRD of partially oxidized particles stored in water several days. (III) is the powder XRD of the same particles annealed to 500°C in air immediately after synthesis. Inset shows the shift in 2θ angle from (111) atomic reflection plane of Fe-Au alloy of the freshly prepared sample (open circle), oxidized (closed circle) and annealed sample at 500 °C (open square).

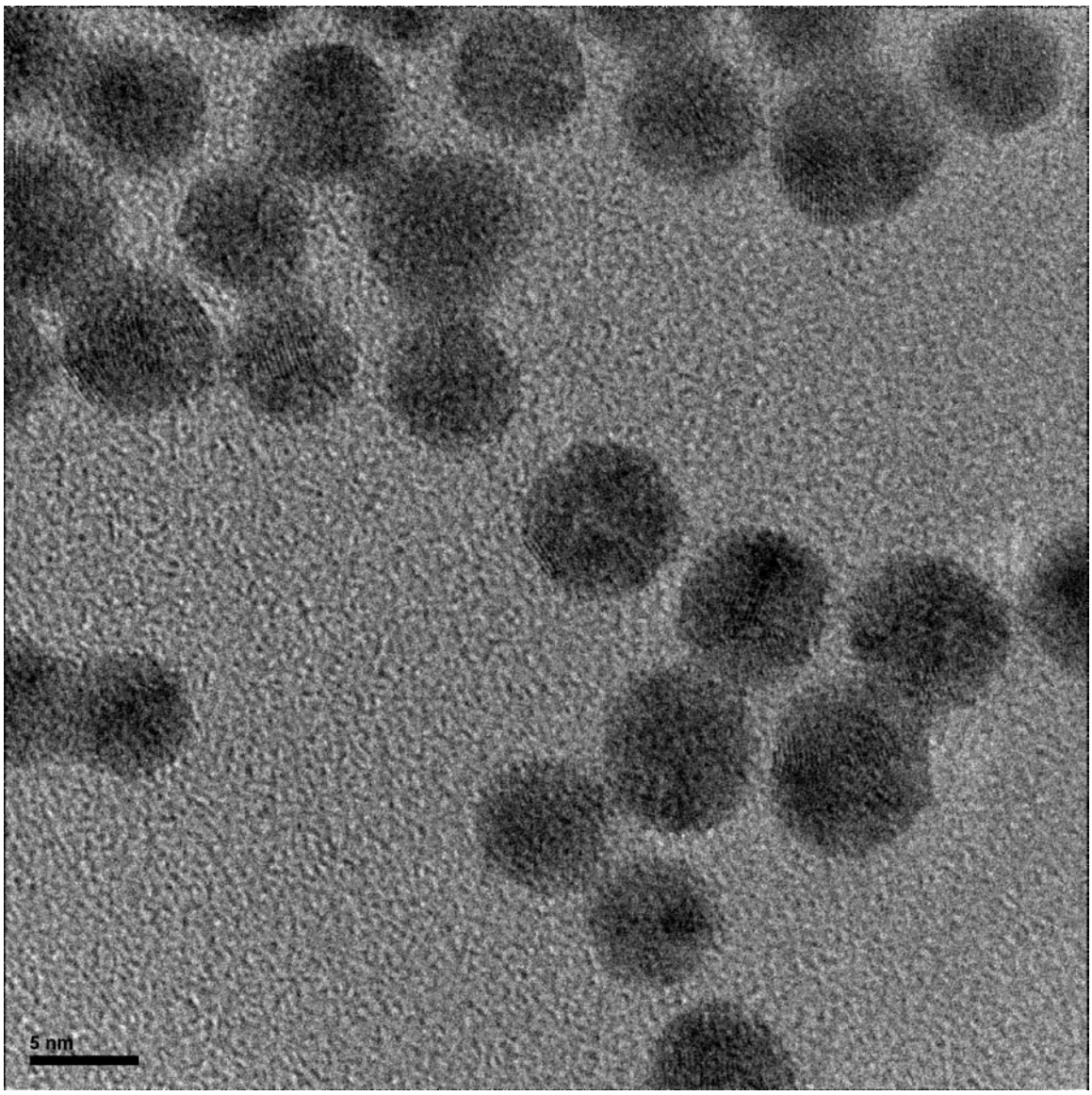

Figure 3-6 HRTEM image of Fe-Au alloy nanoparticles obtained from Fe^0 precursor with 1:1 initial molar ratio of precursor molecules. The image shows majority of the particles possess icosahedral structures.

Figure 3-6 represents the HRTEM images of Fe-Au alloy nanoparticles from the Fe^0 precursor with initial molar ratio of precursor's molecules 1:1. The figure clearly shows not only that the incorporation of gold into iron changes the structure from bcc to fcc, but it also indicates the presence of stable icosahedral structures. Saha et. al[12] have also shown the presence of icosahedral structures using a very high temperature heating (1600K) synthesis method. HRTEM results from this work show very similar structure and morphology. Figure 3-7a and 3-7b highlighted the icosahedral crystal structure of alloy nanoparticles with nearly three and two fold axis of symmetry. Figure 3-7c and 3-7d are the simulated images of the same particles representing clearly the three fold and two fold axis of symmetry in these structures.

Koga et.al[30] also showed the presence of icosahedral structure in the case of gold nanoparticles. During a HRTEM study conducted in conjunction with extensive tilting of gold nanoparticles they have found the presence of icosahedral structure either for 3 nm size or above 8 nm size and not in the 4-6 nm size range. As shown in Figure 5, the majority of the particles possess icosahedral structures in the 3-6 nm size range. Interestingly, there is no observance of decahedral structure like gold nanoparticles. This indirect piece of evidence further supports that there is alloying of iron in gold and change in crystal structure to the icosahedral form. Most of the nanoparticles reveal the Fe-Au alloy (111) lattice fringes with the lattice spacing of ~ 0.22 nm. For some of the nanoparticles, the Fe-Au alloy (200) lattice fringes with the spacing of ~0.20 nm can also be seen, however as opposed to the XRD, the HRTEM technique do not provide sufficient d-spacing measurement precision to differentiate between pure gold and Fe-Au alloy.

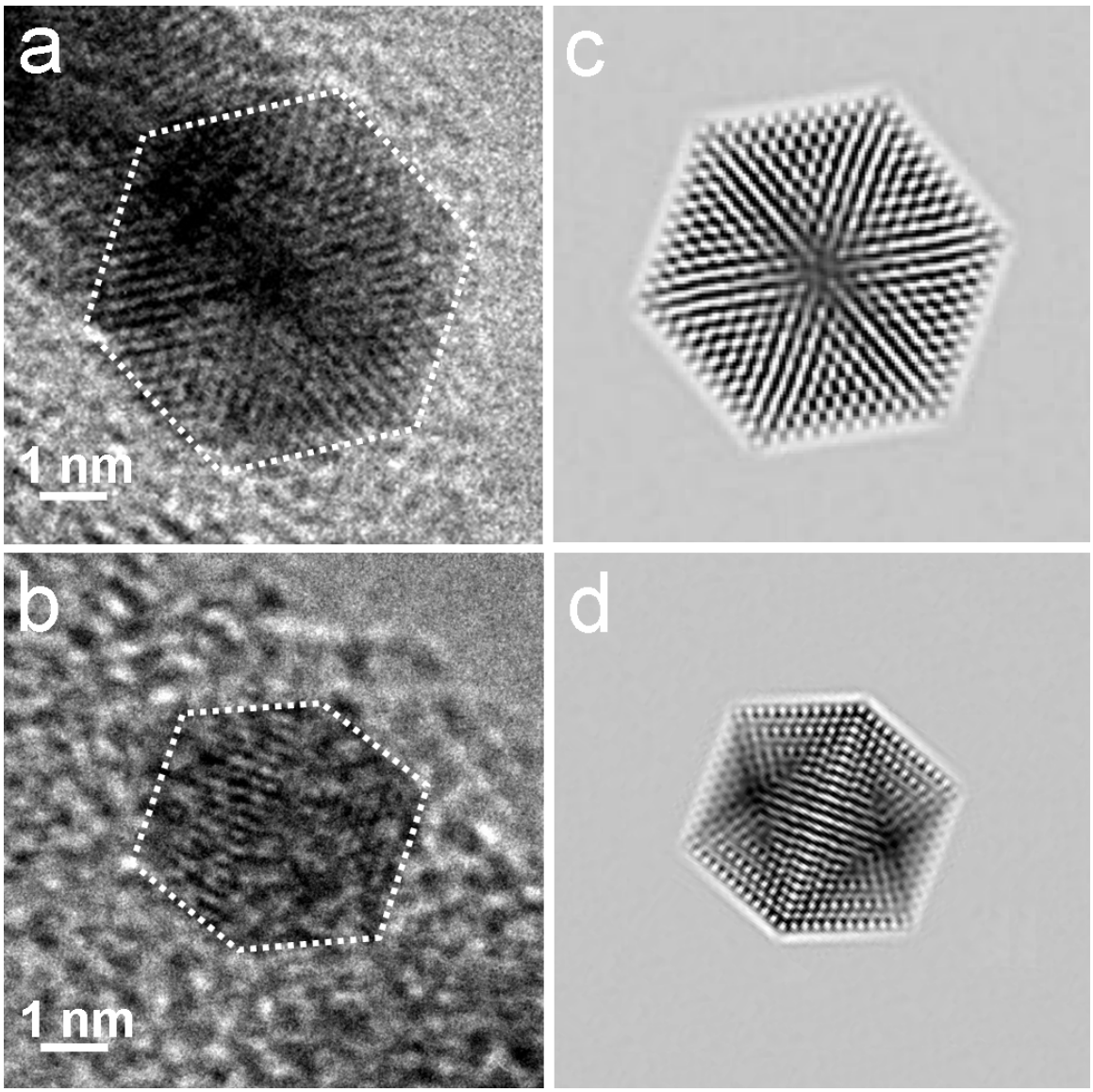

Figure 3-7 a,b: HRTEM images of two Fe-Au alloy nanoparticles formed in the icosahedral structure from Fe^0. These particles are oriented: (a) almost along the 3-fold axis and (b) close to the 2-fold axis, respectively. c, d: Corresponding theoretical HRTEM images from Saha et al.[76] calculated for an icosahedral model structure. The images are reproduced by permission of the editorial board of The European Physical Journal D.

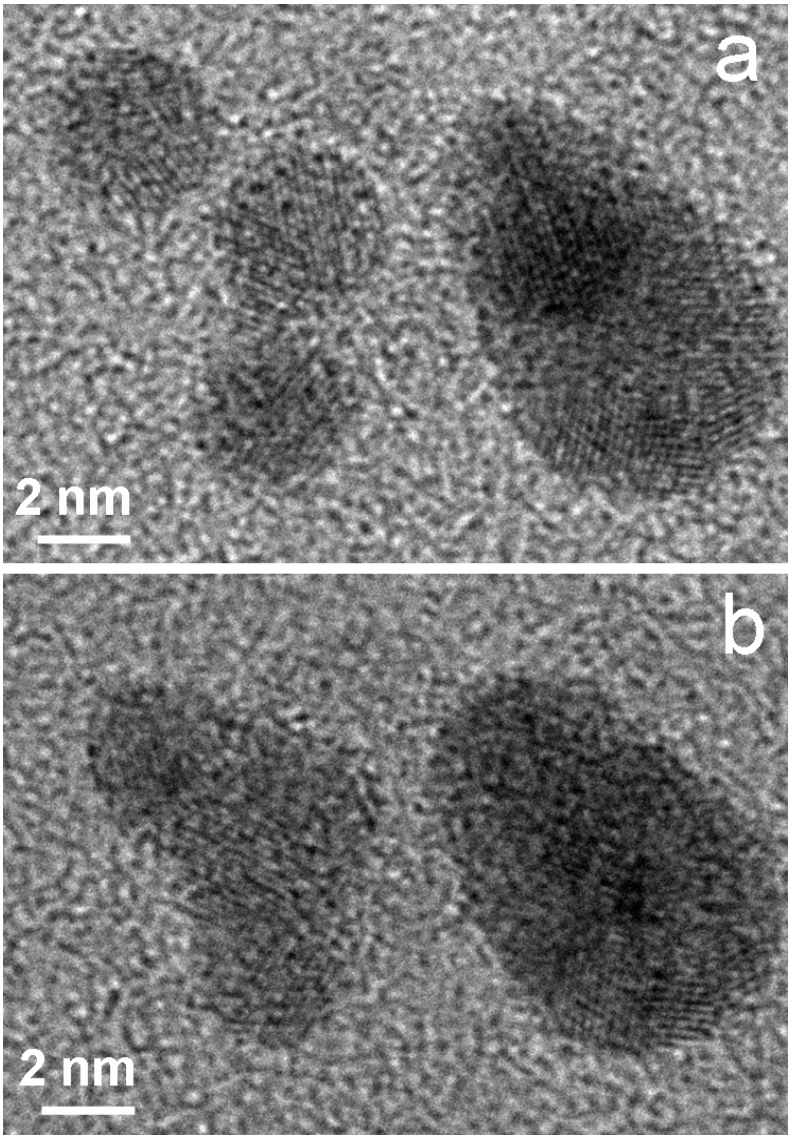

Figure 3-8 a,b: HRTEM images of Fe-Au alloy nanoparticles from Fe^0 precursor before and after 2 min exposure of the specimen with a condensed electron beam. Notice the electron-beam induced fusion of the three nanoparticles located on the left.

The nanoparticles also demonstrate some interesting aggregation under the electron beam during HRTEM studies. Figure 3-8 shows two snapshots of the same area on the sample taken 2 minutes apart. The images indicate that illuminating the particles with highly-converged electron beam, appropriate for HRTEM imaging, initiates the particle fusion by providing sufficient kinetic energy for the particle to migrate towards each other. The energy from the electron beam is not enough though to recrystallize the fused nanoparticles on the timescale of the observation.

The composition of alloy nanoparticles obtained from Fe^0 is analyzed by energy-dispersive X-ray spectroscopy (EDS). The initial molar ratio of precursor molecules in the sample is 1:1. An electron beam, converged to a diameter of few tens of nanometer, is used to illuminate a cluster of the Fe-Au nanoparticles and an EDS signal is collected. A typical EDS spectrum obtained from such measurements is shown in Figure 3-9. The appearance of various prominent peaks of gold and iron confirm the presence of these elements. The presence of oxygen indicates that some of the iron particles are oxidized to iron oxide (and the surface ligands contain oxygen as well). The measured iron-to-gold atomic ratio of 20: 80% is slightly higher than the one obtained from the Vegard's law analysis of the XRD data (14.8±4.7%) but this is only because there is additional iron present in the form iron oxide particles. Therefore, the EDS data are consistent with the data obtained from the Vegard's Law-based estimation.

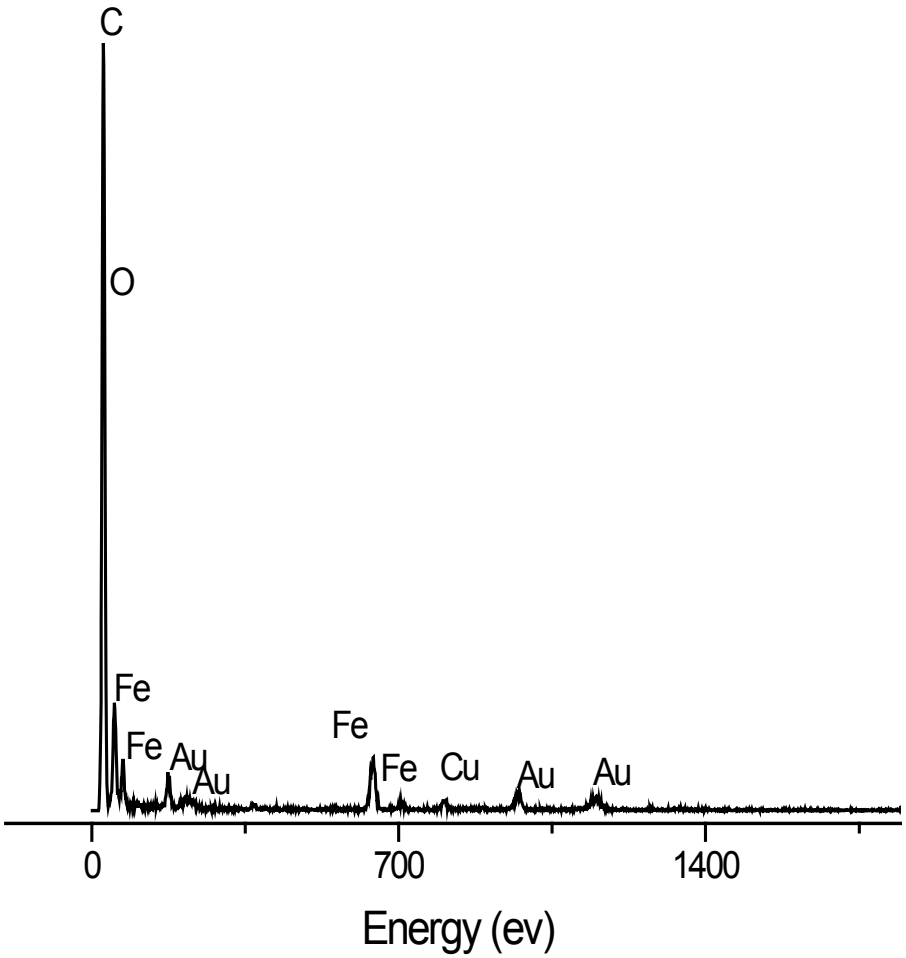

Figure 3-9 Energy dispersive X-ray spectroscopy (EDX) analysis of Fe-Au alloy from Fe^0 precursor.

The particles synthesized by using the two different precursors have different stability. When they are kept dry, both particles can be stored indefinitely (a few months has been tested). The Fe^{2+} synthesized particles are less stable. Once the nanoparticles from Fe^{2+} are dissolved in water, they lose their distinct green color and transform into a rust colored precipitate in approximately 30 minutes. The nanoparticles prepared from Fe^{0} precursor remains stable for a significantly longer period. The lifetime of the particles can be extended if they are kept in the dark. Figure 3-10 represents the UV-visible spectra of gold iron alloy nanoparticles of Fe^{2+} precursor. The spectra are recorded in equal time intervals for 30 minutes. Figure 3-10 shows that the absorption peaks associated with the particles completely disappear after 30 minutes. The disappearance of the plasmon peak may be due to 1) the loss of ligands from the alloy nanoparticles and 2) any unreacted sulphate ions further facilitating the oxidation of iron via redox eqilibria. The width of the peaks (not shown) do not change over time, but rather only decrease in intensity, which suggests that once a particle becomes unstable the oxidation is fairly fast on the time scale of the observation.

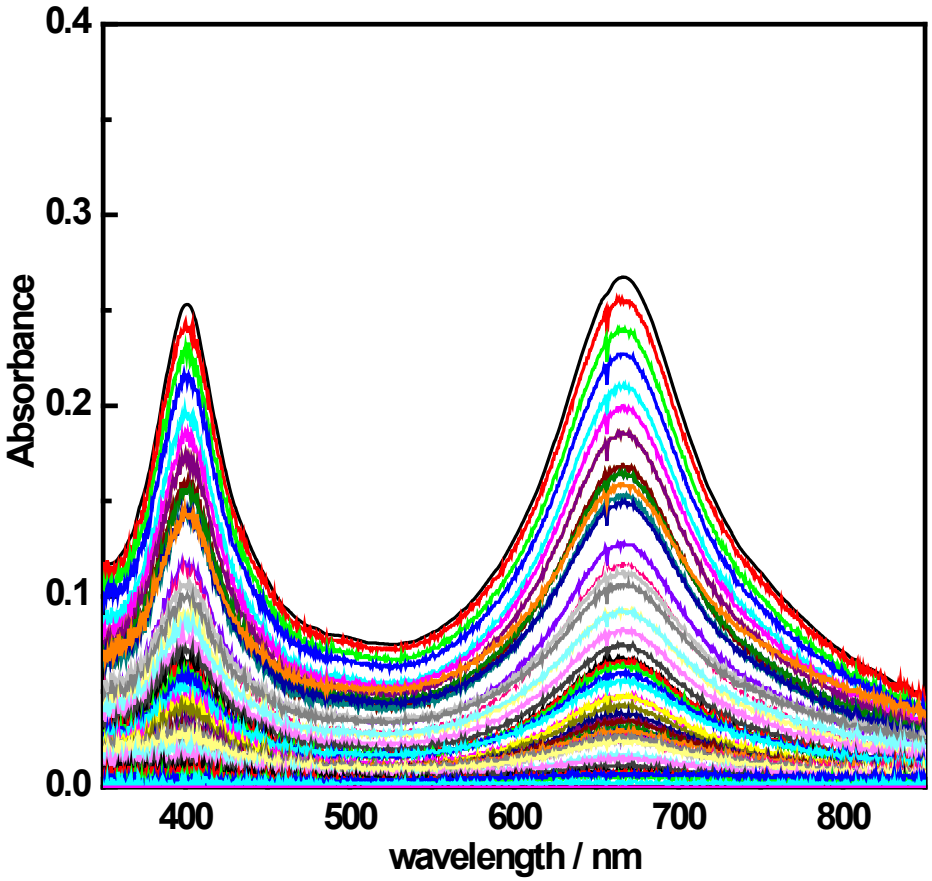

Figure 3-10 The UV-visible absorption spectra (in water) of Fe-Au alloy nanoparticles from Fe^{2+} precursor showing the oxidation trend.

Conclusions:

In summary, a facile synthesis of water-soluble Fe-Au alloy nanoparticles with relative low iron content is demonstrated. The results show that the particle synthesized from iron pentacarbonyl shows higher stability. The absorption of the nanoparticles shows interesting double peak plasma resonance.

References

1. Haruta, M. *Catal. Today* **1997,** 36, (1), 153-166.
2. Haruta, M.; Date, M. *Appl. Catal. a-General* **2001,** 222, (1-2), 427-437.
3. Zhou, B. H., S.; Gabor, A.S *Nanotechnology in Catalysis* Kluwer Academic/Plenum publisher: New York, 2004; Vol. 1.
4. Klabunde, K. J., *Nanoscale Materials in Chemistry*. John wiley &sons, Inc.: 2001.
5. Cushing, B. L.; Kolesnichenko, V. L.; O'Connor, C. J. *Chem. Rev.* **2004,** 104, (9), 3893-3946.
6. Zhou, W. L.; Carpenter, E. E.; Lin, J.; Kumbhar, A.; Sims, J.; O'Connor, C. J. *Eur. Phys. J. D* **2001,** 16, (1-3), 289-292.
7. Ban, Z. H.; Barnakov, Y. A.; Golub, V. O.; O'Connor, C. J. *J. Mater. Chem.* **2005,** 15, (43), 4660-4662.
8. Wang, L. Y.; Luo, J.; Maye, M. M.; Fan, Q.; Qiang, R. D.; Engelhard, M. H.; Wang, C. M.; Lin, Y. H.; Zhong, C. J. *J. Mater. Chem.* **2005,** 15, (18), 1821-1832.
9. Carpenter, E. E.; Kumbhar, A.; Wiemann, J. A.; Srikanth, H.; Wiggins, J.; Zhou, W. L.; O'Connor, C. J. *Mater. Sci. Eng.* **2000,** 286, (1), 81-86.

10. Cho, S. J.; Idrobo, J. C.; Olamit, J.; Liu, K.; Browning, N. D.; Kauzlarich, S. M. *Chem. Mater.* **2005,** 17, (12), 3181-3186.

11. Zhang, L. X.; Sun, X. P.; Song, Y. H.; Jiang, X.; Dong, S. J.; Wang, E. A. *Langmuir* **2006,** 22, (6), 2838-2843.

12. Saha, D. K.; Koga, K.; Takeo, H. *Eur. Phys. J. D* **1999,** 9, (1-4), 539-542.

13. Lu, D. L.; Domen, K.; Tanaka, K. *Langmuir* **2002,** 18, (8), 3226-3232.

14. Chiang, I. C.; Chen, D. H. *Adv. Funct. Mater.* **2007,** 17, (8), 1311-1316.

15. Chang, W. S.; Park, J. W.; Rawat, V.; Sands, T.; Lee, G. U. *Nanotechnology* **2006,** 17, (20), 5131-5135.

16. Terzieff, P.; Gasser, J. G. *J. Phys.Condens. Matter* **1994,** 6, (3), 603-612.

17. Cannella, V.; Mydosh, J. A. *Phys. Rev. B* **1972,** 6, (11), 4220-&.

18. Mock, J. J.; Barbic, M.; Smith, D. R.; Schultz, D. A.; Schultz, S. *J. Chem. Phys.* **2002,** 116, (15), 6755-6759.

19. Gangopadhyay, P.; Gallet, S.; Franz, E.; Persoons, A.; Verbiest, T. *Ieee Transactions on Magnetics* **2005,** 41, (10), 4194-4196.

20. Prodan, E.; Radloff, C.; Halas, N. J.; Nordlander, P. *Science* **2003,** 302, (5644), 419-422.

21. Lin, J.; Zhou, W. L.; Kumbhar, A.; Wiemann, J.; Fang, J. Y.; Carpenter, E. E.; O'Connor, C. J. *J. Solid State Chem.* **2001,** 159, (1), 26-31.

22. Wilcoxon, J. P.; Abrams, B. L. *Chem. Soc. Rev.* **2006,** 35, (11), 1162-1194.

23. Huber, D. L. *Small* **2005,** 1, (5), 482-501.

24. Glavee, G. N.; Klabunde, K. J.; Sorensen, C. M.; Hadjipanayis, G. C. *Inorg. Chem.* **1995,** 34, (1), 28-35.

25. Turkevich, J. G., G.;Stevenson, P.C, *J. colloid Sci.* **1954,** 8, S26-35.

26. Kubaschewski, O. E., H. Z, *Elektrochem. Angew. Phys. Chem.* **1994,** 50, 138-144.

27. Zhou, D.; Usher, B. F. *J. Phys. D-Appl. Phys.* **2001,** 34, (10), 1461-1465.

28. Crangle, J. Scott., W.R. *J. Appl. Phys.* **1965,** 36, 921.

29. Pastor, C. J.; Limones, C.; Hinarejos, J. J.; Garcia, J. M.; Miranda, R.; GomezGoni, J.; Ortega, J. E.; Abruna, H. D. *Surf. Sci.* **1996,** 364, (1), L505-L510.

30. Koga, K.; Sugawara, K. *Surf. Sci.* **2003,** 529, (1-2), 23-35.

CHAPTER 4 - Synthesis of HfO_2 @ Au Core-Shell Nanoparticles

Introduction

The recent progress of research on core-shell nanoparticles is driven by their multiple potential applications and the distinct multifunctional properties associated with core-shell structure. Addition of shell helps to enhance the stability and properties of the core materials. Gold has been the preferred coating material because of its well-known chemistry and chemical functionality.

Recently the semiconductor industries switch to hafnium-based transistors replacing polycrystalline silicon gate electrodes and silicon oxide based insulators, which are the core components of the transistors, the on/off switch of the integrated circuit. Because of reduce dimension, thickness of insulator (SiO_2) between source and drain approach 1 nm and the leakage current approaches an unacceptable rate that produce power drain and over heating for low power devices such as cell phones and laptops.[1-4] To overcome this challenge, a search for high-κ dielectrics materials begin as the industry could no longer shrink the gate dielectric beyond the tunneling limit. In this regard, hafnium based material is considered as the best alternative for the metal- gate electrodes.[4]

HfO_2@Au core-shell nanoparticle is synthesized as it can be a potential material for hafnium based metal gate electrodes. Both core HfO_2 and shell Au have high value of dielectric constant (≈ 25 and 6.9) compare to conventional silicon dioxide (3.9).[2, 5] Without addition of Au shell HfO_2 suffers from high leakage current after high temperature annealing (≥ 500 ^oC) due to the onset of crystallization.[3] This crystallization can be suppressed by addition of gold shell. Gold is noble metal with high work function that ensures the better charge retention and can be used in nanocrystalline based nonvolatile floating gate memory.[1, 2, 6] They can also be used as

heat resistant, highly reflective, protective optical coating, and in catalysis.[5] To the best of our knowledge, there is no report in the literature for the synthesis of HfO_2@Au core-shell nanoparticles despite their attractive applications. In this letter a solution based high temperature reduction method is described to make the HfO_2@Au nanoparticles.

Experimental section

HfO_2@Au core-shell nanoparticles are synthesized by using high temperature reduction method.[7] Briefly, in the first step HfO_2 seed solution is prepared. In the second step, the particles are coated with gold shell. Both steps are carried out under inert atmosphere of argon. In a typical synthesis, a solution containing HfO_2 is prepared from 0.2 mL tetrakis dimethylaminohafnium (98%), 20 mL of dioctylether (99%), 1.5 mL of oleic acid (99%), and 1.5 mL of oleylamine, (70%), 2.5g of 1,2-hexadecanediol (90%). The solution is refluxed at 270 ^{o}C for 1.3 hours. In the next step, 0.52 g of gold (III) acetate (99.9%), 2.5g, of 1,2-hexadecanediol, 1.5 mL oleic acid, 2.5 mL of oleylamine and 25 mL of dioctylether is added to 10 mL solution of the HfO_2 nanoparticles. The solution is heated (at 15 ^{o}C/min) and refluxed at 250 ^{o}C for 2 hours. Following this step, the solution is cooled to room temperature and treated with ethanol (99%) to precipitate the nanoparticles. The nanoparticle slur is centrifuged at 8500 rpm for an hour. The dark purple precipitate containing the nanoparticles is deposited at the bottom of centrifuge tube. After washing the precipitate with ethanol several times, the nanoparticles are vacuum dried at room temperature for 10 hours. Afterwards, the nanoparticle is redispersed in hexane in the presence of 1.5 mL oleic acid and 1.5 mL oleyl amine. Size selective precipitation is carried out by centrifuging and redissolving the nanoparticle in hexane or toluene.

Results and discussion

Measurements of the surface plasmon resonance band of the nanoparticles provide an indirect piece of evidence supporting the formation of HfO_2@Au core-shell nanoparticles. Figure 1 shows the UV-Visible absorption spectra of HfO_2@Au core-shell (square curve), gold (diamond curve), and HfO_2 seed nanoparticles (circle curve). The plasmon peak maximum of gold nanoparticles is at 530 nm and that of HfO_2@Au core-shell nanoparticles is at 555 nm. As expected the plasmon peak of the HfO_2@Au core-shell nanoparticles show 25 nm red shift compare to gold nanoparticles prepared under identical conditions. There is no observation of plasmon peak of HfO_2 seeds nanoparticles in the visible region of the spectrum as represented in Figure 1. The surface plasmon resonance properties of core-shell nanoparticles depends upon the thickness of the shell, size, shape, and dielectric constant of immediate vicinity of the nanoparticles.[8-10] The red shift of the surface plasmon peak is due to a collective interaction of the electrons of the interconnected particles.[11-25] In this particular experiment there is not much shift in plasmon peak of HfO_2@Au core-shell nanoparticles despite the high dielectric constant of core material indicating that it's likely to have thick shell of gold. However, this is consistent with the calculation initially presented in the introduction section (Fig 1.3b). But it is unlikely to have a significant amount of pure gold nanoparticles in these core-shell nanoparticles samples (see later TEM and XRD results) due to the lack of broadening of the surface plasmon peak.

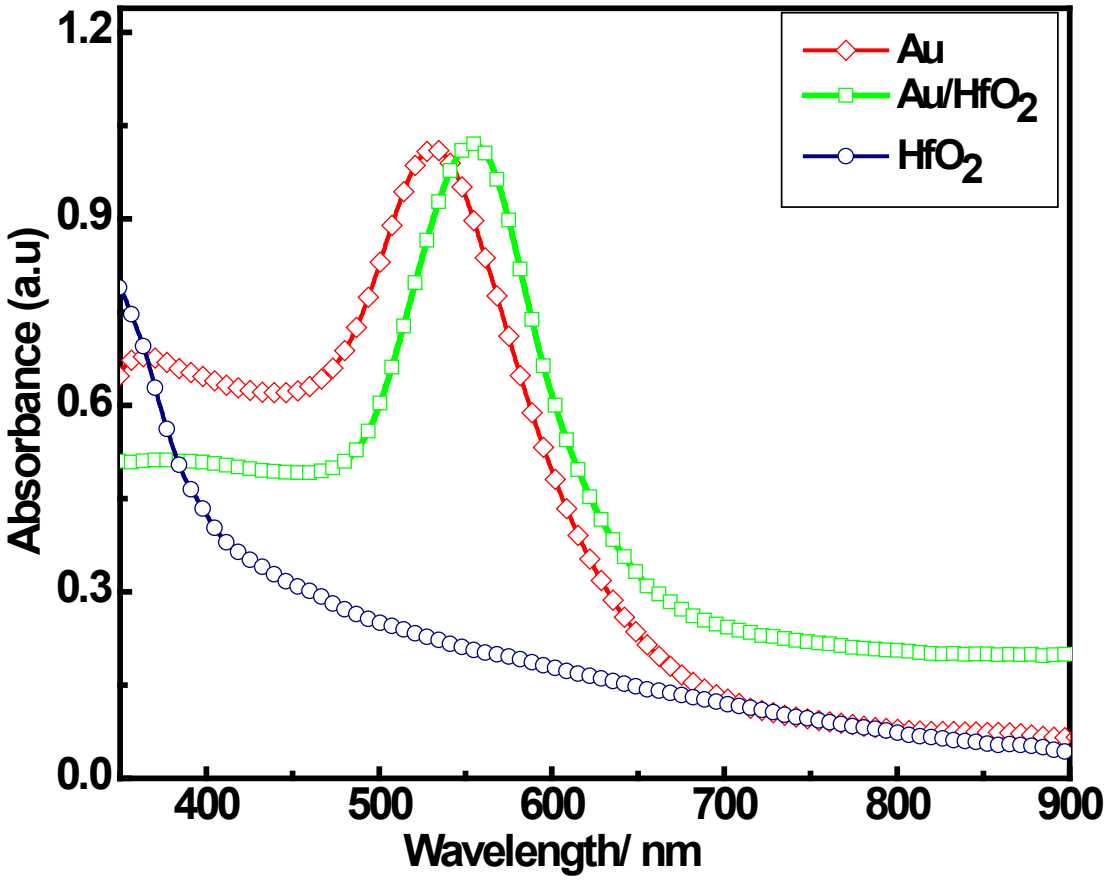

Figure 4-1 UV-Visible absorption spectra of pure gold nanoparticles (diamond curve), hfO_2@Au core-shell nanoparticles (square curve), and hafnium oxide nanoparticles (circle curve).

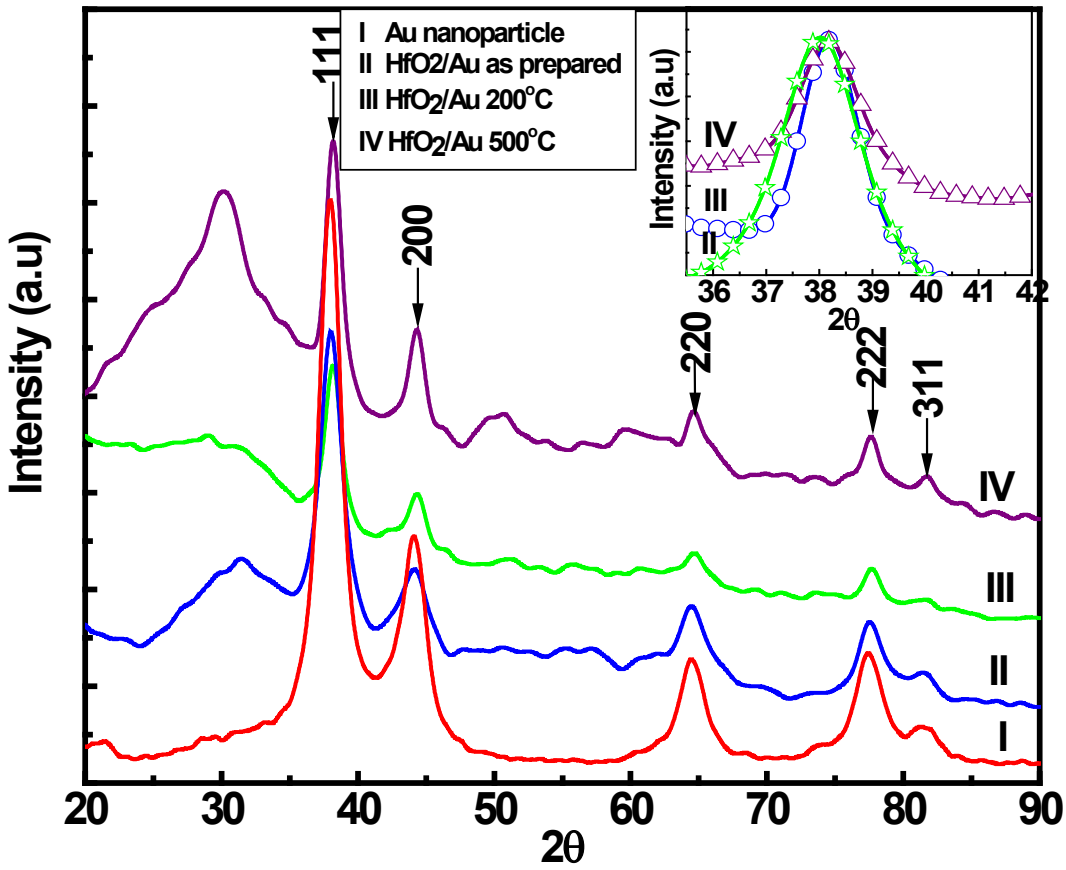

Figure 4-2 Powder XRD pattern of pure gold nanoparticles (I), XRD pattern of as prepared hafnium oxide-gold core-shell nanoparticles (II), & XRD patterns of hafnium oxide-gold core shell annealed to 200 and 500°C (III) & (IV). Inset shows the shifting of (111) peak to higher 2θ while annealing.

Figure 4-2 shows the XRD patterns of pure gold nanoparticles (curve I) as prepared HfO_2@Au core-shell nanoparticles (curve ii) and HfO_2@Au core-shell samples anneal at 200 and 500^oC (curve iii and iv). The XRD pattern of the core-shell nanoparticles reveals that the samples are crystalline and homogeneous. The 2θ angles at 37.94^o, 44.02^o, 64.50, 77.78^o and 81.56^o in Figure 4-2 curve (iii) correspond to (111), (200), (220), (311) and (222) fcc atomic reflections planes of core-shell nanoparticles. The XRD peaks of HfO_2@Au core-shell nanoparticles are located at similar 2θ angles and the x-ray intensities are comparable to pure gold nanoparticles, in agreement with the gold shell of the nanoparticles. Therefore, the observation of well-develop fcc gold XRD pattern in HfO_2@Au core-shell nanoparticles confirms the presence of highly crystalline gold shell. It is unlikely that x-ray diffraction is inconclusive for structure and chemical composition determination of both core and shell[26] because the shell obstructs observation of diffraction peaks corresponds to hafnium oxide. Therefore, an annealing experiment is carried out to establish the actual mechanism of core and shell formation. The inset of Figure 2 shows the change in 2θ angle of (111) atomic reflections of core-shell nanoparticles at 25^{o}C (star curve) and after annealing at 200 and 500^{o}C (circle and triangle curve). Considerable change in 2θ angle (higher 2θ angle) is observed (from 37.94^o to 38.24^{o}2θ for (111) atomic reflection) when the sample is annealed to 200^{o}C. Interestingly, no change in XRD peaks position is observed when the annealing temperature is increased from 200 to 500^{o}C. The observation indicates that the hafnia and gold of the nanoparticles alloy with each other when annealed above 200^{o}C. The shifting of each peak position to higher 2θ values in the alloy sample indicates softening of the lattice constant. At this moment, it is speculated that this is due to incorporation of gold into the hafnium oxide surface. The calculated average lattice constant for the alloy and pure gold nanoparticles for their cubic unit cell are 4.004 ± 0.025 Å and 4.064 ±

0.025 Å respectively. The lattice constant of gold nanoparticles is very close to that of bulk gold.[27] The XRD data shows that there is no phase segregation of the elements in the core-shell nanoparticles below 200 ^{o}C. At higher temperature (500 ^{o}C) the nanoparticles begin to show the phase segregation as proven by appearance of (111) peak of cubic hafnium oxide as shown in Figure 4-2 (curve iv).

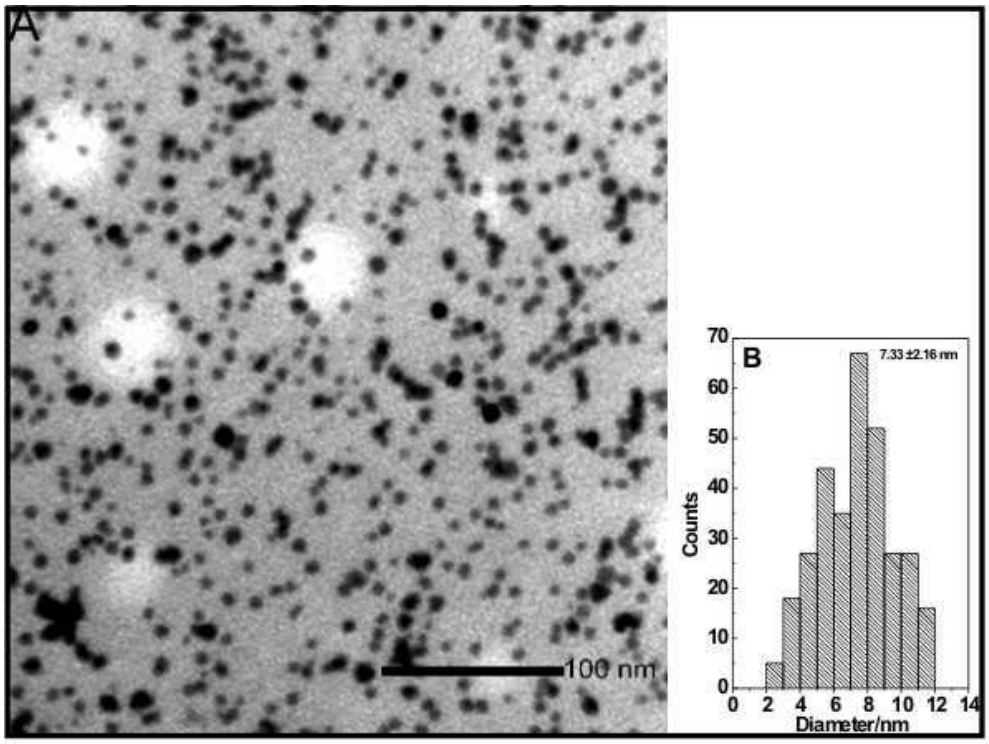

Figure 4-3 TEM image of hafnium oxide-gold core-shell nanoparticles (A), Histogram shows the corresponding size distribution (B).

Figure 4-3a shows the low resolution transmission electron microscope (TEM) image of HfO_2@Au core-shell nanoparticles. The average sizes of the nanoparticles are 7.3 ± 2.1 nm as shown by the histogram Figure 4-3b. Within the resolution of the TEM; the particles are multifaceted with irregular shape and mostly in the spherical form. Based on the feature contrast

in the TEM images in terms of darkness and brightness, it is thought that there is a fraction of uncoated HfO_2 nanoparticles are present in the product. By counting particles in the TEM images, the fraction of uncoated particles is estimated to be ~ 15 %. The majority (~ 85 %) of HfO_2 nanoparticles are coated with gold shell. Nanoparticles size is tuned by using size selective precipitation as explained in the experimental section.

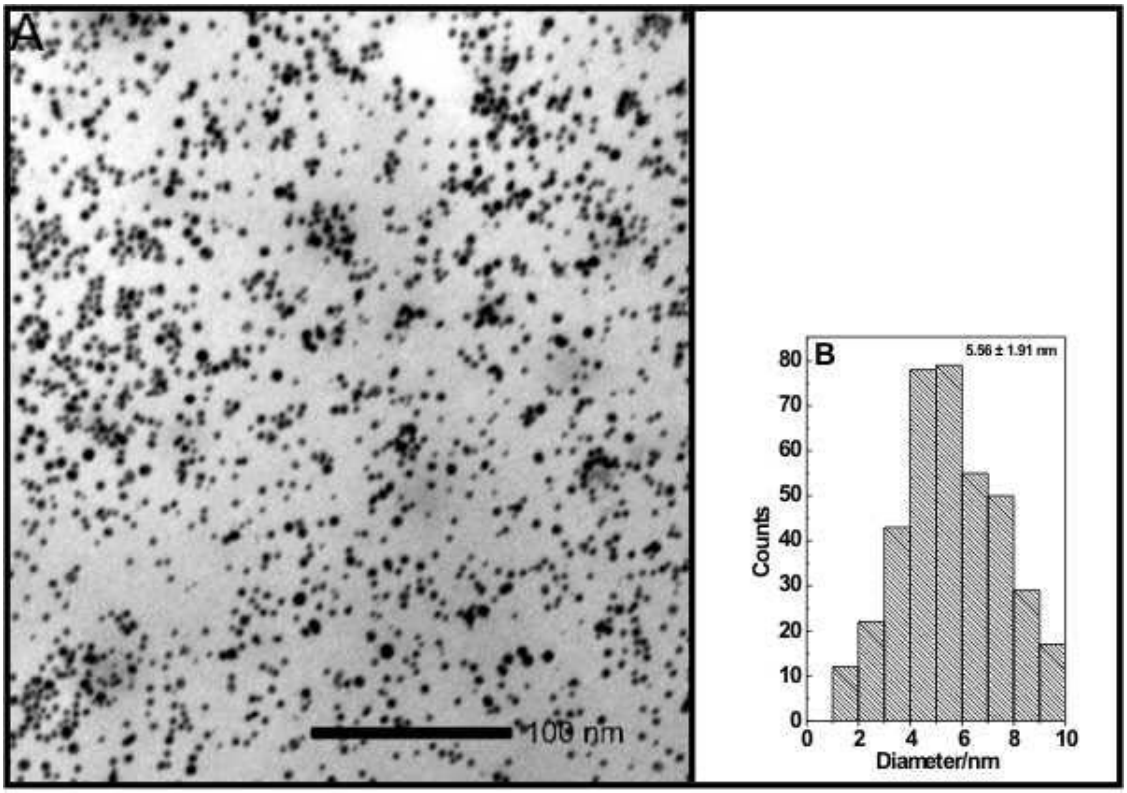

Figure 4-4 TEM image of hafnium oxide-gold core-shell nanoparticles after repetitive washing and centrifuging (A), Histogram shows the corresponding size distribution (B).

Figure 4-4a represents the smaller size of HfO_2@Au core-shell nanoparticles that are obtained by centrifuging the same batch of nanoparticles at 8500 rpm for an hour and

redissolving in hexane. The average size of the nanoparticles is 5.5 ± 1.9 nm as represented by the histogram Figure 4-4b. As expected, the particles are more aggregated and spherical due to centrifuging.

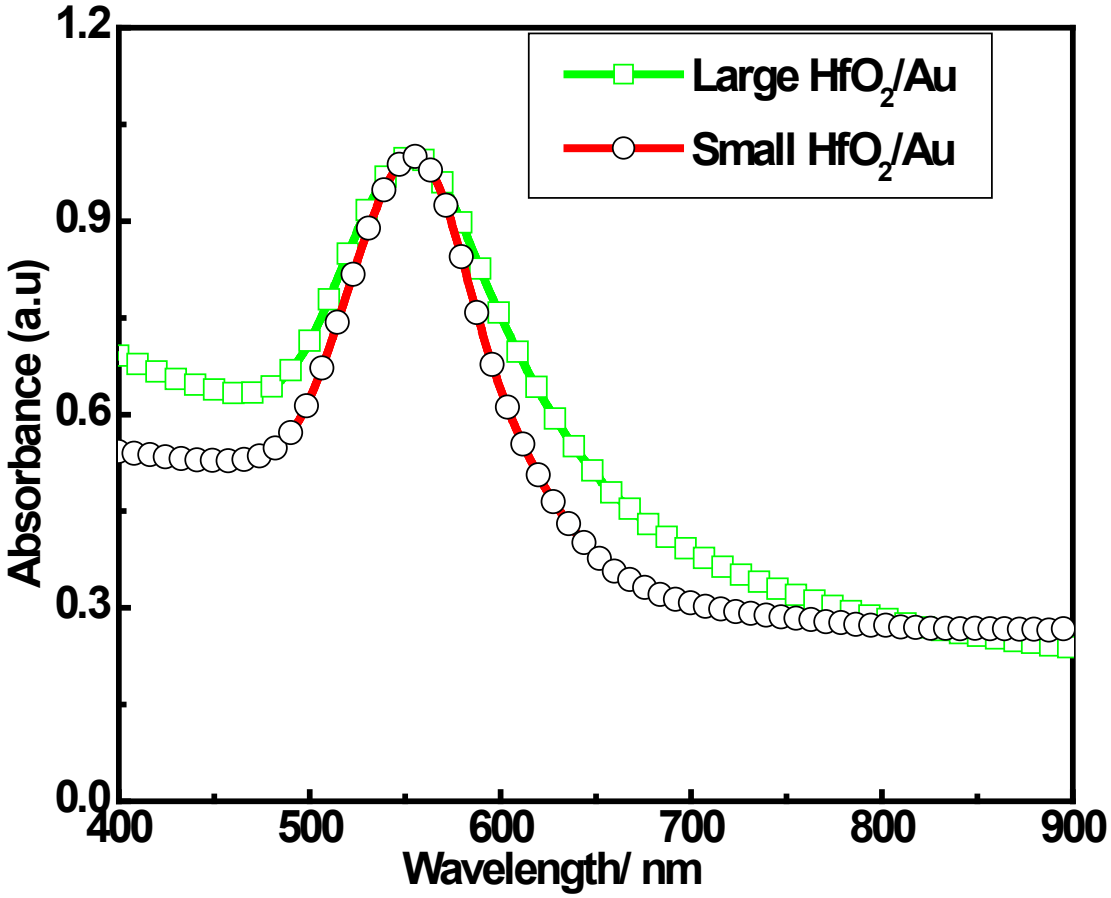

Figure 4-5 Shows the UV-visible absorption spectra of two different sizes of hafnium oxide core-gold shell nanoparticles.

Figure 4-5 shows the UV-visible absorption spectrum for large and small nanoparticles. The small nanoparticles are obtained after size selective precipitation as explained in Figure 4-4a. The bandwidth of large HfO_2@Au nanoparticles is higher compare to small nanoparticles.The full width half maximum of the large and small nanoparticles is differ by 2.1 nm; which is very similar to the particle size measurement from the TEM images within the measurement error. Therefore, there is no shift in surface plasmon bands, but narrowing down the surface plasmon band for the smaller nanoparticles. The result provides an indirect piece of evidence for the size tuning ability from the single batch synthesis of nanoparticles.

The structure of the HfO_2@Au core-shell nanoparticles is further studied by high resolution transmission electron microscope (HRTEM) and electron diffraction (Figure 4-6). The inset I and II show the HRTEM images of HfO_2@Au core-shell nanoparticles. The samples are prepared in two different formvar support grids after size selective precipitation. Multidomain structure with a regular lattice interplanar distance (0.24 nm), corresponds to fcc Au (111) is observed in both images. The particle size is very similar to that of low resolution TEM measurement as in Figure 3c and shell thickness of the nanoparticles calculated from the HRTEM analysis is 1.05 nm. The observation of several diffraction rings is attributed to the crystalline structure of the core-shell nanoparticles (Figure 4-6). The diffraction rings are corresponds to the (111), (200), (220), (222), and (311) atomic reflection planes originate from the gold shell. The result is consistent with the powder XRD shown in Figure 4-2.

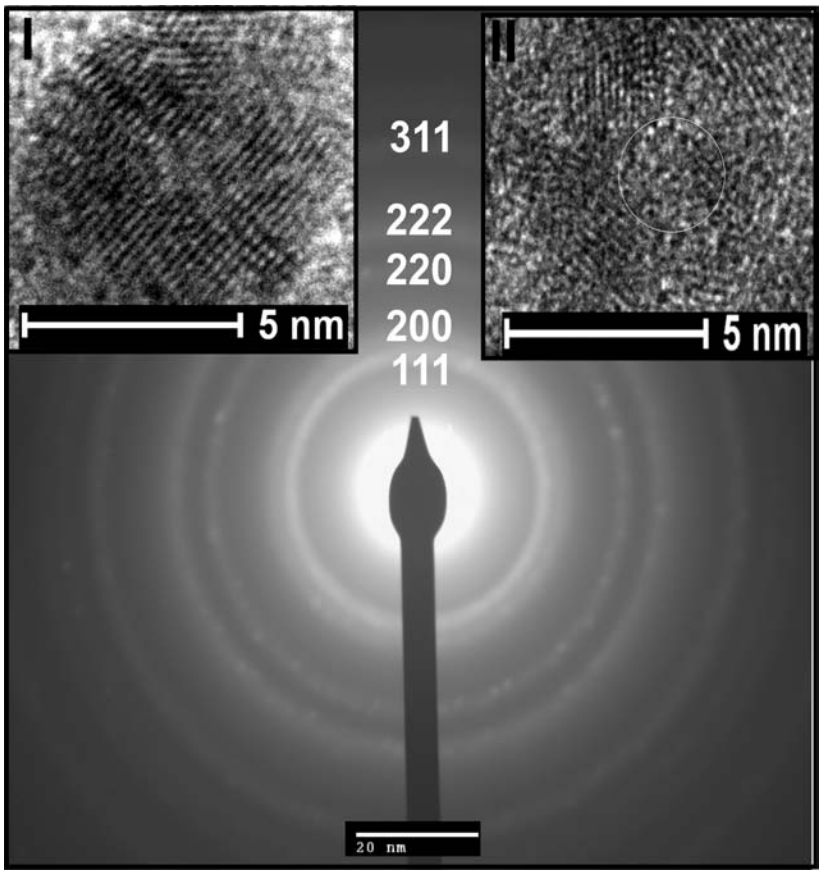

Figure 4-6 is electron diffraction of hafnium oxide- gold core-shell nanoparticles displaying a high degree of crystallinity of the nanoparticles. Insets show the HRTEM images of core-shell structure of hafnium oxide gold core-shell nanoparticles.

Figure 4-7 shows a spectrum obtain from energy dispersive X-ray analysis (EDX). The spectrum clearly shows the presence of both hafnium and gold in the nanoparticles. The atomic ratio of gold to hafnium from EDX analysis is found to be 81:19.

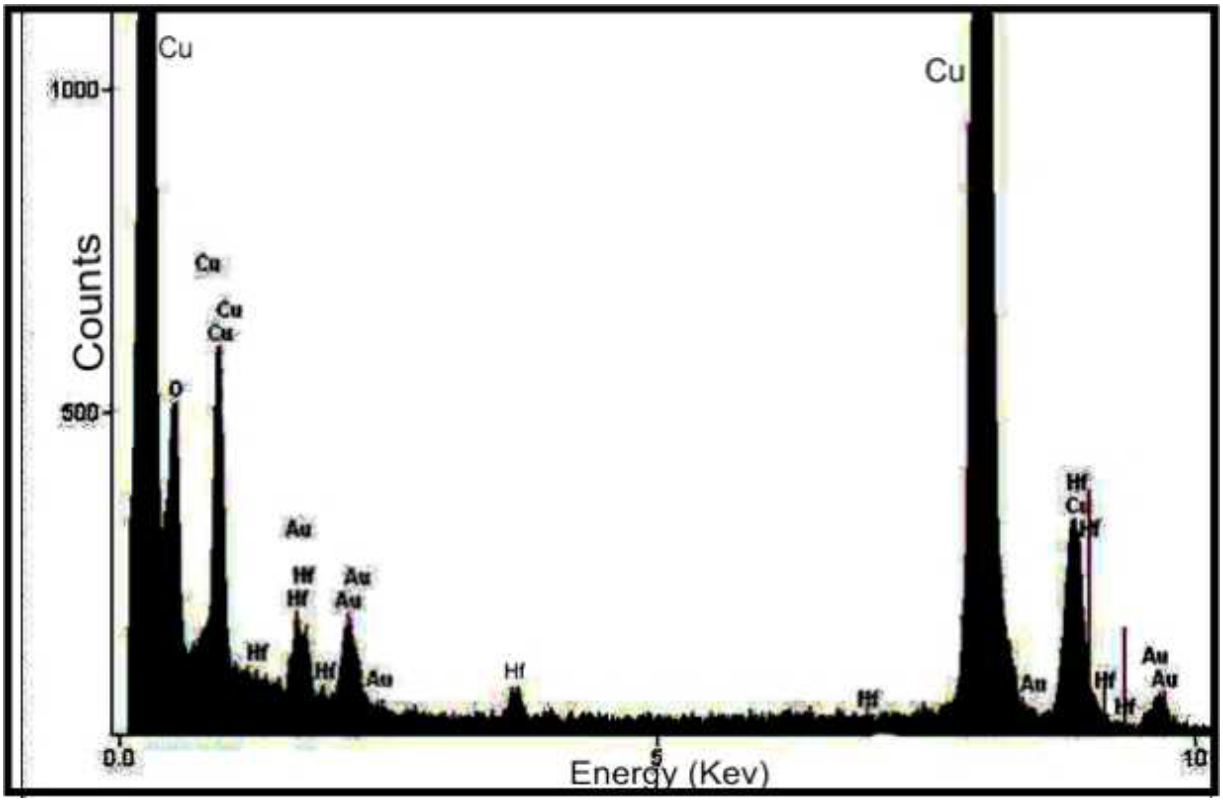

Figure 4-7 Shows an energy dispersive x-ray analysis spectrum of hafnium oxide- gold core-shell nanoparticles.

To estimate average thickness of the shell for the HfO_2@Au core-shell nanoparticles, a comparison of thickness measurement between TEM and EDX determine Au: Hf ratio is performed. The comparison is based on the spherical core-shell model and the metallic composition, i.e.

$$N_{Hf}\, x \text{ Atomic ratio (AR) of Au: Hf} = N_{Au} \quad (1)$$

This relation can be expanded as,

$$\frac{\pi}{6} d_c^3 \rho_c / M_c x AR(Au)/(Hf) = \frac{\pi}{6}[(d_c + 2d_s)^3 - d_c^3]\rho_s / M_s \quad (2)$$

$$d_s = \frac{1}{2}[d_c^3 \rho_c / M_c x \frac{M_s}{\rho_s} x AR(Au)/(Hf) + d_c^3]^{1/3} - d_c$$

$$d_s = \frac{1}{2}\sqrt[3]{43.06 x AR(Au)/(Hf) + 91.73} - 4.51 \quad (3)$$

where, d_c and d_s stand for the diameter of the core HfO_2 (4.51 nm) and the thickness of the Au shell; ρ_c and ρ_s are the density of core and shell which is equal to 9.68 g cm^{-3} and 19.3 g/ cm^3 , and M_c and M_s are the Molar mass and atomic mass of core material (HfO_2) and shell (Au) respectively. The thickness of the Au shell determine from the above example using equation (3) is 0.66 nm. Therefore, it is notable that the thickness calculated from the EDX analysis of the core-shell nanoparticles is within 33 % accuracy to the thickness determines from the TEM measurement that is 1.05 nm.

Conclusions

HfO_2@Au core-shell nanoparticles are successfully prepared by using high temperature reduction method. The growth of such structure is based on the random nucleation of gold on the surface of hafnium oxide. The HfO_2@Au core-shell nanoparticles are potential candidate for hafnium-based transistors, flash memory, and catalysis.

References

1. Zhu, X. H.; Zhu, J. M.; Li, A. D.; Liu, Z. G.; Ming, N. B., J.*Mater. Sci.Technol.* **2009,** 25, (3), 289-313.
2. Jung Yup, Y.; Ju Hyung, K.; Won Joon, C.; Young Ho, D.; Chae Ok, K.; Jin Pyo, H.,. *J.Appl. Phys.* **2006,** 100, (6), 066102.
3. Chen-Chan, W.; Jyun-Yi, W.; Yan-Kai, C.; Che-Hao, C.; Tai-Bor, W., *Appl. Phys. Lett.* **2007,** 91, (20), 202110.
4. Matthews, J., *Physics Today* 2008,February.
5. Tang, H.; Yang, X. B.; Kirkham, J.; Smith, D. A., *Anal. Chem.* **2007,** 79, 3646.
6. Groeseneken, G.; Aoulaiche, M.; De Gendt, S.; Degraeve, R.; Houssa, M.; Kauerauf, T.; Pantisano, L. Advanced Semiconductor Devices and Microsystems, 2006. ASDAM '06. International Conference on, 2006; pp 15-19.
7. He, X.; Liu, H.; Li, Y.; Wang, S.; Li, Y.; Wang, N.; Xiao, J.; Xu, X.; Zhu, D., *Adv. Mater.* **2005,** 17, 2811.
8. Moores, A.; Goettmann, F., *New J. Chem.* **2006,** 30, (8), 1121-1132.
9. Wang, L. Y.; Luo, J.; Maye, M. M.; Fan, Q.; Qiang, R. D.; Engelhard, M. H.; Wang, C. M.; Lin, Y. H.; Zhong, C. J *J. Mater. Chem.* **2005,** 15, (18), 1821-1832.
10. Miller, M. M.; Lazarides, A. A., J. *Phys.Chem. B* **2005,** 109, (46), 21556-21565.
11. Radloff, C.; Halas, N. J., *Nano Lett.* **2004,** 4, (7), 1323-1327.
12. Chowdhury, M. H.; Campbell, C. J.; Theofanidou, E.; Lee, S. J.; Baldwin, A.; Sing, G.; Yeh, A. T.; Crain, J.; Ghazal, P.; Cote, G. L., *Proc. SPIE* **2006,** 6099, 609905.
13. Ekgasit, S.; Thammacharoen, C.; Yu, F.; Knoll, W., *Appl. Spectrosc.* **2005,** 25, 661.

14. Fu, E.; Ramsey, S. A.; Chen, J.; Chinowsky, T. M.; Wiley, B.; Xia, Y.; Yager, P., *Sens. Actuators B* **2007,** B123, 606.

15. Haes, A. J.; Chang, L.; Klein, W. L.; Van Duyne, R. P., *J. Am. Chem. Soc.* **2005,** 127, 2264.

16. Herderick, E. D.; Tresback, J. S.; Vasiliev, A. L.; Padture, N. P., *Nanotechnology* **2007,** 18, 1.

17. Larsson, E. M.; Alegret, J.; Kaell, M.; Sutherland, D. S., *Nano Lett.* **2007,** 7, 1256.

18. Maillard, M.; Giorgio, S.; Pileni, M. P., *J. Phys. Chem. B* **2003,** 107, 2466.

19. Mie, G., *Ann. Phys.* **1908,** 25, 377.

20. Pileni, M. P., *Nat. Mater.* **2003,** 2, 145.

21. Schatz, G. C.; Young, M. A.; Van Duyne, R. P., *Top. Appl. Phys.* **2006,** 103, 19.

22. Shalaev, V. M., *Nat. Photonics* **2007,** 1, 41.

23. Storhoff, J. J.; Marla, S. S.; Bao, P.; Hagenow, S.; Mehta, H.; Lucas, A.; Garimella, V.; Patno, T.; Buckingham, W.; Cork, W.; Muller, U. R., *Biosens. Bioelectron.* **2004,** 19, 875.

24. Underwood, S.; Mulvaney, P., *Langmuir* **1994,** 10, 3427.

25. Volkov, V. S.; Bozhevolnyi, S. I.; Devaux, E.; Laluet, J. Y.; Ebbesen, T. W., *Nano Lett.* **2007,** 7, 880.

26. Zhang, J.; Post, M.; Veres, T.; Jakubek, Z. J.; Guan, J.; Wang, D.; Normandin, F.; Deslandes, Y.; Simard, B., *J. Phys. Chem. B* **2006,** 110, (14), 7122-7128.

27. Dahal, N.; Chikan, V.; Jasinski, J.; Leppert, V. J., *Chem. Mater.* **2008,** 20, (20), 6389-6395.

CHAPTER 5 - Phase Controlled Synthesis of Iron Silicide Nanoparticles (Fe_3Si and $FeSi_2$) in solution

Introduction

As robust, stable, environmentally green, and inexpensive material,[1, 2] iron silicides could take a critical role in the next generation of nanomaterials with a wide range of potential applications.[3] The bulk phase diagram of iron and silicon shows at least five known iron silicide compounds (Fe_3Si, Fe_5Si_3, FeSi, β-$FeSi_2$, and α-$FeSi_2$).[4] According to the phase diagram, ε -FeSi, β-$FeSi_2$, and Fe_3Si are stable at room temperature while, Fe_2Si, α-$FeSi_2$ and Fe_5Si_3 are metastable. These iron silicides exhibit metallic, semiconductor or insulating behavior depending on their structure. Ferromagnetic properties are observed in iron rich phases Fe_3Si, and Fe_5Si_3.[5-8] FeSi acts as a Kondo insulators with increasing conductivity as a function of temeparture,[9, 10] β-$FeSi_2$ is a narrow band gap (0.85 eV) semiconductor and potential photovoltaic material.[11, 12] α-$FeSi_2$ is a metal and a potentially beneficial interface for silicon based solar cells.[13] Fe_3Si is a good candidate as a ferromagnetic electrode in spintronics devices such as magnetic tunnel junctions.[7, 14] The use of conventional ferromagnetic materials such as Fe or Co, suffers from oxidation and impedance mismatch between the ferromagnetic film and semiconductor. Fe_3Si has been proposed as an excellent alternative for those conventional materials.[15] Fe_3Si has high Curie temperature of ~ 800 K, is oxidation resistant, and has a similar spin polarization to that of Fe and Co (45% in thin film), and a relatively high value of saturation magnetization (84 to 196 emu/g).[6, 14, 16] At room temperature Fe_3Si crystallizes in the $D0_3$ crystal structure. The crystal structure is derived based on space group Fm3m and cubic unit cell dimension of magnitude 5.665 Å.

Despite the interesting properties and potential applications, iron silicide is challenging to produce in a solution. While gas phase synthetic methods are described in the literature, no colloidal synthetic methods exist to produce such nanoparticles. There are some examples of self-assembled epitaxial thin films of Fe_3Si on Si, Ge, and GaAs substrates.[8, 16-22] However, these examples are difficult to implement for many of the intended applications. The preparation of heuslar Fe_3Si nanoparticles by magnetron sputtering is also described in the literature.[8] There are recent reports of the synthesis of either FeSi nanowires from a single source precursor molecule [9] or the preparation of Fe_5Si_3 nanowire and nanoparticles.[5, 23]

The synthesis of nanoparticles from bulk iron silicide is challenging due to complex phase behavior and multiple stoichiometries of the material. Typically, iron silicides are produced at very high temperatures that are difficult to implement in solution. The stoichiometric composition of silicide can not be explained by a simple sets of rules based on oxidation state and electronegativity.[1] A key question is what phase of iron silicide would be produced if chemical reactions were carried out with or without stoichiometric control. This letter shows that it is possible to form highly crystalline iron silicide nanoparticles in solution with some phase and size control. In this particular method, iron pentacarbonyl and silicon tetrachloride are used as precursor molecules to produce iron silicide. From these precursor molecules, Fe_3Si or β-$FeSi_2$ is formed at relatively low temperatures.

Experimental Details

Iron pentacarbonyl $Fe(CO)_5$, 99.5%, and silicon tetrachloride ($SiCl_4$) 99.99% are purchased from Strem chemicals. 1,2-hexadecanediol techn. 90%, oleic acid 90%, triphenylphophine 90%, ethanol 95%, 1,2-dichlorobenzene 99%, and octyl ether 99% are purchased from Aldrich. All the chemicals are used as received without further purification.

Synthesis of Fe_3Si nanoparticles

Fe_3Si nanoparticles 4-7 nm in size are synthesized in a three-neck-flask. In a typical synthesis 20 ml ortho 1,2-dichlorobenene or octyl ether is mixed with 4 mmol (1.03 g) of 1,2-hexadecanediol and heated to ~ 220 to 250 ^oC. When ortho 1,2-dichlorobenzene is used as solvent the mixture is heated to 180^oC. The Solution is stirred for 10 minutes under argon atmosphere. Following the dissolution of 1,2-hexadecanediol 2 mmol (0.56 g) of oleic acid and 2 mmol (0.52 g) of triphenylphosphine are injected in the solution stepwise. In order to inject triphenylphosphine, it is dissolved in 2 ml of either octyl ether or 1,2-dichlorobenzene and oleic is injected as received because it is liquid at room temperature. At this point of the synthesis, 20 mmol (3.91 g) of iron pentacarbonyl is injected and the decomposition of iron pentacarbonyl results in the formation of iron nanoparticles. Immediately, the initial yellow solution changes to black as nanoparticles form. Within 10 seconds of iron pentacarbonyl injection, 6.6 mmol (1.12 g) of silicon tetrachloride is injected into the solution that leads to the formation of iron silicide nanoparticles. A vigorous reaction takes place forming dense fumes inside the condenser (extreme care should be taken while handling iron pentacarbonyl and 1,2-dichlorobenzene as both are toxic and inflammable). The solution is refluxed under argon for 10 to 240 minutes. After injection of the silicon tetrachloride, the appearance of the solution changes from dense black to light black. When the stoichiometric ratio of silicon and iron is changed to 2:1 mostly β-$FeSi_2$ nanoparticles

are formed. Interestingly, the iron mono silicide never forms under the experimental conditions, even when the ratio is changed to 1:1, but the reaction rather leads to the formation of Fe_3Si phase. The Fe_3Si nanoparticles synthesize in 1,2-dichlorobenzene are readily soluble in heptane or hexane. The solution is cooled to room temperature after refluxing 3 hours, and 95% ethanol is added in excess and centrifuged for 10 minutes at 8500 rpm. The black brown precipitate is separated from the very light brown supernatant. The precipitate is dried and characterized by XRD. For further characterization, the precipitate is redissolved in hexane, followed by ultrasonic treatment for an hour in the presence of 0.8 mmol of oleic acid and 0.8 mmol of triphenylphosphine. The additions of ligands in this part of experiment help to increase the solubility of the nanoparticles. The solution is treated with excess ethanol (50 ml) to precipitate nanoparticles. The sample is centrifuged again at 8500 rpm for 10 minutes. Finally, the precipitate obtained is dissolved in hexane or heptane. This final solution is used to prepare samples for further characterizations.

Results and discussion

Figure 5-1 shows powder x-ray diffraction (XRD) patterns of the Fe_3Si nanoparticles under different experimental conditions along with the calculated Fe_3Si x-ray diffraction peaks. The powder x-ray diffraction pattern reveals that the samples are homogeneous and crystalline. The XRD peaks at 27.30, 31.48, 45.30, 54.11, 56.28, 66.10, 75.14, and 83.76 2θ correspond to (111), (200), (220), (311), (222), (400), (420), and (422) lattice planes of $D0_3$ structure Fe_3Si nanoparticles. When iron rich conditions are used, experiments are carried out for 10 minutes to 240 minutes refluxing time to assess the effect of refluxing time on the crystallinity and homogeneity of the samples. As Figure 1a clearly shows, the crystallinity and homogeneity of the samples are increased with longer refluxing times. Fe_3Si Nanoparticles that are obtained from

refluxing longer time (240 minutes) visually show sharp peaks. However, when the peaks are fitted with Debye-Scherrer formula[24] to extract approximate particle size, the data confirmed that the crystallite sizes remain the same (~ 8.5 ± 1.8 nm) as shown in table 1. The most intense (200) peak is Gaussian fitted to data in each experiment and determine the width and the peak values as well as errors in these values from the Gaussian function. The result indicates that once the growth of the nanoparticles is taken place, monomer exchange among the particles is minimal.

Interestingly, a small change in 2θ angles is observed in XRD patterns between the calculated (Figure 1a (V)) and the experimental results of the Fe_3Si nanoparticles. The small change in 2θ angles is attributed to the formation of thin sublayer of iron silicide (Fe_3Si) or silicon oxide that produce different residual strain on the nanoparticles. Similar behavior is reported in case of anatase (TiO_2), silver, and iron platinum nanoparticles.[25-27]

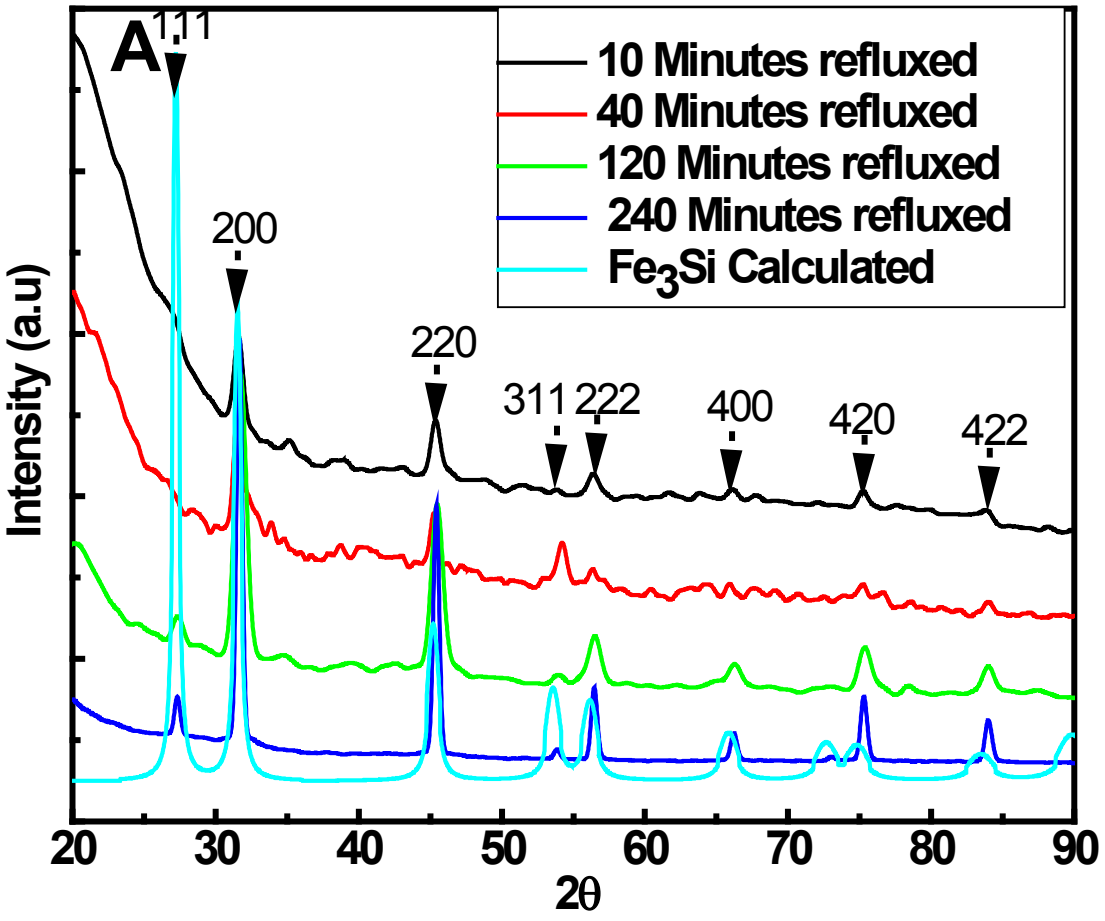

Figure 5-1 XRD patterns of Fe_3Si nanoparticles prepared under different refluxing time: 10 minutes (I), 40 minutes (II), 120 minutes (III), 240 minutes (IV), and calculated XRD patterns based on space group no. 225 and lattice constant 5.665 Å.

Stability and the robustness of the Fe_3Si nanoparticles are evaluated by annealing the nanoparticles at 500°C to 900°C in air. For comparison the calculated XRD patterns of α-$Fesi_2$ and β-$FeSi_2$ are also presented in Figure 5-2 (I) & (II) respectively. While annealing the nanoparticles below 450°C, no change in the XRD pattern is observed (not shown in figure). However, when the nanoparticles are heated in air above 450°C, phase change takes place in the material as shown in Figure 1b (III-V). When the nanoparticles are heated (above 600°C); the major peaks of Fe_3Si phase partially collapse as depicted in Figure 1b (V). Further heating the nanoparticles to 700°C results in the formation of the mixed phase of α-$FeSi_2$, β-$FeSi_2$ and Fe_5Si_3 (IV).[12, 28, 29] When the nanoparticles are heated to 900°C, they exhibit the same phase as in 700°C, but sharpening and narrowing of the XRD peaks is observed due to annealing (III). This is different from the bulk phase diagram of iron and silicon where Fe_5Si_3 is the expected product to be obtained upon annealing in the iron rich samples.

When the XRD patterns of annealed sample at 900°C is compared with calculated XRD patterns of Fe_5Si_3 and α-$FeSi_2$, the later appears more prominent along with β-$FeSi_2$ as shown in Figure 5-3. The XRD peaks at 2θ degree 28.04 and 33.40 are the peak associated with Fe_5Si_3. The Fe_5Si_3 has hexagonal structure with lattice constant a = 6.759Å and c = 4.720Å and space group of P63/mcm.[40] During annealing, the absence of silicon dioxide peaks or iron oxide peaks (which are prone to form even at lower temperature) indicate that there is no phase segregation of the elements within the nanoparticles.

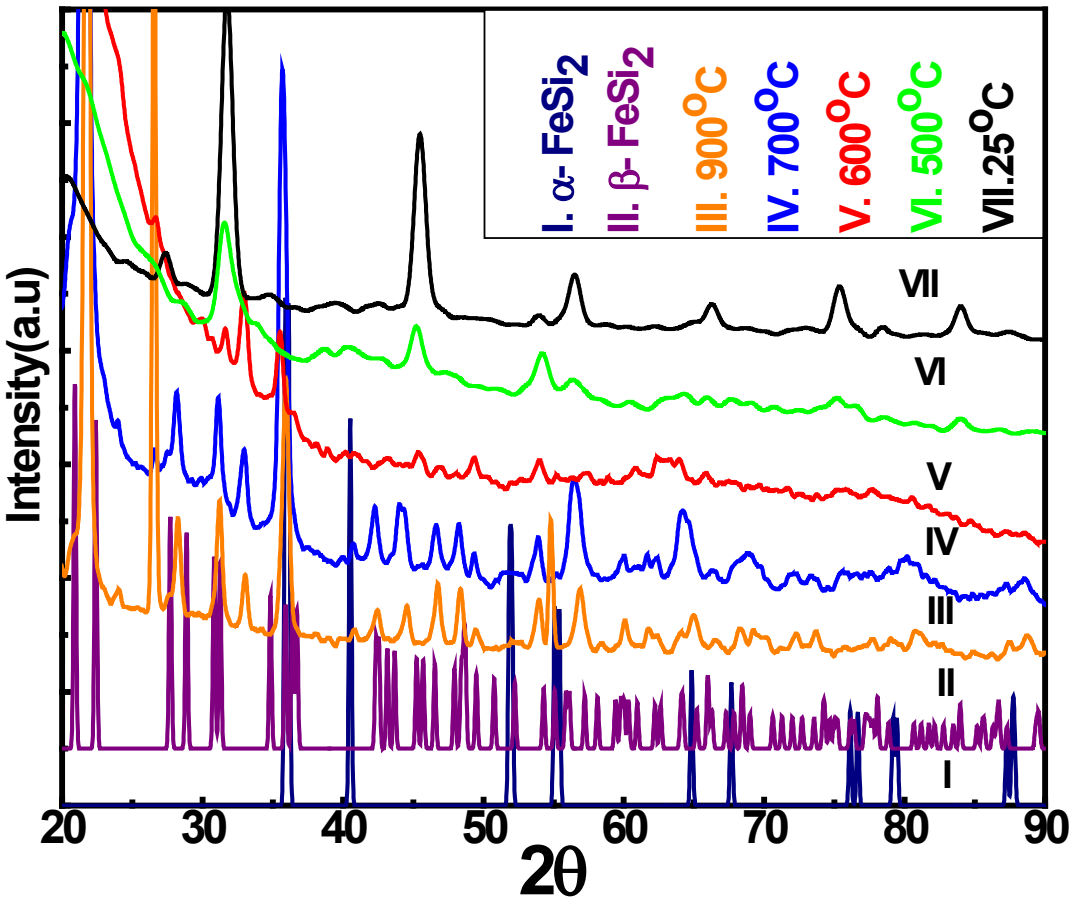

Figure 5-2 represents calculated XRD patterns of α-$FeSi_2$ and β-$FeSi_2$ (I) & (II). XRD patterns of Fe_3Si nanoparticles annealed at different temperatures: 900°C (III), 700°C (IV), 600°C (V), 500°C (VI), and room temperature (VII).

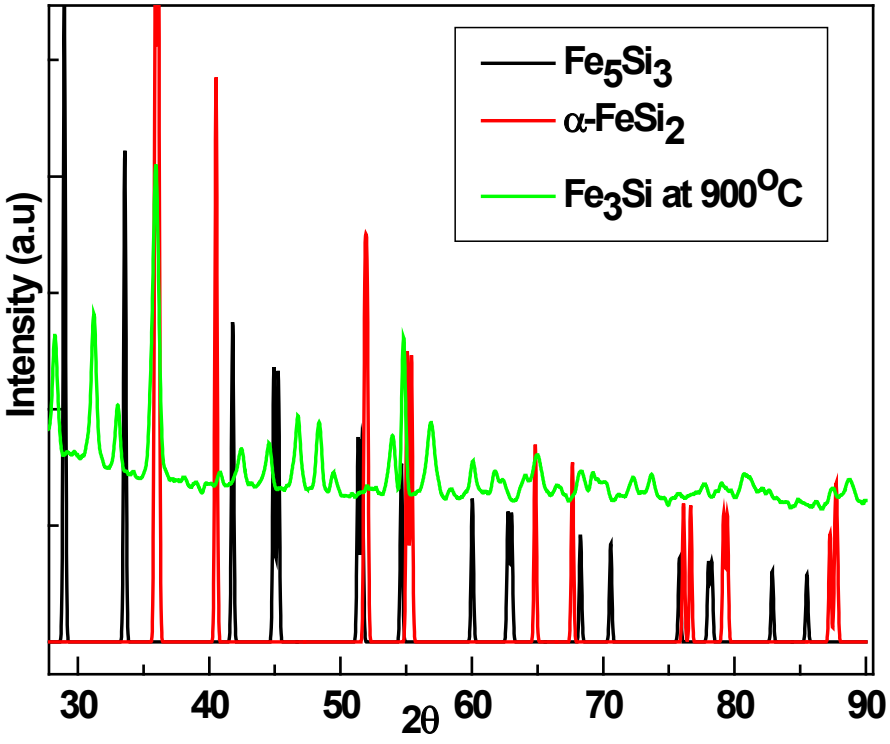

Figure 5-3 the calculated XRD patterns of bulk α –$FeSi_2$ and $Fe_5Si_3$and the XRD of Fe_3Si nanoparticles annealed at 900°C.

Unusually, Fe_3Si nanoparticles are not formed in all concentrations of precursor molecules. As shown in Figure 1c, several experiments are carried out at different concentrations of iron to silicon precursor molecules, keeping all variables in the reactions constant. When the concentration of iron to silicon precursors is 0.24 M and 0.08 M, the reaction simply forms an amorphous material with broad atomic reflections at 30, and 40 degree 2θ as shown in Figure 1c (IV). Further increasing the concentration of iron to silicon precursor molecules from 0.46 M and

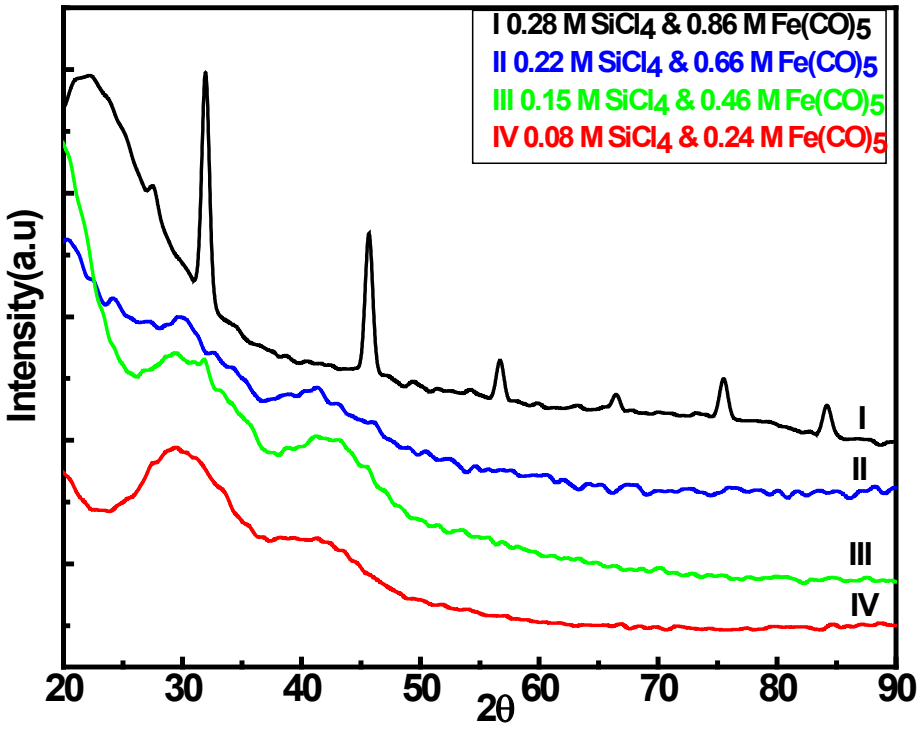

Figure 5-4 XRD patterns of Fe_3Si nanoparticles at different molar concentration but fixed molar ratio (3:1) of iron to silicon precursor: 0.86 M iron to 0.28 M silicon precursor (I), 0.66 M iron to 0.22 M silicon precursor (II), 0.46 M iron to 0.15 M silicon precursor (III), and 0.24 M iron to 0.08 M silicon precursor (IV).

0.15 M (this composition is later called the small Fe_3Si nanoparticles in this manuscript) to 0.66 M to 0.22 M, the x-ray diffraction patterns do not show significant improvement in the crystallinity and homogeneity of the nanoparticles (Figure 1c III and II). The poor crystallinity and homogeneity in all concentrations except 0.86 M of iron precursor to 0.28 M of silicon precursor is probably due to very small cluster size and absence of favorable nucleation sites for formation of the nanoparticles. Crystalline Fe_3Si nanoparticles are formed in all experiments containing the iron to silicon precursors concentrations above or equal to 0.86 M to 0.28M as

shown in Figure 1c (I) (nanoparticles for this composition are considered as large Fe_3Si nanoparticles in this manuscript). The effect of different reducing agents is also addressed in the synthesis of the Fe_3Si nanoparticles. In this particular experiment 1,2-hexadecanediol is found to be the best reducer to produce crystalline iron silicide nanoparticles. Other reducers such as lithium-aluminium hydride, lithium triethylborohydride, and ethylene glycol simply cause the formation of amorphous material.

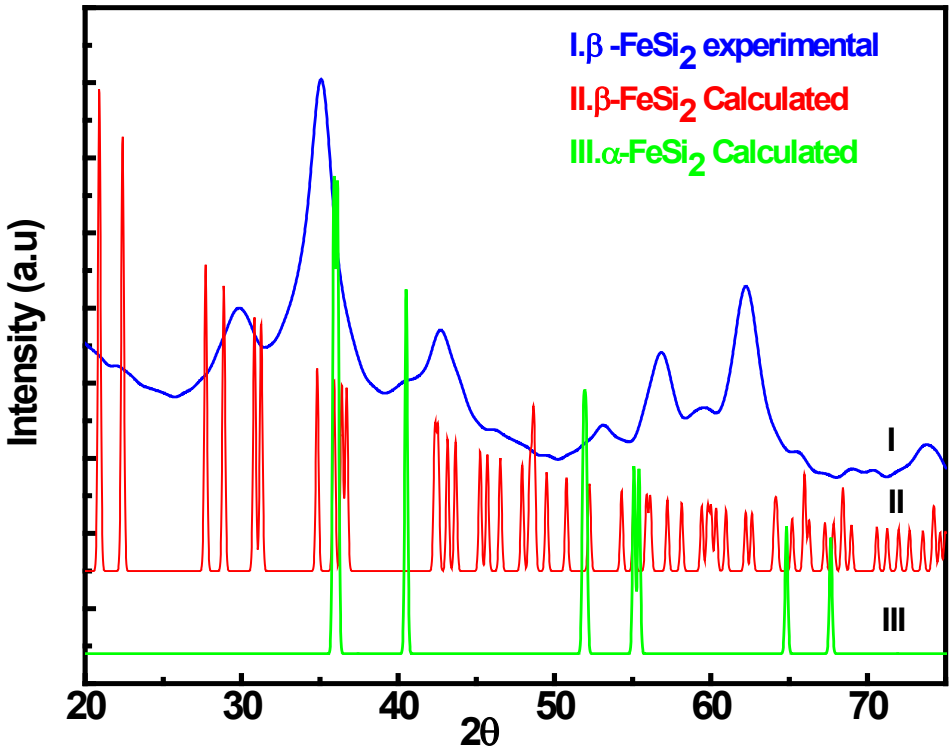

Figure 5-5 XRD patterns of β-$FeSi_2$ nanoparticles prepared from 1:2 molar ratios of iron to silicon precursor molecules (I), and calculated XRD patterns of β-$FeSi_2$ and α-$FeSi_2$ **based on their crystal geometries, lattice constants, and space groups (II).**

When the mole ratio of precursor molecules is 1:2 for iron to silicon, mainly β-$FeSi_2$ is formed (Figure 1d (I)).[30-32] Figure 1d (II) and (III) represents the calculated XRD patterns of β-$FeSi_2$ and α-$FeSi_2$ nanoparticles based on their orthorhombic and tetragonal crystal structures, lattice parameters and crystallographic space groups. The close agreement of the experimental and calculated XRD pattern suggests the formation of β-$FeSi_2$ nanoparticles.

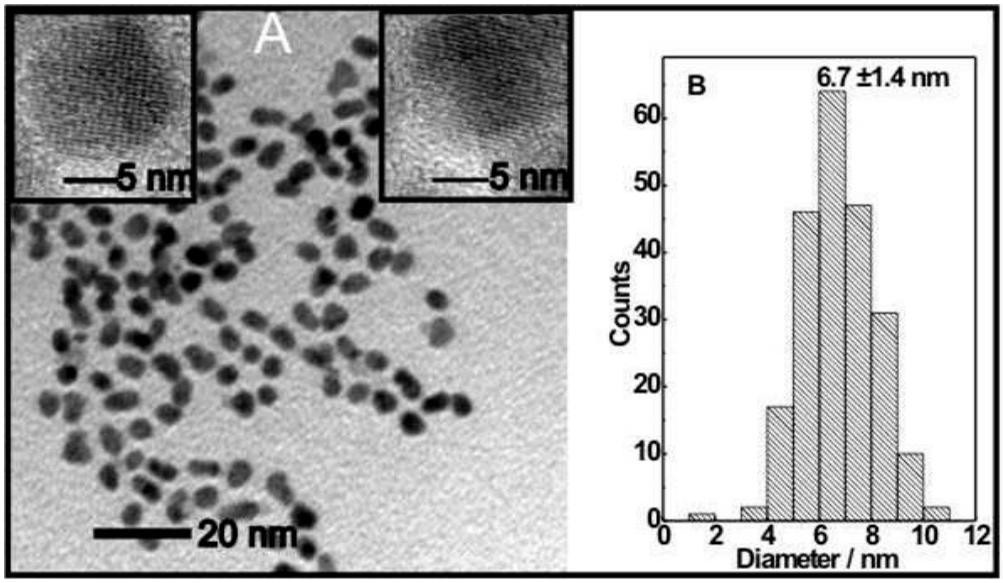

Figure 5-6 represents TEM image of large Fe_3Si nanoparticles. Insets: HRTEM images of Fe_3Si nanoparticles representing d (111) lattice fringes.

Figure 5-6a shows the low magnification transmission electron microscope (TEM) image of the large Fe_3Si nanoparticles. The particles are prepared by taking 0.86 M iron pentacarbonyl and 0.28 M silicon tetrachloride that corresponds to the XRD patterns (I) in Figure 1c. Figure5-6b shows the size histogram of the corresponding Fe_3Si nanoparticles.The average size of the nanoparticles is 6.7 nm with standard deviation of ± 1.4 nm. The particle distribution shows some degree of polydispersity revealing the inhomogeneous nucleation of silicon and iron

nanoparticles (note: silicon precursor is injected in the second step). Within the resolution of the low resolution TEM, the image reveals irregularly shaped, multifaceted nanocrystals with sharp edges. Figure 5-6a insets show the high resolution transmission electron microscope (HRTEM) images of large Fe_3Si nanoparticles and the material is highly crystalline with clearly seen lattice fringes. Insets show the d (111) lattice fringes of $D0_3$ cubic structure with lattice spacing 0.32 nm. The experimental results of the lattice spacing from HRTEM are similar to that of d (111) lattice spacing obtained from XRD (Figure 5-6a) and confirms the crystalline nature, and formation of Fe_3Si nanoparticles. The calculated d (111) spacing for the bulk Fe_3Si is 0.32 ± 0.01 nm.

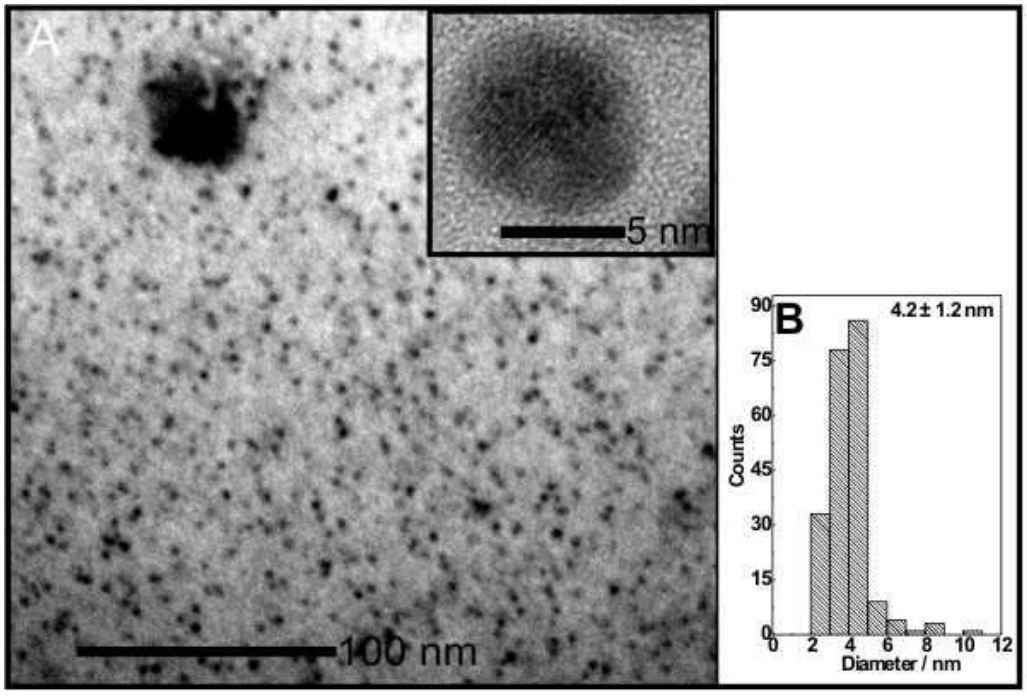

Figure 5-7 TEM image of small Fe_3Si nanoparticles (A). (B) **Size histogram of small Fe_3Si nanoparticles.**

The size control growth of the nanoparticles is crucial to produce well defined iron silicide nanoparticles; here the size of the nanoparticles depends on the ratios of the precursor molecules. Changing the concentration of reacting precursor molecules at fixed molar ratios of 3:1 for iron to silicon produces the Fe_3Si nanoparticles of different sizes. Figure5-7a represents the small Fe_3Si nanoparticles prepared by using 0.15 M of silicon tetrachloride and 0.46 M of iron pentacarbonyl. The nanoparticles in this case are nearly monodisperse with average size of 4.2 nm and standard deviation of ± 1.2 nm (Figure 5-7b). The inset shows the HRTEM of the same nanoparticles, revealing that nanoparticles are amorphous in this particular composition. This result is consistent with the XRD results shown in Figure 5-4 (III).

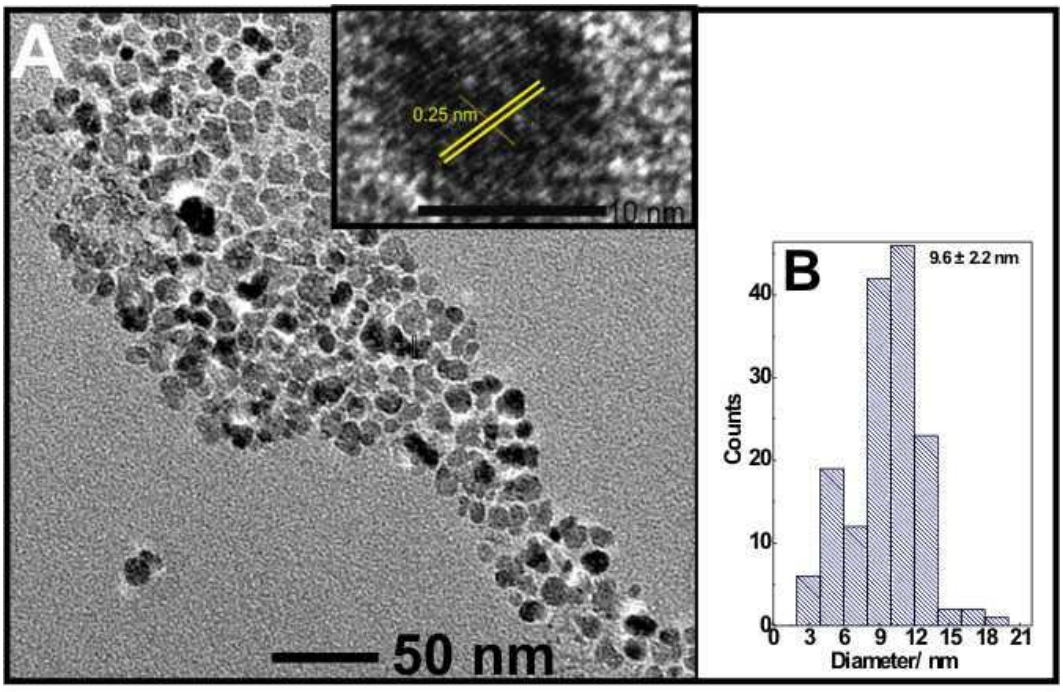

Figure 5-8 TEM image of different phase (β-$FeSi_2$) nanoparticles (A). Insets: HRTEM images of β-$FeSi_2$ nanoparticles representing d (222) lattice fringes (B) **Corresponding size histogram of the β-$FeSi_2$ nanoparticles.**

When the precursors molar ratio for iron to silicon are changed to 1:2 the reaction forms the β-$FeSi_2$ nanoparticles previously shown in Figure 5-5 (I). The average size and morphology of the particles is represented by the TEM image as shown in Figure5-8a. The TEM image shows that the β-$FeSi_2$ nanoparticles are not spherical and larger than Fe_3Si nanoparticles. The sudden change in size and morphology is probably due to deposition selectivity of precursor molecules during the growth of nanoparticles. Figure 5-8b shows the histogram of the corresponding β-$FeSi_2$ nanoparticles and the average size is 9.6 nm with standard deviation of 2.2 nm. The inset shows the HRTEM image of β-$FeSi_2$ nanoparticles where the lattice fringes are clearly seen. The value of lattice spacing measure from HRTEM is 0.24 nm corresponds to d (222) lattice. The calculated bulk value of d (222) lattice of β-$FeSi_2$ is 0.24 nm ± 0.01 nm. The result implies that particles are growing continuously without phase segregation of the elements and are single crystalline. Further characterization of the nanoparticles is performed by using electron diffraction associated with HRTEM. The diffraction spots are obtained by focusing the electrons beam on single particle and the spots are simulated by using ratiometric and vector addition method.[33] For the spots identification zone axis is considered parallel to the $(1\bar{1}0)$ direction. All the distinct and identifiable points (Figure 5-9) are attributed to the crystallinity of the particles and correspond to the different lattice planes of the $D0_3$ type large Fe_3Si nanoparticles. Absence of diffraction rings confirm that the nanoparticles are neither randomly oriented like grains in polycrystalline foils nor like spheroidal particles in films. The nanoparticles are not forming the super lattice as there is no evidence of super lattice diffraction spots.[34]

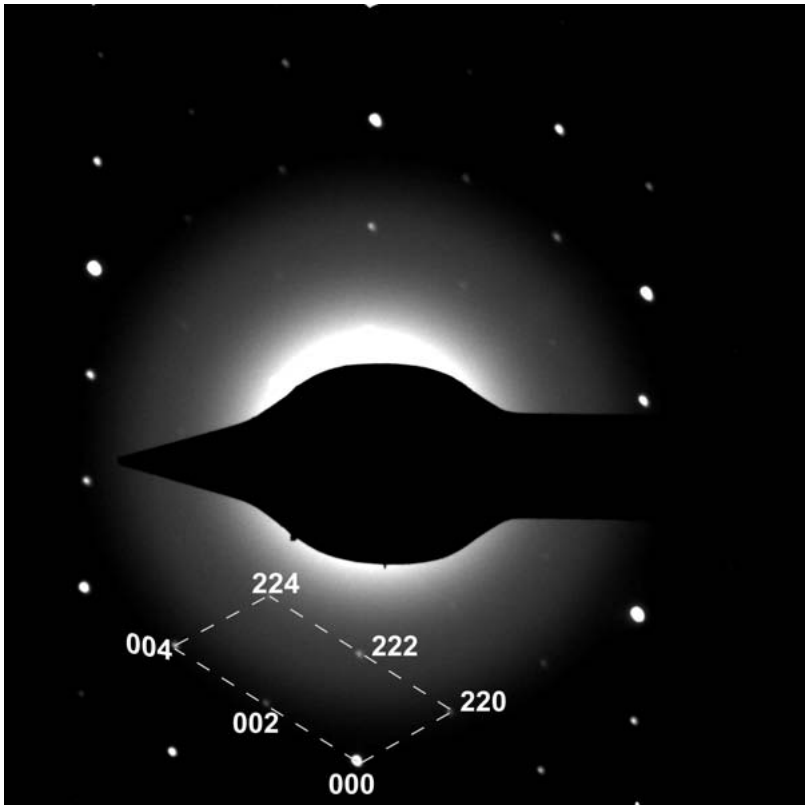

Figure 5-9 Electron diffraction patterns of the large Fe_3Si nanoparticles.The zone axis is parallel to $(1\bar{1}0)$ direction.

Iron silicide nanoparticles are relatively hard materials that allow size distribution determination by atomic force microscopy (AFM) from the topography of the as deposited nanoparticles on flat surfaces such as Si <111>. The flatness of the Si <111> surface measured from tapping mode AFM is 0.2 nm. In AFM particles size is defined by the maximum height of the particles and gives the three dimensional projection of the nanoparticles. The deposited Fe_3Si nanoparticles on Si <111> are analyzed by tapping mode AFM. Banin and co-workers pointed out that nanoparticle height could be underestimated by AFM in free air because the recorded

height is the sum of the topography and the force gradient contribution.[35] Therefore, to increase the visibility of the particles during analysis (not shown), the AFM images of nanoparticles on Si <111> are enhanced by the taking the negative eigenvalues of the Hessian function of the image. The image enhancement step is followed by the selection of a 15 nm diameter circular region encompassing the visually enhanced particles. The difference between the median of the lowest 3 pixels and highest three pixels are taken as the height of the particles. This process ensures that artifacts associated with the AFM technique (such as spikes) are minimized. The histograms of the particles are generated by adding up several hundreds of particles.

The tapping mode AFM image of large Fe_3Si nanoparticles are shown in Figure 5-10a and corresponding average particles height is 6.9 ±1.5 nm is represented by the histogram in Figure 5-10b. Figure 5-10c is AFM image for the small Fe_3Si nanoparticles and corresponding average height distribution is 3.8 ±1.0 nm as shown by the histogram in Figure 5-10d. Similarly, Figure 5-10e shows the AFM image of β-$FeSi_2$ nanoparticles with average height distribution of 9.1 ± 3.5 nm (Figure 5-10f). The summary of the TEM, AFM, and XRD measurements are shown in table 3

Table 3 Size measurements of Fe_3Si and β-$FeSi_2$ nanoparticles from TEM, AFM, & XRD

S.N	Samples	TEM		AFM	
		Diameter/ nm	Standard deviation	Height/ nm	Standard deviation
1	Large Fe_3Si	6.7	± 1.4	6.9	± 1.5
2	Small Fe_3Si	4.2	± 1.2	3.8	± 1.0
3	β-$FeSi_2$	9.6	± 2.2	9.1	± 3.5

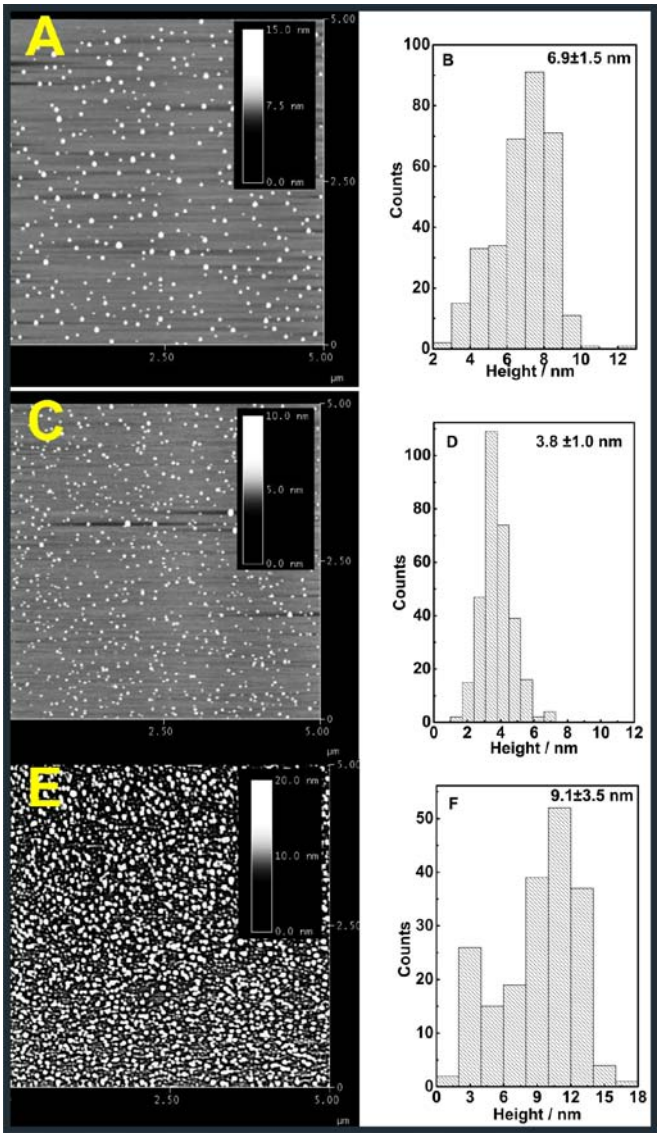

Figure 5-10 Tapping mode AFM images of large Fe_3Si (A), small Fe_3Si (C), and β-$FeSi_2$ (E) nanoparticles. (B), (D), and (F) are their corresponding height histograms.

From the table 3 it is concluded that the height measurement of the nanoparticles by using AFM is agreed well with the TEM particle size measurement. As expected, the morphology and shape of the nanoparticles are similar in both AFM and TEM images.

Composition of the nanoparticles is examined by using Energy Dispersive X-ray analysis (EDX). EDX point analysis is carried out by focusing electron beam at least for seven different particles and the average composition is calculated.

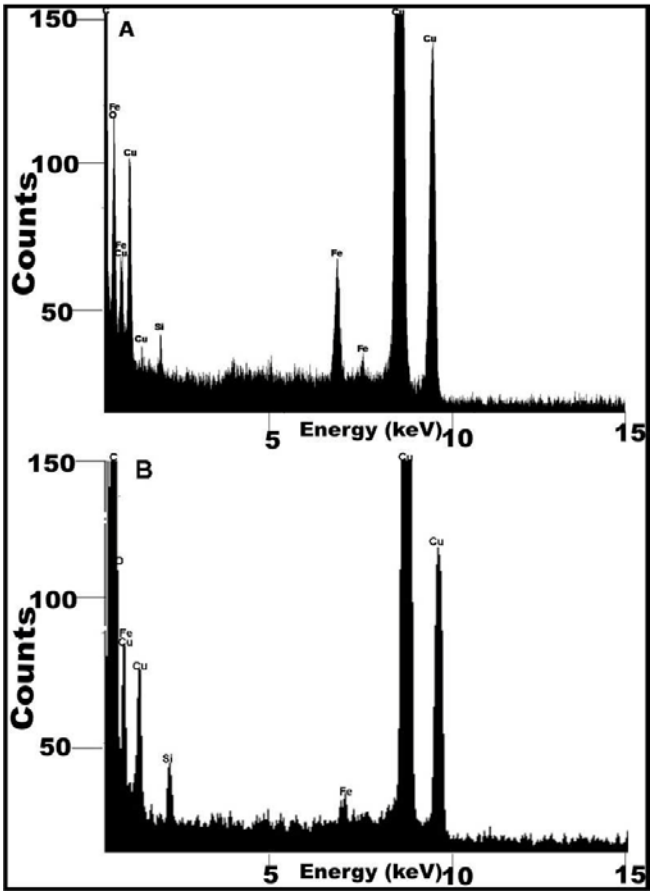

Figure 5-11(A) EDX spectrum of large Fe_3Si nanoparticles. (B) EDX spectrum for β-$FeSi_2$ nanoparticles.

Figure 5-11a is the typical EDX spectra obtained from single large Fe_3Si nanoparticles. The spectra shows approximately 3 times more intense peak for iron compare to silicon and the average composition is 0.18 ±0.01 atomic % of silicon and 0.56 ±0.02 atomic % of iron. Similarly, Figure 5-11b is a typical EDX spectra obtained from single $FeSi_2$ nanoparticles that are prepared by taking 1:2 reacting precursor molecules molar ratio of iron to silicon. The EDX spectra shows approximately 2 times intense peak of silicon to that of iron and the ratio of peak area is approximately proportional to the molar ratio of the Si to Fe. The average composition is .08 ±0.01 atomic % of iron and 0.14 ±0.01 atomic % of silicon. The overall average composition of each element is shown in table 4 and 5

Table 4 Composition of Fe_3Si nanoparticle from EDX measurement.

Element	Weight %	Atomic %	Error %
Carbon (K)	82.77	94.22	0.29
Oxygen (K)	0.05	0.04	0.03
Silicon (K)	0.74	0.18	0.02
Iron (K)	1.15	0.56	0.01
Copper (K)	15.26	5.04	0.06

Table 5 Composition of β-FeSi2 nanoparticles from EDX measurement.

Element	Weight %	Atomic %	Error %
Carbon (K)	66.05	89.90	0.31
Oxygen (K)	0.03	0.02	0.03
Silicon (K)	0.25	0.14	0.01
Iron (K)	0.30	0.08	0.01
Copper (K)	33.37	9.86	0.13

Magnetic properties of the large Fe_3Si nanoparticles are studied by using a commercial superconducting quantum interference device (SQUID) magnetometer. Figure 5-12 shows the magnetization curves with respect to the applied magnetic field at five different temperatures. At all temperatures the Fe_3Si nanoparticles do not show hysteresis loops, implying that the particles are superparamagnetic. The average saturation magnetization of large Fe_3Si nanoparticles is 60 emu/g which is very similar to that of iron oxide (Fe_3O_4) nanoparticles (61 emu/g)[36] and less than iron nanoparticles which is 171 emu/g.[37] The saturation magnetization is higher at lower temperature (10 K) and lower at higher temperature (300 K) due to increasing thermal energy that overcomes the electronic spin exchange and produces a randomizing effect.[38, 39] The absence of hysteresis is attributed to the small particle size and finite size effect in the nanoparticles.[39]

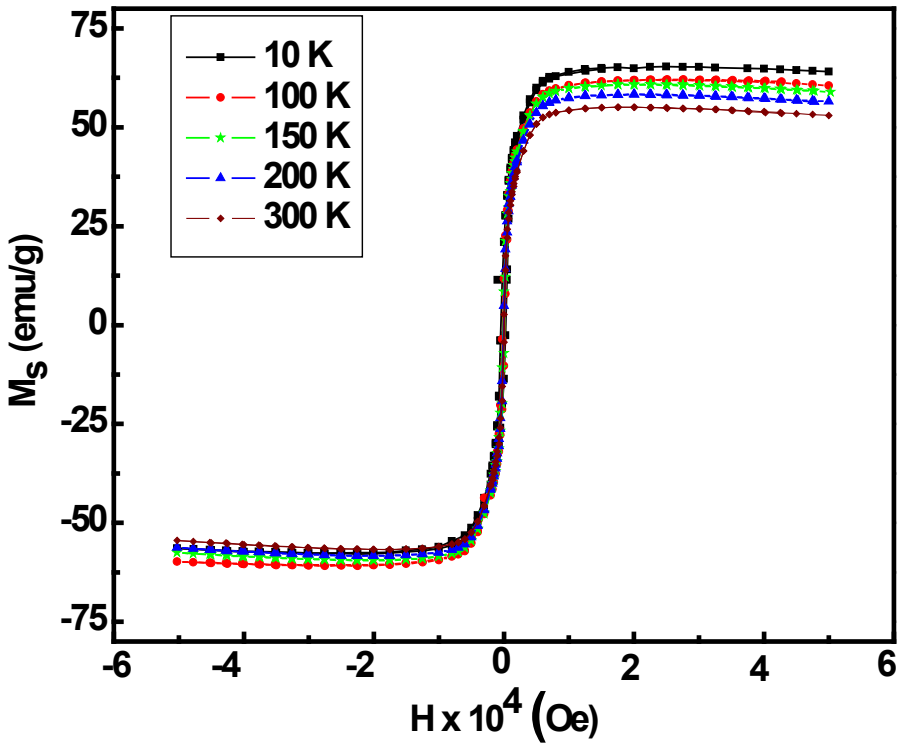

Figure 5-12 Magnetization vs applied magnetic field curve for Fe_3Si nanoparticles ranging from10 K to 300 K.

Conclusions:

Fe_3Si nanoparticles are prepared by a high temperature reduction method. The particles show superparamagnetic nature at temperature 10 K to 300 K as estimated from SQUID magnetometry measurements. The variation of mole ratios of reacting precursor molecules is a key to control the nanoparticle phase. It is believed that improvement of this work can open up a road to prepare a new class of nanoparticles that are environmentally friendly, cheaper, and technologically important.

References

1. Zichichi, A., *Silicides Fundamentals and Applications,World scientific Publishing Co.pte.Ltd. singapore*. 2000.
2. Borisenko, V. E., Semiconducting Silicides. *Springer: Berlin* **2000,** 39.
3. Hafner, J.; Spisak, D., *Phys. Rev. B* **2007,** 75, (19).
4. Hansen, M. P. A., K.rer.nat.; *Constitution of Binary Alloys*. Second ed.; McGraw- Hill Book Company: 1958, page no.713.
5. Kolel-Veetil, M. K.; Qadri, S. B.; Osofsky, M.; Goswami, R.; Keller, T. M., *J. Phys. Chem. C* **2009,** 113, (33), 14663-14671.
6. Hamaya, K.; Ueda, K.; Kishi, Y.; Ando, Y.; Sadoh, T.; Miyao, M., *Appl. Phys. Lett.* **2008,** 93, (13).
7. Mantovan, R.; Georgieva, M.; Fanciulli, M.; Goikhman, A.; Barantcev, N.; Lebedinskii, Y.; Zenkevich, A., *Phys. Status Solidi a-* **2008,** 205, (8), 1753-1757.
8. Jing, Y.; Xu, Y. H.; Wang, J. P., *J. Appl. Phys.* **2009,** 105, (7).
9. Schmitt, A. L.; Bierman, M. J.; Schmeisser, D.; Himpsel, F. J.; Jin, S., *Nano Lett.* **2006,** 6, 1617.
10. Fu, C.; Krijn, M.; Doniach, S., *Phys. Rev. B* **1994,** 49, (3), 2219-2222.
11. Filonov, A. B.; Migas, D. B.; Shaposhnikov, V. L.; Dorozhkin, N. N.; Petrov, G. V.; Borisenko, V. E.; Henrion, W.; Lange, H., *J. Appl. Phys.* **1996,** 79, (10), 7708-7712.
12. Antonov, V. N.; Jepsen, O.; Henrion, W.; Rebien, M.; Stauss, P.; Lange, H., *Phys. Rev. B* **1998,** 57, (15), 8934-8938.

13. Kulatov, E.; Nakayama, H.; Ohta, H., *J. Phys. Soc. Jap.* **2001,** 70, (7), 2199-2204.

14. Ionescu, A.; Vaz, C. A. F.; Trypiniotis, T.; Gürtler, C. M.; García-Miquel, H.; Bland, J. A. C.; Vickers, M. E.; Dalgliesh, R. M.; Langridge, S.; Bugoslavsky, Y.; Miyoshi, Y.; Cohen, L. F.; Ziebeck, K. R. A., *Phys. Rev. B* **2005,** 71, (9), 094401.

15. Min, B.-C.; Motohashi, K.; Lodder, C.; Jansen, R., *Nat. Mater.* **2006,** 5, (10), 817-822.

16. Deneke, C.; Schumann, J.; Engelhard, R.; Thomas, J.; Muller, C.; Khatri, M. S.; Malachias, A.; Weisser, M.; Metzger, T. H.; Schmidt, O. G., *Nanotechnology* **2009,** 20, (4).

17. Ando, Y.; Hamaya, K.; Kasahara, K.; Ueda, K.; Nozaki, Y.; Sadoh, T.; Maeda, Y.; Matsuyama, K.; Miyao, M., *J. Appl. Phys* **2009,** 105, (7).

18. Liew, S. L.; Seng, D. H. L.; Tan, H. R.; Chi, D. Z., *J. Phys. D-Appl. Phys.* **2009,** 42, (10).

19. Starke, U.; Weiss, W.; Kutschera, M.; Bandorf, R.; Heinz, K., *J. Appl. Phys.* **2002,** 91, (9), 6154-6161.

20. Takeda, K.; Yoshitake, T.; Sakamoto, Y.; Hara, D.; Itakura, M.; Kuwano, N.; Nagayama, K., *Int. J. Mod. Phys. B* **2009,** 23, (17), 3543-3549.

21. Schütte, M.; Wartchow, R.; Binnewies, M., *Zeitschrift für anorganische und allgemeine Chemie* **2003,** 629, (10), 1846-1850.

22. Zhang, S. L.; Ostling, M., *Crit. Rev. Solid State Mater. Sci.* **2003,** 28, 1.

23. Varadwaj, K. S. K.; Seo, K.; In, J.; Mohanty, P.; Park, J.; Kim, B., *J. Am. Chem. Soc.* **2007,** 129, (27), 8594-8599.

24. Dahal, N.; Chikan, V.; Jasinski, J.; Leppert, V. J., *Chem. Mater.* **2008,** 20, (20), 6389-6395.

25. Li, W.; Ni, C.; Lin, H.; Huang, C. P.; Shah, S. I., *J. Appl. Phys.* **2004,** 96, (11), 6663-6668.

26. Jinlian, H.; Weiping, C.; Cuncheng, L.; Yanjie, G.; Li, C., *Appl. Phys. Lett.* **2005,** 86, (15), 151915.

27. Klemmer, T. J.; Shukla, N.; Liu, C.; Wu, X. W.; Svedberg, E. B.; Mryasov, O.; Chantrell, R. W.; Weller, D.; Tanase, M.; Laughlin, D. E., *Appl. Phys. Lett.* **2002,** 81, (12), 2220-2222.

28. Hunt, T. D.; Reeson, K. J.; Homewood, K. P.; Teon, S. W.; Gwilliam, R. M.; Sealy, B. J.; *Nucl. Instrum. Meth. B* **1994,** 84, (2), 168-171.

29. Hunt, T. D.; Sealy, B. J.; Reeson, K. J.; Gwilliam, R. M.; Homewood, K. P.; Wilson, R. J.; Meekison, C. D.; Booker, G. R., *Nucl. Instrum. Meth. B* **1993,** 74, (1-2), 60-64.

30. Udono, H.; Kikuma, I.; Okuno, T.; Masumoto, Y.; Tajima, H.; Komuro, S., *Thin Solid Films* **2004,** 461, (1), 182-187.

31. Yoshitake, T.; Yatabe, M.; Itakura, M.; Kuwano, N.; Tomokiyo, Y.; Nagayama, K., *Appl. Phys. Lett.* **2003,** 83, (15), 3057-3059.

32. Oostra, D. J.; Bullelieuwma, C. W. T.; Vandenhoudt, D. E. W.; Felten, F.; Jans, J. C., *J. Appl. Phys.* **1993,** 74, (7), 4347-4353.

33. www.matter.org.uk/diffraction/electron.

34. Ueda, K.; Ando, Y.; Kumano, M.; Sadoh, T.; Maeda, Y.; Miyao, M., *Appl. Surf. Sci.* **2008,** 254, (19), 6215-6217.

35. Ebenstein, Y.; Nahum, E.; Banin, U., *Nano Lett.* **2002,** 2, (9), 945-950.

36. Lee, Y.; Lee, J.; Bae, C. J.; Park, J. G.; Noh, H. J.; Park, J. H.; Hyeon, T., *Adv. Func. Mater.* **2005,** 15, (3), 503-509.

37. Gong, W.; Li, H.; Zhao, Z. G.; Chen, J. C., *J. Appl. Phys*. **1991,** 69, (8), 5119-5121.

38. Sellmyer, D., Skomski, Ralph, *Adv. Magn. Nanostructures*. Springer: 2006 p507.

39. Lu, A. H.; Salabas, E. L.; Schuth, F., *Angew. Chem. Int. Edit.* **2007,** 46, (8), 1222-1244.

40. Nature, 152 (1943) P. 413-413, www.webmineral.com

CHAPTER 6 - Preparation of Iron and Gold Silicide Nanodomains on Silicon (111) by the Reaction of Gold, Iron-Gold Core-Shell, and Alloy Nanoparticles with Triethylsilane

Introduction

Heterogeneous catalytic reactions are widespread and are commonly performed with the reactant(s) and product(s) in the liquid or gas phase and the catalyst in the solid phase; with the reaction occurs at the interface between the phases. The surface properties of a heterogeneously supported catalyst are significant factors in the effective use of that catalyst.[1] The composite nanoparticles of iron and gold can also act as heterogeneous catalyst. Specifically, heating gold, iron-gold alloy and iron-gold core-shell nanoparticles deposited on Si (111) can provide the accessible reaction sites through their interfaces. The reactions in the interfaces cause the reactant chemisorption and product desorption. This growth method allows the production of a large variety of novel nanostructures.[2-7] Most heterogeneous catalysts are composed of a selected combination of active materials, promoter and support. The implementation of combinatorial techniques to heterogeneous catalysis is a significantly more challenging problem than in other application areas of materials sciences.[1] Additional challenges arise from the complex and dynamic nature of catalyst. If new sets of catalysts are used, the range of materials produced with the new catalysts can be significantly extended despite being complex and dynamic. In this manuscript, a novel idea is explored: oxidation-sensitive catalysts that can be prepared in a form that one can be used under atmospheric conditions, and still exhibit catalytic activity towards producing composite semiconductor nanostructures at elevated temperatures.

As a specific example, composite iron-gold alloy, core-shell and gold nanoparticles are heated on Si (111) substrate in absence and presence of silicon precursor (triethylsilane). This

method allows for the production of silicides of both iron and gold on the silicon substrate. Iron shows catalytic activity in producing gold silicide (Au_5Si_2) and gold shows the catalytic activity in producing iron silicide (β-$FeSi_2$) on the silicon substrate. However, colloidal iron nanoparticles are prone to oxidation, which seems to exclude the possibility to introduce iron nanoparticles from colloidal synthesis. Iron is the fourth most abundant element in the earth's crust, which would make iron a desirable material to address problem such as solar energy conversion[8-12]on a large scale. Effective bandgap calculations and experiments show that a decrease in the size of the β-$FeSi_2$ results in a direct bandgap (0.85 eV) leading to more efficient capture of photons and allowing some bandgap tunability upon quantum confinement.[13,14] The theoretical solar energy conversion efficiency of β-$FeSi_2$ is 16-23 %.[15] The beta iron silicide is non-toxic, ecologically friendly semiconductor and has large absorption coefficient. The optical absorption coefficient is greater than 10^5 cm^{-1} at 1eV, which is 50 times larger than that of crystalline silicon.[15, 16]

Interestingly, iron silicide has many phases and only the beta silicide is a semiconductor. The bulk phase diagram (see supplemental information figure S5) of iron and silicon shows at least five known iron silicide compounds (Fe_3Si, Fe_5Si_3, FeSi, β-$FeSi_2$, and α-$FeSi_2$).[17] According to the phase diagram, ε -FeSi, β-$FeSi_2$, and Fe_3Si are stable at room temperature while Fe_2Si, and Fe_5Si_3 are the metastable. β-$FeSi_2$ can be fabricated by using different methods: including powder metallurgical methods,[18-20] polycrystalline thin film by electron beam evaporation,[21-23] magnetron sputtering,[24] plasma ion processing,[25] continuous wave laser and pulse laser deposition,[26-28] solid phase epitaxy,[29-31] reactive deposition epitaxy, molecular beam epitaxy,[32,33] and chemical vapor deposition.[34]

To address some of the challenges with the outlined goals, this study investigates the reaction of colloidal iron-gold core-shell and iron-gold alloy nanoparticles with Si (111). The change in height of the heated nanoparticles is monitored by atomic force microscopy (AFM) to investigate how the three different nanoparticles react and collapse on the Si (111) surface. In addition, the nucleation of silicide on the deposited nanoparticles is explored, which show catalytic activity to produce nanostructures from gas phase precursors.

Experimental Section

Gold, iron-gold alloy and iron-gold core-shell nanoparticles are deposited on 1×1 cm^2 Si (111). Prior to the deposition, the Si (111) is washed with double distilled water and sonicated in acetone for five minutes. The clean silicon wafer is etched with 40% hydrofluoric acid for 15 minutes and dried in a vacuum. The nanoparticles are deposited on the Si (111) by dipping the silicon wafers in the nanoparticle solution for five minutes. Gold and iron-gold core-shell nanoparticles solutions are prepared in toluene and an iron-gold alloy nanoparticles solution is prepared in aqueous phase (0.01 gm nanoparticles are dissolved in 50 ml Toluene and ultrapure water in each case). After loading, the Si (111) wafer is held under vacuum (~10^{-7} Torr) and heated to 500 ^{o}C at the rate of 10 ^{o}C per minute. When the temperature reaches 500 ^{o}C, the wafer is maintained for 20 minutes in order to melt the nanoparticles on the silicon substrate. The wafers are cooled to room temperature for its characterizations. In second part of the experiment, the nanoparticle loaded wafers are annealed to 500 ^{o}C in the presence of flowing precursor molecules (triethylsilane). Argon is used as a carrier gas for the silicon precursor. The flow of argon through the silicon precursor (triethylsilane maintained at 30 ^{o}C) is controlled at constant rate of 25 mTorr during heating for 20 minutes. The wafers are cooled to room temperature and characterization is performed. In third part of the experiment, the nanoparticle loaded wafers are

heated to 800 ^{o}C under conditions similar to that of the 2nd part of the experiment for two hours. Experiments are carried out in the set up shown in Figure 1.

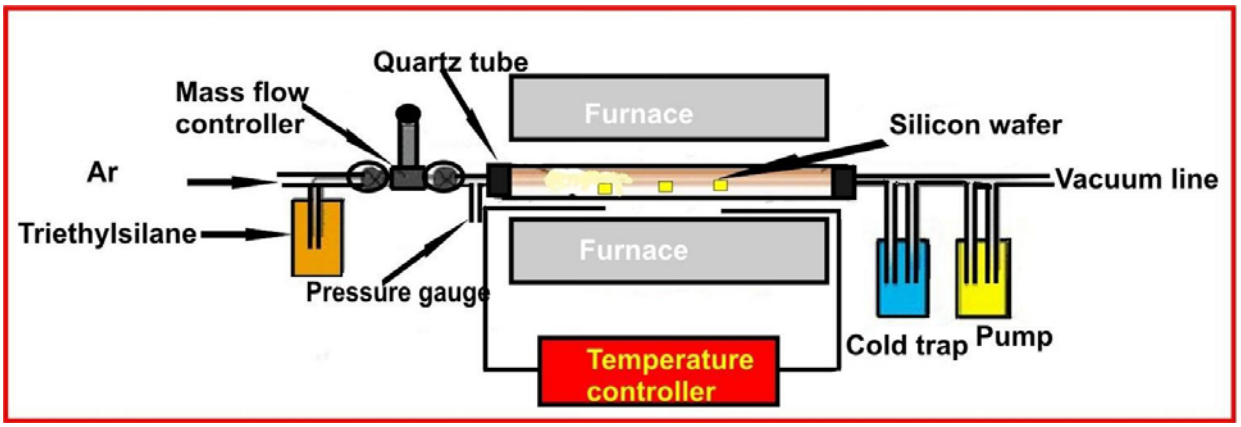

Figure 6-1 Experimental set up for the preparation of silicide nanodomains on silicon (111)

Iron-gold core-shell nanoparticles are synthesized modifying the method previously described by Wang et.al.[35] Briefly, in the first step an iron seed solution is prepared and in the second step the particles are coated with gold shell. Both steps are carried out in argon atmosphere to reduce the oxidation of the iron nanoparticles. In a typical synthesis, a solution is prepared from 0.2 ml of iron pentacarbonyl (99.9 %), 15 mL of dioctylether (99 %), 1.5 mL of oleic acid (99 %), 1.5 mL of oleyl amine (70 %), and 2.5 g of 1, 2-hexadecanediol (90 %). The solution is refluxed at 230 ^{o}C for 2.3 hours. In the next step, 0.56 g of gold (III) acetate (99.9%), 2.5 g of 1, 2-hexadecanediol, 1.5 mL oleic acid, 2.5 mL of oleyl amine and 25 mL of dioctylether is added to 10 mL solution of the iron nanoparticles. The solution is heated at the rate of 15 ^{o}C/ min and refluxed at 210 ^{o}C for 2 hours. Following this step, the solution is cooled to room temperature and treated with ethanol (99 %) to precipitate the nanoparticles. The nanoparticle slur is centrifuged at 8500 rpm for an hour and a precipitate containing the nanoparticles is

deposited at the bottom of centrifuge tube. The precipitate is washed with ethanol several times and vacuum dried at room temperature for 10 hours. Afterwards, the solid nanoparticles aggregates are magnetically separated from the non-magnetic part. The magnetic portion of the nanoparticles is collected and redispersed in hexane in the presence of 1.5 mL oleic acid and 1.5 mL oleyl amine. The experimental yield for the magnetic portion of the material is 31 %.

The preparation of iron-gold alloy nanoparticles follows the previously described literature method.[36] Briefly, 0.4 mL of iron pentacarbonyl (99 %) is injected into 20 mL of toluene (110 ºC) containing 0.08 mole of didodecyldimethylammonium bromide. After 20 minutes, $AuCl_3$, $3.3x10^{-4}$ mole and sodium salt of mercapto propane sulphonic acid, $5.6x10^{-3}$ mole are added to the solution. The gold was slowly reduced by drop wise addition of 2 mL of 2M aqueous sodium borohydride. The nanoparticles are precipitated with ethanol and centrifuged for 15 minutes at 7000 rpm. The nanoparticles are washed with ethanol and chloroform several times before vacuum drying for 10 hours. The magnetic part of the sample is collected for the experiments and the yield is 23 %.

Detailed characterization of the etched samples is performed using tapping-mode atomic force microscopy (AFM) measurements. A Digital Instrument multimode AFM with Nanoscope IIIa electronics is employed. Tapping-mode pyramidal AFM tips are purchased from Nanosensors. Transmission electron microscopy (TEM) is performed on a Philips CM100 microscope operated at 100 kV. Powder X-ray diffraction (XRD) patterns are recorded by a Bruker D8 X-ray diffractometer with Cu Kα radiation. The scanning electron microscope (SEM, S-3500N) is used to observe the particle morphology. High-resolution transmission electron microscopy (HRTEM) is performed using a JEOL JEM2010 instrument operating at 200 kV and equipped with a LaB6 electron source. X-ray photoelectron spectroscopy (XPS) analysis is

performed using an Al Kα anode as the excitation source and the emitted electrons collected with a SPECS hemispherical analyzer operated at 25 eV pass energy. Any effects due to sample charging (which were minimal) were calibrated using the carbon 1s photoelectron peak (284.6 eV). Synchrotron based x-ray absorption near edge spectroscopy (XANES) measurements were performed at the undulator beamline 8.0.1 at the Advanced Light Source, Lawrence Berkeley National Laboratory. XANES experiments were conducted using the total electron yield detection method where the total photocurrent is measured as the photon energy is scanned through the absorption edges. All spectra are normalized to the photocurrent from a gold grid. The experimental energy resolution is ~0.15 eV at the Fe L_3-edge. For both the XPS and XANES measurements, spectra are taken at base pressures of less than 5 x 10^{-9} Torr. Triethylsilane (97%) is used as the silicon precursor.

Results and Discussion

First, the height change of the gold, iron-gold core-shell and iron-gold alloy nanoparticles is explored during heating of the nanoparticles on the Si (111). The change in height of the nanoparticles during heating gives the approximate surface melting and diffusion behavior of the nanoparticles on the substrate. Figure 2 shows the TEM images of the gold, iron-gold core-shell, and iron-gold alloy nanoparticles used in the experiment before heating on the silicon substrate. The particles have narrow size distributions as evident by the histograms at the bottom of Figure 6-2. The average size distribution of these particles is determined by taking approximately 200 particles for each sample. The composition of the alloy nanoparticles and core-shell nanoparticles are 14.8 mol ± 4.7 % and 25 mol ± 5.0 % of iron, respectively. The deposition of the nanoparticles is followed by heating on the Si (111). The changes in height of the nanoparticles after heating are determined by tapping mode AFM.

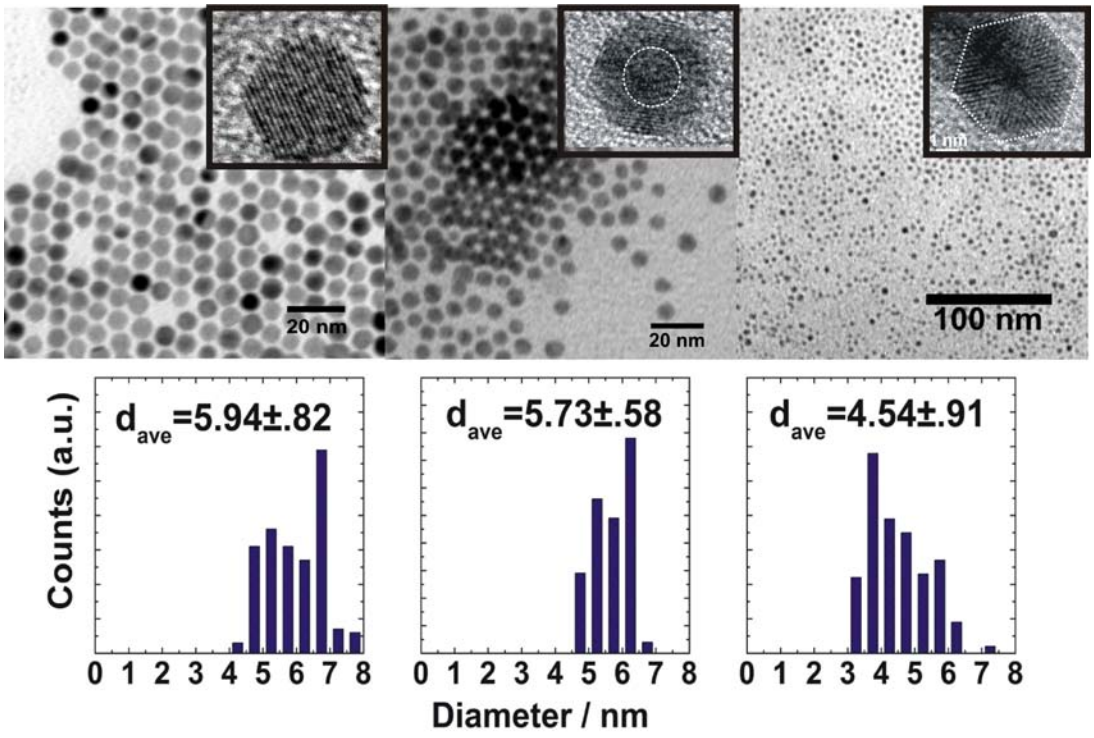

Figure 6-2 Transmission Electron Microscope (TEM) images of pure gold, iron-gold core-shell and iron-gold alloy nanoparticles. The insets show the High-Resolution Transmission Electron Microscope (HRTEM) images of a selected nanoparticle from each sample. The histograms represent the particles distributions for each sample.

In order to increase the visibility of the particles during analysis, the AFM images of the nanoparticles on Si (111) are enhanced by taking the negative eigenvalues of the Hessian function of the images (see supplemental material Figure S1). This process ensures the minimization of the artifacts associated with the AFM technique (such as spikes). The histograms of the particles are generated by the height measurement of several hundreds of the nanoparticles. The surface roughness of the Si (111) is also measured as a reference (see

supplemental material Figure S2) and the root mean square (RMS) value of 0.2 nm is estimated showing very little variation when no nanoparticles are deposited on the surface. The surface treatment of the Si (111) also plays an important role in the height determination of the nanoparticles. If the surface is untreated, the nanoparticles are embedded inside the oxide layer upon heating. A similar finding has been reported by Robinson et al where they prepared a gold catalyzed silicon oxide layer on a silicon substrate.[37] With substrates not treated with hydrofluoric acid, the nanoparticles submerge into the surface, therefore making the height measurements of the particles ambiguous. As an example, the impressions created by gold nanoparticles at 200 ºC are shown in Figure S3 (b). When the surface is treated with dilute hydrofluoric acid, the native oxide layer is removed exposing the Si (111). The same nanoparticles on the treated Si (111) do not show any impressions of oxide formation within the resolution of measurement limits (see supplemental material Figure S3 left). While the oxide layer may grow over time, its contribution to the height analysis is assumed to be negligible since the heat treatments are carried out in vacuum.

The height distributions as a function of heating temperature of the gold, iron-gold core-shell and iron-gold alloy nanoparticles are also studied (see supplemental material Figure S4). The room temperature height distribution of the nanoparticles on Si (111) is consistent with the height distribution of the particles from the TEM image. The data shows that when the particles are heated, the height distribution decreases due to the collapse of the particles. The summary of the results is shown in Figure 6-3 where the error bars derive from the standard deviation of the average size and not from the error of the measurements, which is significantly smaller. First, gold nanoparticles show a slight increase in height from 25 ºC to 200 ºC. Above 300 ºC, the heights of the gold nanoparticles suddenly decrease from ~ 6 nm to ~ 3.5 nm. The initial

increase in height is most likely due to the result of coalescence followed by partial recrystallization of the nanoparticles. During coalescence and recrystallization, the clusters undergo a spontaneous shape deformation to lower their surface free energy. The height decrease above 300 ºC may be the result of the gold silicide formation, which has been confirmed previously in the literature.[38-43]

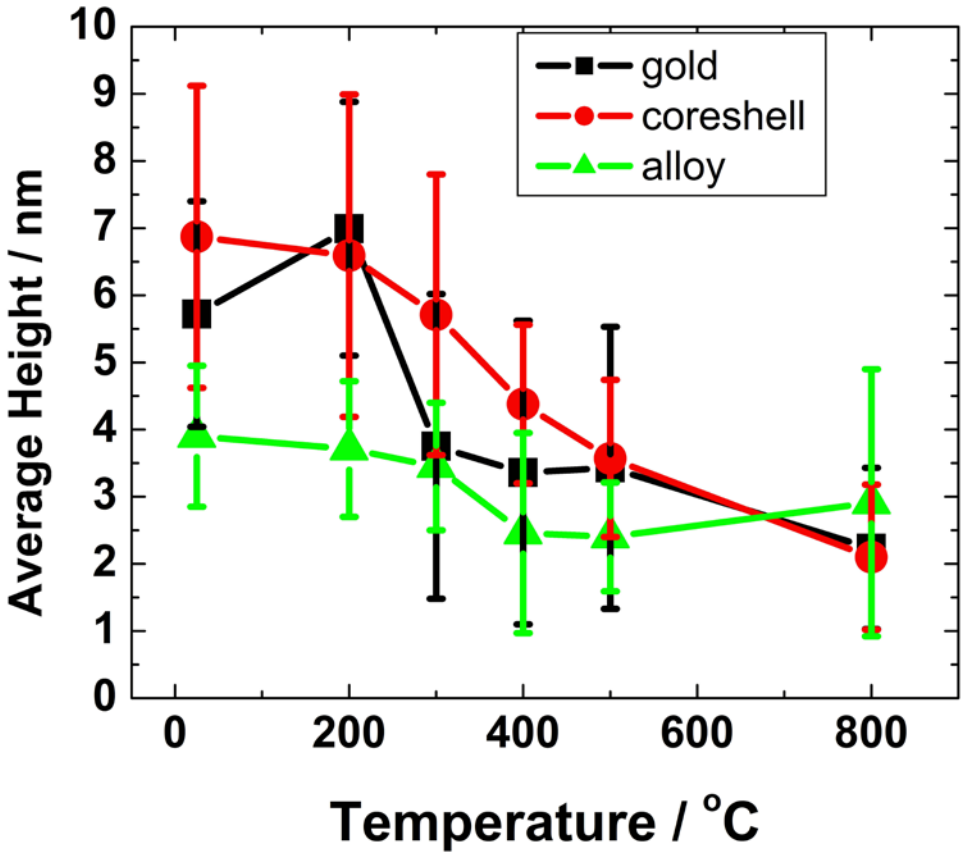

Figure 6-3 the change in height profile of iron-gold core-shell, alloy, and gold nanoparticles as a function of temperature

X-ray photoelectron spectroscopy (XPS) is performed to identify the nature of the species formed during heating. As observed in Figure 4a, distinct spectral changes are observed when

monitoring the Si 2p and Au 4f photoelectron peaks. At 200 ^{o}C, evidence for metallic Au ($4f_{7/2}$ photoelectron at 84 eV) and silicon (2p photoelectron at 99 eV) with a small contribution from SiO_2 (103 eV) is seen. The difference between the Si and SiO_2 peaks (3.8 eV) is consistent with previous literature .[44] Interestingly, the Si(KLL) Auger peak at ~93 eV has a noticeable shoulder at 89 eV, which has been previously reported to be a sign of alloying in silicon.[45] This observation suggests that even at this lower temperature, some form of alloying is already occurring in these materials.

As the temperature is increased from 200-400 ^{o}C (middle trace, Figure 6-4a), a small shift in the Au 4f photoelectron peaks is observed, indicative of silicide formation.[46] A small shift to lower binding energy for the Si 2p peaks is observed, along with a large peak at ~104 eV. It should be noted that the origin of this peak cannot be simply ascribed to an increase in SiO_2 content for two reasons: (1) the heating steps were performed in a vacuum; therefore there is little oxygen during the process and (2) the splitting between the two peaks is now 4.9 eV, nearly 1 eV higher than the 200 ^{o}C trace. Indeed, this behavior is most likely related to the formation of the gold silicide. As the sample is further heated to 500 ^{o}C, a drastic change in the photoemission spectrum is observed (top trace, Figure 4a). First, a peak related to silicide formation is observed at ~100.3 eV which is similar to energy shifts seen in other silicide.[47, 48] Second, the metallic Au 4f photopeaks are missing; instead, they are replaced with a new gold silicide photopeak appearing at ~90 eV. This assignment is not inconsistent with previous literature reports of large binding energy shifts in the Au 4f peaks as a function of gold oxidation state.[49] The broadness of the peak at 90 eV (~ 3.5 eV) versus the metallic Au peak at 84 eV (~1.2 eV) suggests this peak is actually a broadened two component peak (comprising of both the $4f_{7/2}$/$4f_{5/2}$).

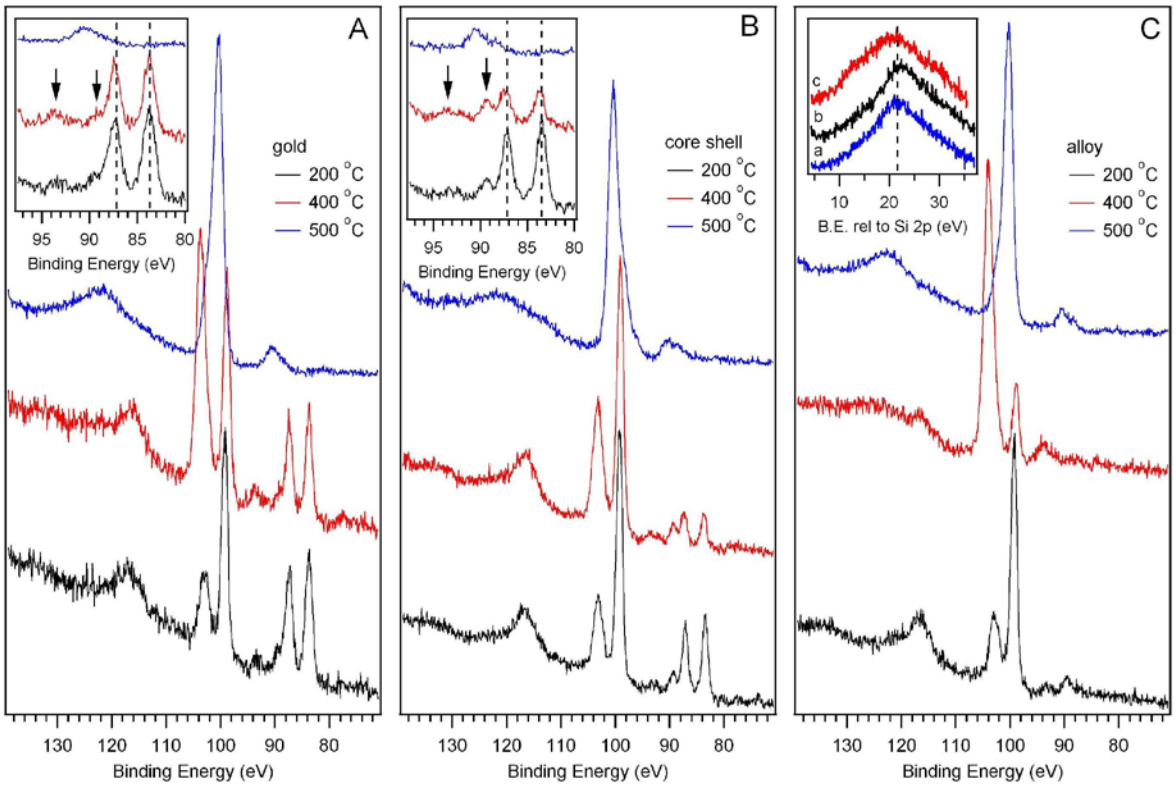

Figure 6-4 XPS spectra of (A) pure gold, (B) iron-gold core-shell and (C) iron-gold alloy nanoparticles as a function of temperature. The insets in (A) and (B) are zoomed regions expanding the Au 4f photoelectron peaks with the traces plotted in the same order as the full scale plots. The inset in (C) plots the Si 2p plasmon loss feature for (a) pure gold, (b) iron-gold alloy and (c) iron-gold core-shell nanoparticles heated at 500 ^{o}C.

Core-shell nanoparticles display significantly different behavior compared to the gold nanoparticles. The overall trend still shows a decrease in the average height of the particles, but there is no sudden temperature-dependent collapse of the particles. In this case the iron core clearly plays a significant role in retarding the complete collapse of the nanoparticles, which is expected due to the higher melting point of iron. Qualitatively, the results from alloy

nanoparticles are similar to the results from the heating of the core-shell nanoparticles. The nanoparticles heights collapse between 300-400 ºC, which is higher than that of the gold nanoparticles by approximately 100 ºC. It is speculated that the difference in melting dynamics of the iron containing nanoparticles compared to the pure gold nanoparticles will lead to more efficient tethering of the particle on the surface (decreased nanoparticle mobility on the surface) via silicide formation. This suggestion is supported by the XRD results shown in Figure 6-6 (ii & iii). Gold silicides are less stable than the iron silicide at above the eutectic temperature (363^{o}C) and forms mostly the metastable silicides Au_3Si, Au_2Si, Au_5Si_2, and Au_7Si_5.[43, 50-52]

Figure 6-5 shows the XRD patterns of gold, alloy, and core-shell nanoparticles on Si (111) substrate after heating at 500 ^{o}C. The figure indicates that the gold nanoparticles remains as fcc gold with only a little amount of Au_5Si_2 formation as indicated by a small peak at 69.5^{o} 2θ corresponding to (416) atomic reflection of fcc Au_5Si_2 (Figure 6-5 i). The small XRD peak at 2θ 28.4^{o} corresponds to Si (111). The XRD peaks at 38.2º, 44.4º, 64.8º, 77.6º, and 82.0^{o} 2θ angles correspond to the (111), (200), (220), (311), and (222) fcc atomic reflections of gold respectively. The observation of a large amount of fcc gold via XRD is surprising from our XPS results in Figure 4A; however, when one considers the differences in depth probing between XPS and XRD, this result is not too surprising. The inelastic mean free path (IMFP), λ, of a gold 4f electron excited at 1486 eV (Al Kα) is ~2 nm[53]. The intensity, *I*, of the XPS experiment can be expressed as $I \propto \exp(-\lambda)$, which means that ~95% of the signal arises from a depth of ~3λ indicating the probe depth of the XPS experiment is ~6 nm. This suggests that the surface layer of these materials is comprised of the silicide, while the metallic fcc gold resides > 6 nm below the surface and will be the subject of a future manuscript.

Conversely, alloy and core-shell nanoparticles form a mixture of both crystalline gold silicide Au_5Si_2 and iron mono silicide FeSi, (Figure 6-5 ii & iii). When compared to literature values[51-59] the XRD peak at 2θ 57.0 is associated with (220) atomic reflection of iron mono silicide. General inspection of the XPS spectra in Figures 4b and c show qualitatively similar behavior to the pure gold nanoparticles. Namely, as the temperature is increased, shifting of the Si 2p photoelectron peaks is observed followed by a complete transformation of the 2p feature at 500 ^{o}C. Slight differences in line shapes may suggest different forms of silicide (i.e. both iron and gold) but analysis of the Si 2p features alone cannot provide a complete picture of iron silicide formation. It is extremely interesting to note that at 200 ^{o}C, the alloy nanoparticles show no evidence for metallic gold peaks, and only at higher temperatures do the 4f photopeaks that we previously attributed to gold silicide formation.

Creation of iron silicide is confirmed with near edge x-ray absorption spectroscopy (XANES) as observed in Figure 6-7. For both the core-shell and alloy nanoparticles, as the temperature is increased, an increase in the Fe L_3-edge XANES feature at ~706 eV suggests formation of iron silicide.[54] The formation of iron silicide is also supported from analysis of the Si plasmon features from XPS (inset, Figure 4C) where it has been reported the energy of this loss feature is a fingerprint for silicide formation.[55,56] While we observe a plasmon energy of 17.4 eV for bulk Si (spectra not shown), the loss features for all the 500 ^{o}C treated materials fall between 21-22 eV, consistent with silicide formation.

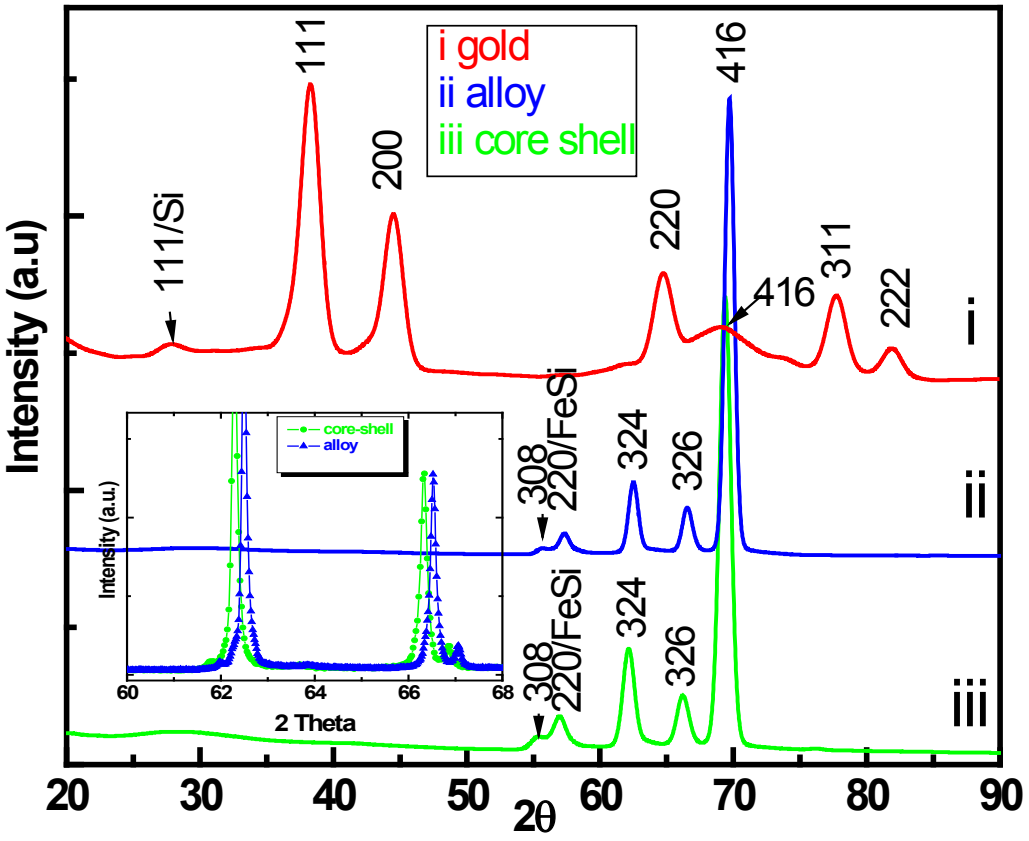

Figure 6-5 XRD of pure gold (i), iron-gold core-shell (ii), and iron-gold alloy (iii) nanoparticles heated at 500°C. The inset in the middle shows the shift in 2θ angle of alloy nanoparticles as compared with core-shell nanoparticles.

The XRD peaks at 2θ angles 55.4º, 62.2º, 66.3º, 69.5º are associated with gold silicide (Au_5Si_2) (308), (324), (326), and (416) atomic reflections respectively. Nearly identical XRD peaks of the gold silicide are observed in case of core-shell and alloy nanoparticles annealed at 500 °C in the absence of silicon precursor (Figure 5a ii & iii). However, the (416) atomic reflection is at the same 2θ in all three experiments and confirms the formation of gold silicide Au_5Si_2 but its formation is significantly higher in the cases of alloy and core-shell nanoparticles due to a catalytic effect from the iron atom.

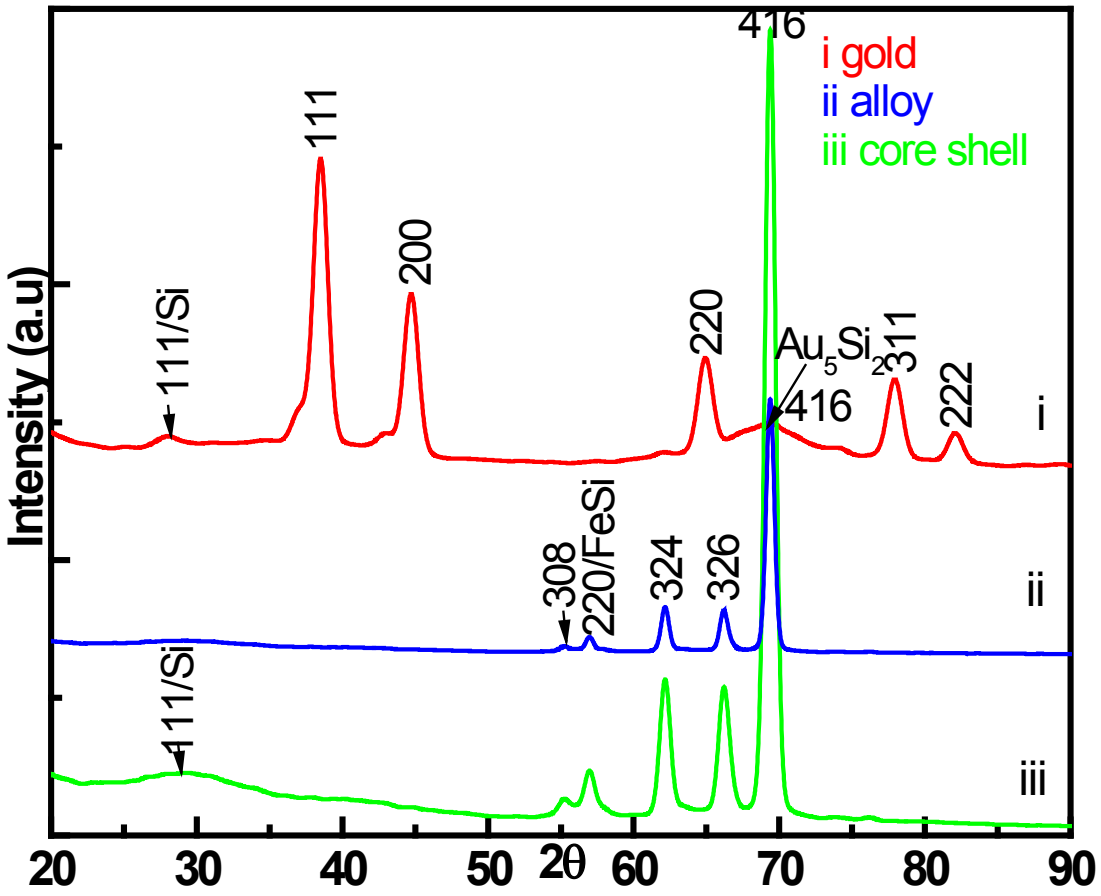

Figure 6-6 shows the XRD of same particles presented in fig 6-5 after storing several months in air.

The results refer to common bimetallic catalysts where both components are present on the surface.[57] Specifically the results imply that the more oxophilic iron atom catalyzes the silicide formation attached to the neighboring, less oxophilic gold center. Furthermore, iron, which has higher surface energy than gold and silicon, helps in the formation of gold silicide from core-shell and alloy nanoparticles. At room temperature, the surface free energies of thin

films of iron, gold, and silicon are 2.9 Jm^{-2}, 1.9 Jm^{-2}, and 1.4 Jm^{-2} respectively.[58-60] It is observed that both gold and iron mono silicides obtained from the alloy nanoparticles show an upward shift in XRD peak position (~ 0.4^{o}) for each peak compared to the gold and iron silicide from core-shell nanoparticles. In Figure 6-5 only the peak position (416) can be seen as upward shifted. The figure with overlapping scale (inset) clearly shows the shift for all reflections of silicide from alloy nanoparticles. In the core-shell nanoparticles, the active iron atoms remain protected by the gold shell (see supplemental information S6) and this reduction of available iron atoms on the surface causes the significant decrease in surface potential energy and results in the observation of a lack of upward shift of XRD peak position. The average lattice constant of face centered cubic (fcc) Au_5Si_2 and iron mono silicide obtain from the alloy nanoparticles are found to be 19.49 Å and 4.44 Å, respectively. The values of the lattice constants obtained in this experiment are contracted compared to the reported literature values of 19.50 and 4.46 Å[52]. As shown in Figure 5a ii & iii, gold silicide (Au_5Si_2) is the major crystalline (the sharp XRD peaks) product while heating the alloy and core–shell nanoparticles on the silicon substrate. The results provide an indirect piece of evidence that there is not homogeneous distribution of gold and iron silicide in the nanoparticles. The major cause of the growth of such structures is due to the relaxation of strain which is associated with large lattice mismatch. However, thermal heating and surface reconstructions at higher temperature alter the atomic arrangements at the surface leading to change the surface potential; this might cause the formation of gold and iron silicide structures on the silicon substrate. The presence of Au_5Si_2 reported herein is different from the literature[38, 39,41,52,61] where it is noted that gold can form silicide at room temperature.

Figure 6-6 shows the XRD patterns obtained from the same sample presented in Figure 5a after several months of exposure to air. Identical XRD spectrums of the products of gold and iron-gold core-shell nanoparticles imply that there is no change in compositions of the products; i.e. there is no oxidations of the products (Figure 6-6 i & ii). However, the composition of alloy nanoparticles is changed and the XRD peak position of iron-gold alloy nanoparticles are shifted by ~ 0.4^0 and overlap with the XRD peaks of silicide obtained from core-shell nanoparticles (Figure6-5 iii). Neither the oxidation of iron nor the silicon is observed from the XRD results within the accuracy of the measurements. However, in case of alloy nanoparticles the more oxophilic iron atom is mostly on the surface of the nanoparticles. The oxophilic metal center may activate the silicon leading to the formation of a thin sublayer of silicon oxide or iron oxide on top of the product crystals over the time. The thin sublayer produces different residual strain on the nanoparticles surface and cause to change the 2θ angles in the XRD spectrum.

We next investigate the effect of the presence of a silicon precursor on these nanoparticles. The sample is annealed at 500 ^oC (Figure 6-8 i) in presence of flowing triethylsilane. Upon annealing, the gold nanoparticles are completely converted into crystalline gold silicide, Au_5Si_2. Unlike in the previous case (Figure 6-5 i), the XRD peaks are observed at 2θ angles 62.2º, 66.3º, 69.5º corresponding to (324), (326), and (416) atomic reflections of gold silicide (Au_5Si_2), respectively. Gold silicide may be formed as a result of a reaction between the gold nanoparticles and silicon from the precursor. In this experiment, silicon is supplied from substrate as well as from the gaseous precursor and ensures enough nucleation of silicon on the nanoparticles forming gold silicide. Figure 6-8 (ii) shows the XRD pattern obtained after annealing the sample at higher temperature (800 ^oC).

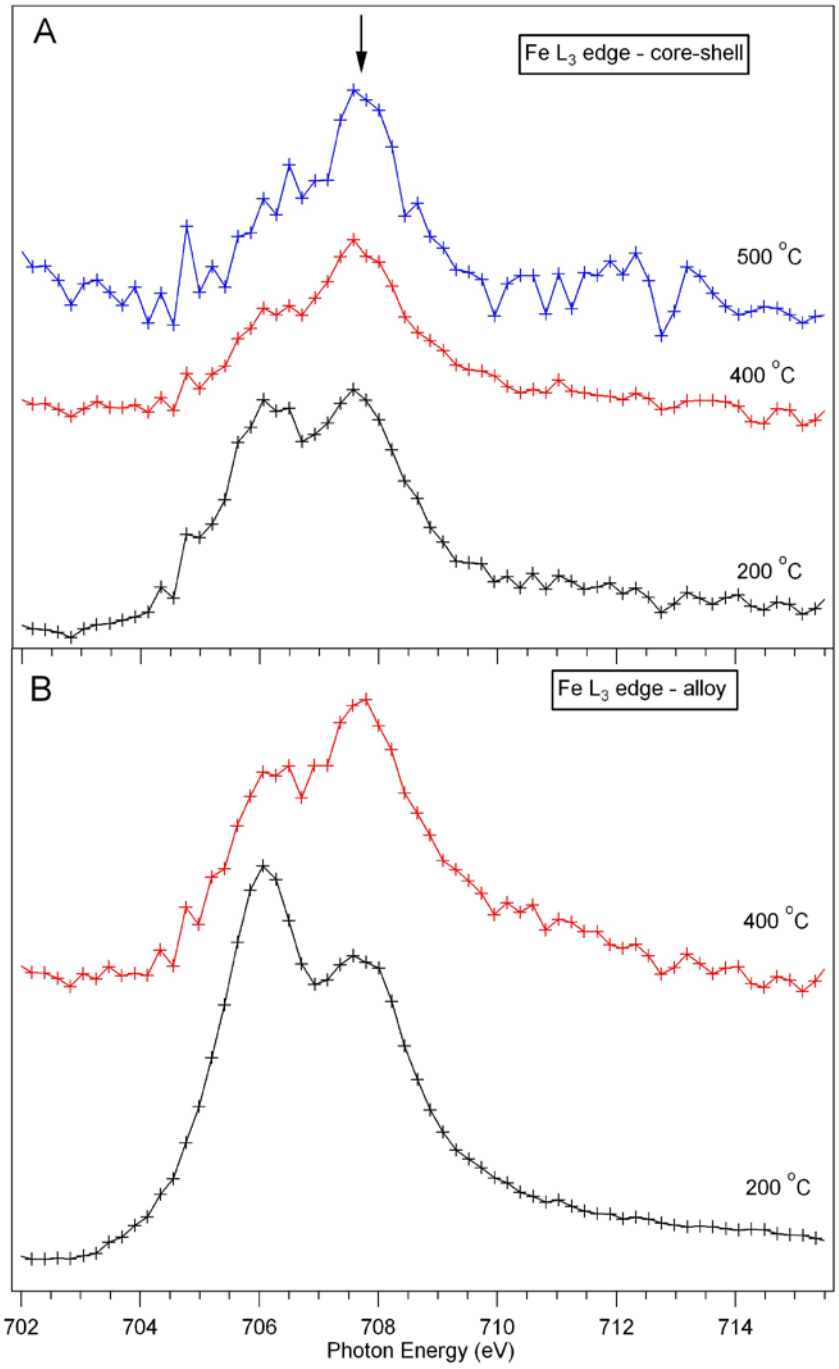

Figure 6-7 Fe L_3-edge XANES spectra for (A) iron-gold core-shell, and (B) iron-gold alloy nanoparticles as a function of temperature.

Here only the (326) and (416) atomic reflections of gold silicide are observed; and (324) atomic reflection is absent. This process is explained based on the established literature of gold-silicon chemistry: Gold and silicon have a relatively low eutectic temperature; at higher temperature gold-iron mixture remains as a liquid eutectic alloy. It is reasonable to expect the surface crystallization and layering while cooling the samples. Subsequent solidification gives rise to non-epitaxial growth of gold silicide on top of silicon substrate. The result is composed of numerous protruding gold silicide particles with random orientation on silicon substrate as shown in Figure 6-11f. The atomic rearrangement due to surface dangling bond and nucleation of silicon in the nanoparticles might be expected to change atomic packing and bonding during heating. In order to verify the orientation of the nanostructure on silicon substrate, XRD are taken by sample rotation around the surface normal axis and no noticeable changes in the XRD data are observed, indicating that the diffracting layers consist of randomly oriented crystallites that causes the appearance and disappearance of diffraction peaks. Figure 6-9 (i) shows the XRD pattern of core-shell nanoparticles annealed at 500 oC in the presence of flowing triethylsilane on silicon substrate. The figure shows that the sample forms the β-FeSi2 phase on the surface after annealing. No crystalline materials are formed on the surface in the absence of the nanoparticles. The atomic reflections associated with β-FeSi2 are labeled in the figure. The orthorhombic crystal structure with space group Cmca and lattice constants a = 9.863, b = 7.791, and c = 7.833 Å is expected to show at least 134 reflections in the XRD. However, only 11-12 XRD reflections of β-FeSi2 are observed on silicon (111) substrate (either from core-shell or alloy nanoparticles).

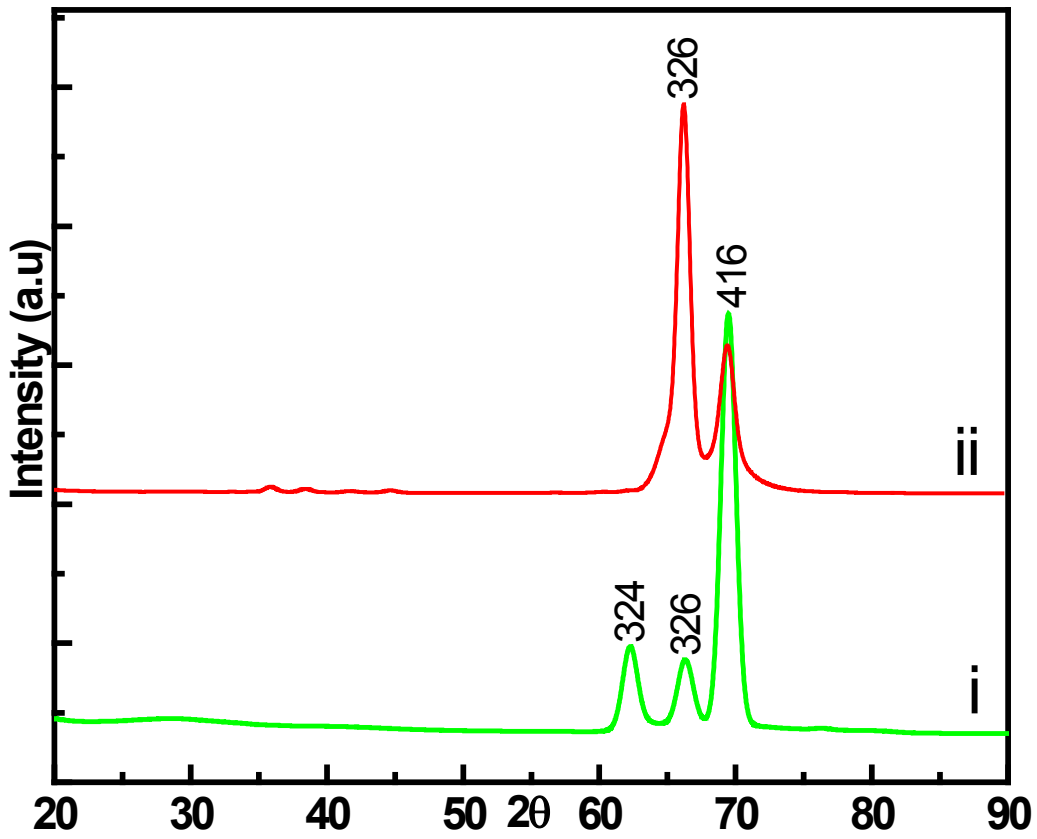

Figure 6-8 XRD of pure gold nanoparticles heated at 500 (i) and 800 °C in presence of gas silicon precursor.

To our knowledge, no complete experimental XRD spectrum of β-$FeSi_2$ nanoparticles has been presented in the literature.[26, 62-70] When the sample is annealed at 800 °C with triethylsilane, the (023), (440), (006), (262), and (535) atomic reflections disappear (Figure 6-9 ii). New atomic reflections appear at 65.0°, 78.0°, and 84.4° 2θ angles corresponding to (424), (045), and (354) atomic reflections of the β-$FeSi_2$. The broadening of the (111) atomic reflection of Si is attributed to higher deposition of excess silicon from the precursor and the segregation of β-$FeSi_2$

nanoparticles due to strain-induced crystallization during annealing. Obviously, the driving force for the segregation is the difference between the surface energies of gold, iron, and silicon. Not surprisingly, at higher temperature dissociation of iron-gold pair takes place and the iron precipitates out from the active lattice sites. This is because the activation energy of diffusion for iron (0.42 eV) is lower than the activation energy of precipitation (0.7 - 0.9 eV) of iron at higher temperature in silicon (111).[71] The precipitated iron combines with the silicon precursor and forms the β-$FeSi_2$ as shown in Figure 6-11b and 6-11d where the crystal size is significantly increased.

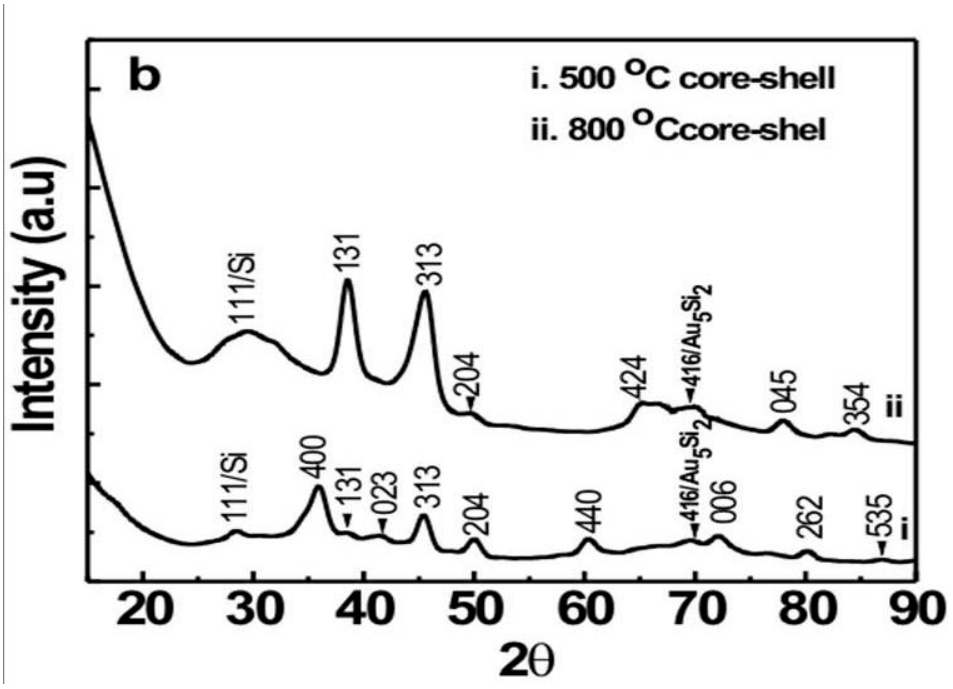

Figure 6-9 XRD of iron-gold core-shell nanoparticles heated at 500 (i) and 800°C (ii) in presence of flowing silicon precursor molecules.

Figure 6-10 (i) shows the XRD pattern obtained by heating the alloy nanoparticle loaded silicon wafer in the presence of triethylsilane. The figure shows a trend similar to that of the β-$FeSi_2$ layer obtained from core-shell nanoparticles. However, the intensity of the peaks is higher and a significant broadening of the (416) peak of Au_5Si_2 is observed. The reasons for the broadening are: 1) more gold atoms are exposed to the surface in the alloy; 2) a thicker layer of β-$FeSi_2$ is present and, 3) there is a high degree of segregation of atoms. Due to the segregation of atoms in the surface, a new broad (200) atomic reflection at 17.6º 2θ is observed.

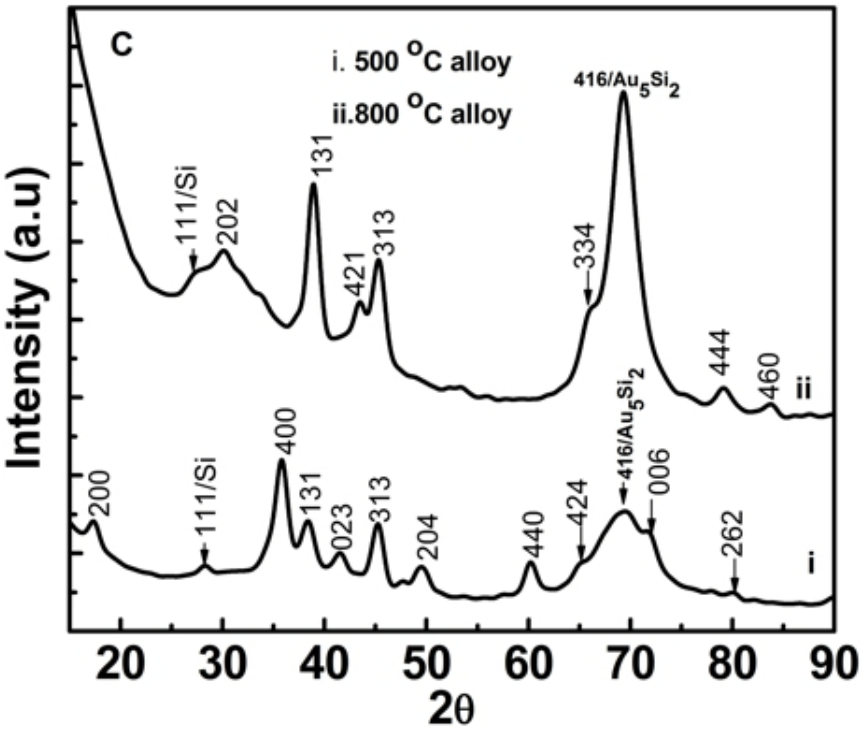

Figure 6-10 XRD of iron-gold alloy nanoparticles heated at 500 (i) and 800°C (ii) in presence of flowing silicon precursor molecules.

When the sample is annealed at 800 ºC, additional reflections are observed: (202), (421), (334), (444), and (460). The presence of additional reflections implies that at higher temperature the interfacial reactions increase due to defects and surface twins that cause the change in texture of the particles, like the previous case of gold silicide. As the annealing temperature increases, the volume fraction of the nanodomains and silicon content increase indicating the growth of β-$FeSi_2$ nanostructure as shown in Figure 6-11b, 6-11d and table 6. The lattice mismatch between silicon substrate and the β-$FeSi_2$ layer produces the local variation of the interatomic distances in the sample and generates different XRD spectra. The crystal structure of β-$FeSi_2$ prepared from both alloy and core shell nanoparticles are identical; only the orientation distribution is different. This difference manifests itself in the relative intensities of the diffraction peaks. Similar to the β-$FeSi_2$ obtained from core-shell nanoparticles, no XRD peak for either gold or gold silicide is observed in the case of alloy nanoparticles. It is important to note that the Si (111) atomic reflections are not observed either in the case of alloy nanoparticles heated in absence of precursor (Figure 6-5, ii and 6-6,ii) or for gold nanoparticles heated in the presence of triethylsilane (Figure 6-8, i & ii).

In Figures 6-11a &b, the scanning electron microscope (SEM) images of iron-gold core-shell nanoparticles deposited on Si (111) and heated in the presence of triethylsilane at 500 ^{o}C and 800 ^{o}C are shown. The morphology of the particles at 500 ^{o}C is not significantly different from that of the particles deposited at room temperature (data not shown). When the sample is annealed at 800 ^{o}C, the image shows dramatic changes in the morphology and in the contrast of the particles. The particles appear more crystalline and they show some order on the surface. A similar phenomenon is observed in case of iron-gold alloy nanoparticles at 800 ^{o}C as shown in Figures 6-11c & 6-11d. The results are consistent with the XRD results shown previously, where

fewer atomic reflections are observed at 800 ^{o}C due to the preferred orientation of the particles on the silicon substrate. In the case of gold nanoparticles, the preferred orientation is not observed as shown in Figures 6-11e & 6-11f. The partial ordering observed in Figures 6-11b & 6-11d is probably the result of the single crystal substrate. When the iron containing part of the catalyst forms the iron silicide, cracks develop which leads to some migration of the other nanoparticles into the crack leading to the observed pattern.[67, 72]

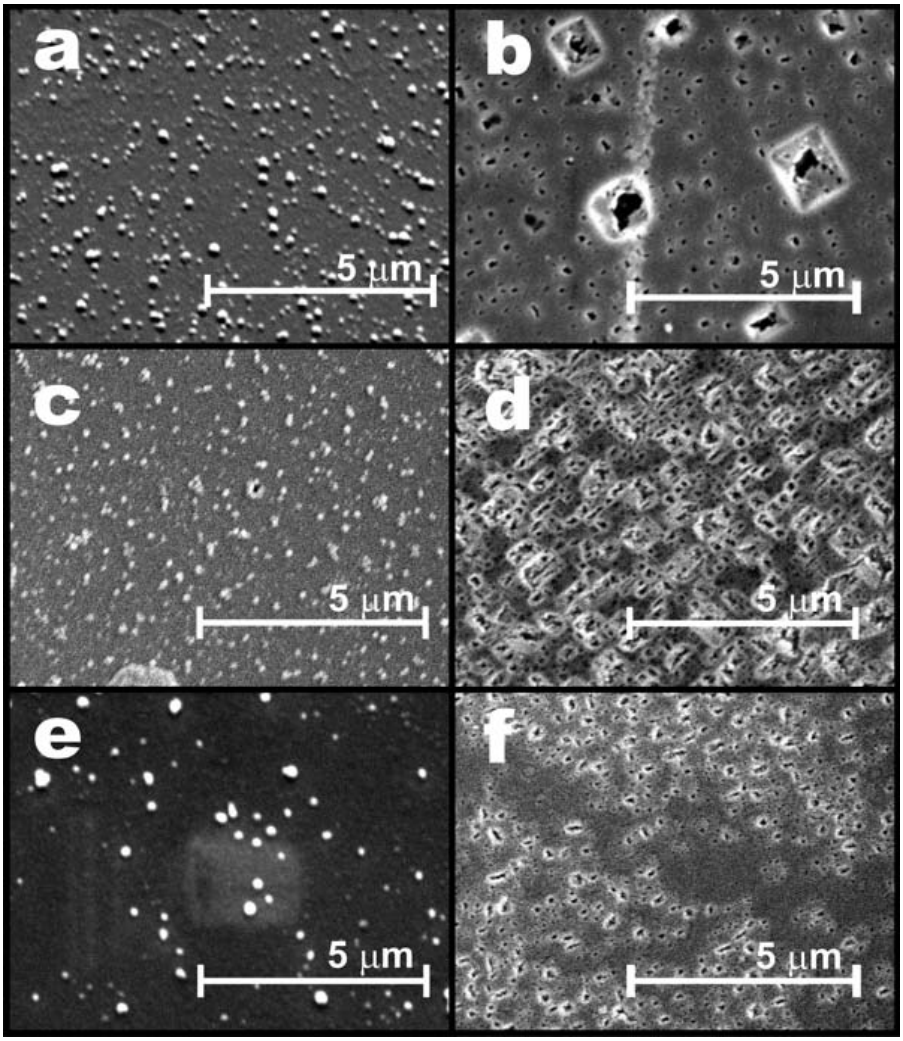

Figure 6-11 Scanning electron microscope (SEM) images of iron-gold core-shell nanoparticles heated at 500 and 800^{o}C in presence of flowing precursor molecules, respectively. (c-d) SEM images of iron-gold alloy nanoparticles heated at 500 and 800^{o}C in presence of flowing precursor molecules, respectively, and (e-f) SEM images of gold nanoparticles heated at 500 and 800^{o}C in presence of flowing precursor molecules.

Compositions of the silicides that are obtained after heating the alloy and core-shell nanoparticles in presence of triethylsilane are listed in Table 6. The composition is measured by

using energy dispersive X-ray analysis (EDX) attached to the SEM. The comparison of the surface composition of the iron silicide obtained from core-shell nanoparticles at 500 ^{o}C and at 800 ^{o}C shows that the silicon concentration is increasing, but the relative amount of iron remains almost the same. As expected, silicon is nucleating in the nanoparticles and forms the β-$FeSi_2$ nanoparticle layer. At 800 ^{o}C interestingly gold is not observed probably because of gold silicide instability and iron precipitate out forming iron silicides. In the case of the iron-gold alloy nanoparticles, the amount of silicon at 800 ^{o}C also increases compared to the sample heated to 500 ^{o}C. The relative amount of gold is reduced, similar to the results using core-shell nanoparticles. At the same time, sodium and sulfur are completely removed, and the amount of oxygen is increased from desorption of ligands (sodium salt of mercapto-3 propane sulphonic acid). The absence of sodium, sulfur and the reduced amount of carbon at 800 ^{o}C shows removal of ligands from the nanoparticles.

Table 6 Composition of iron silicide at two different temperatures; obtained form gold-iron core-shell and alloy nanoparticles

Composition of iron silicide from Fe-Au alloy nanoparticles					Composition of iron silicide from Fe-Au core-shell nanoparticles				Silicon wafer + silicon precursor		Silicon wafer only	
Element	500°C		800°C		500°C		800°C		500°C		500°C	
	Wt. %	At. %	Wt. %	At. %	Wt. %	At. %	Wt %	At. %	Wt. %	At. %	Wt. %	At. %
Silicon K	46.72	32.77	54.94	42.85	40.65	26.33	46.63	31.63	25.86	100.00	0.35	100.00
Iron K	8.33	7.83	8.22	9.17	16.60	12.64	16.35	9.64	-	-	-	-
Gold M	4.37	0.41	3.62	0.38	3.81	0.38	-	-	-	-	-	-
Carbon K	35.33	54.47	30.77	44.19	35.47	56.50	37.02	58.73	-	-	-	-
Oxygen K	1.87	2.16	2.45	3.41	3.47	4.15	-	-	-	-	-	-
Sulphur K	1.61	0.93	-	-	-	-	-	-	-	-	-	-
Sodium K	1.77	1.43	-	-	-	-	-	-	-	-	-	-

Conclusions

This work has explored the possibilities of using composite iron-gold, core-shell, alloy and gold nanoparticles to form iron and gold silicide (β-$FeSi_2$, FeSi & Au_5Si_2). Heating the composite nanoparticles at different temperatures reveals distinctly different behaviors. Gold collapses at lower temperature due to the formation of gold silicide. The formation of gold silicide is catalyzed by iron atom. The iron-containing nanoparticles collapse at a significantly higher temperature. The silicide is also formed from the gas phase silicon precursor of triethylsilane, which means that the nanoparticles are available for nucleation. The β-$FeSi_2$ obtained in this experiment is a narrow band gap semiconductor and potential photovoltaic material. Although the iron silicide system has not currently been the subject of much attention in the literature, simple strategies for the preparation of these materials, like those presented in this manuscript, could prove to be of great potential and very useful for future studies on nanostructured iron silicides.

Acknowledgement

The authors are grateful to the Department of Chemistry at Kansas State University for funding. The Advanced Light Source is supported by the Director, Office of Science, Office of Basic Energy Sciences, of the U.S. Department of Energy under Contract No. DE-AC02-05CH11231.

Supporting information is available

A method of AFM image analysis to increase the accuracy of height measurements of nanoparticles is presented. AFM images of the nanoparticles on etched and unetched silicon

(111) substrate and AFM image of Si (111) without the nanoparticles. Histograms of the height measurements of the nanoparticles at six different temperatures, Phase diagram of iron-silicon system and XRD of iron-gold core-shell nanoparticles at 25 and 500 ^{o}C are available.

Increasing visibility of nanoparticles in AFM pictures:

In AFM particles size is defined by the maximum height of the particles and gives the three dimensional projection of the nanoparticles. The deposited nanoparticles on Si (111) are analyzed by tapping mode AFM. Banin and co-workers pointed out that the nanoparticles height could be underestimated by AFM in free air because the recorded height is the some of the topography and the force gradient contribution.[1] Therefore, to increase the visibility of the particles during analysis, the AFM images of nanoparticles on Si (111) are enhanced by the taking the negative eigenvalues of the Hessian function of the image. The image enhancement step is followed by the selection of a 15 nm diameter circular region encompassing the visually enhanced particles. The difference between the median of the lowest 3 pixels and highest three pixels are taken as the height of the particle. The entire process is shown in Figure S1.

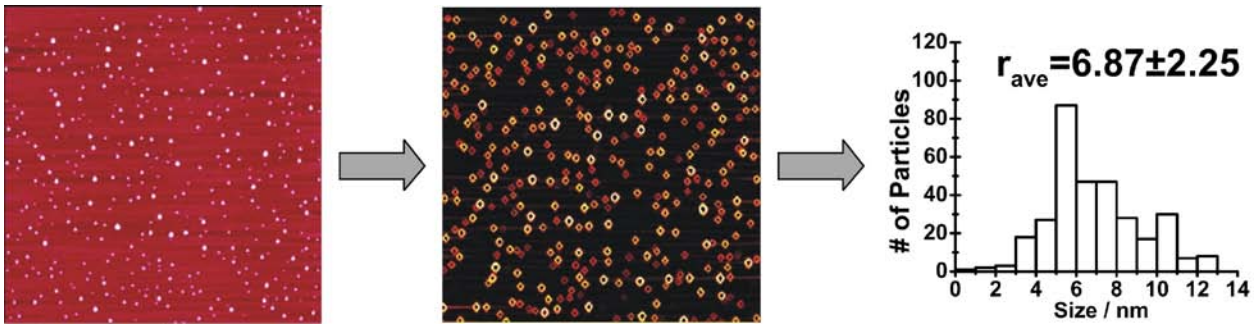

Figure S1 Tapping mode Atomic Force Microscope (AFM) images (5x5µm) of gold nanoparticles heated at 200^{o}C and a method of calculation height distribution of the particles

[1] Ebenstein, Y.; Nahum, E.; Banin, U., *Nano Lett.* **2002,** 2, (9), 945-950.

Study of surface roughness:

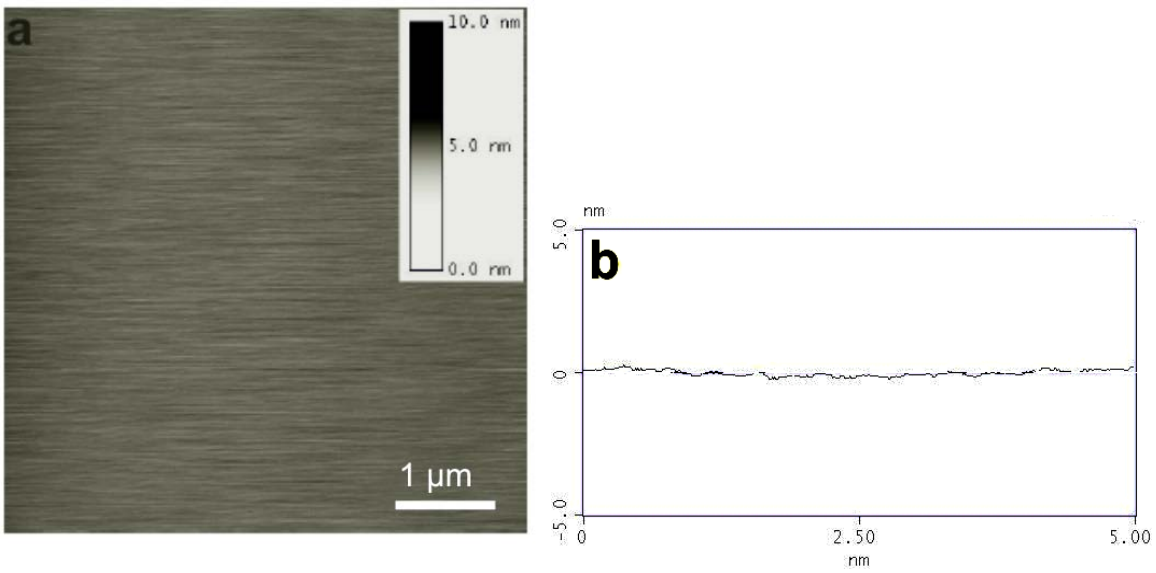

Figure S2 (a) AFM image (1x1 µm) shows the surface roughness of bare silicon (111) surface. b) Shows the section analysis of the same bare silicon (111).

The surface roughness of Si (111) is studied by using tapping mode AFM as shown in Figure S1a (5x5µm) .The surface roughness of Si (111) is calculated to be 0.2 nm by section analysis according to Figure S1b.The behavior of nanoparticles loaded Si (111) is studied by using AFM in both hydrogen fluoride etched surface and not etched surface. The etched surface clearly shows the absence of oxide layer and actual size of the nanoparticles is clearly seen as shown in Figure S3 a. However, the unetched surfaces shows plenty of oxide of silicon and submerge the nanoparticles inside the layer during heating as shown in Figure S3 b. Gold nanoparticles are taken as an example in this case.

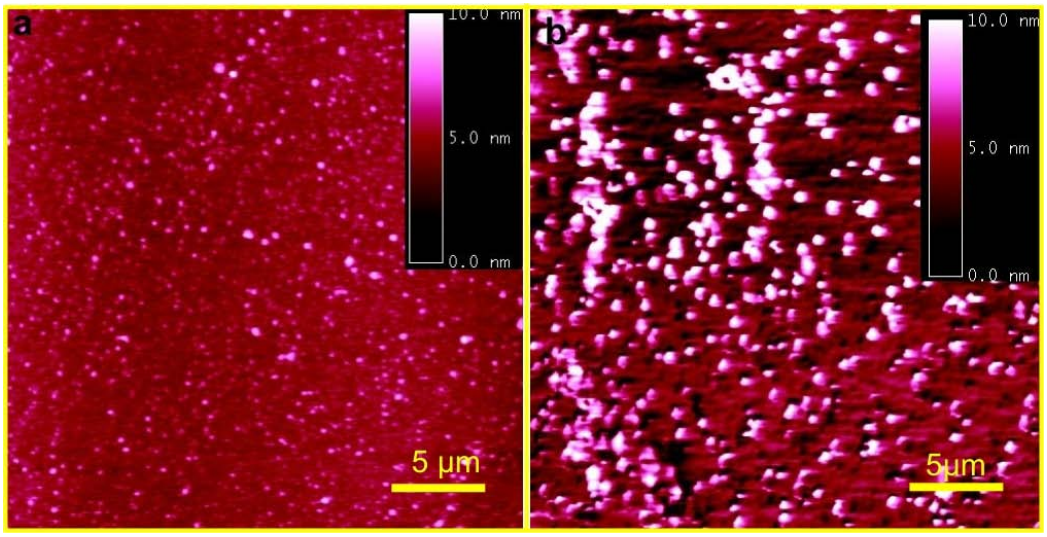

Figure S3 a AFM image of gold nanoparticles on etched surface and unetched silicon (111) surface b (5x5 µm).

Height measurements:

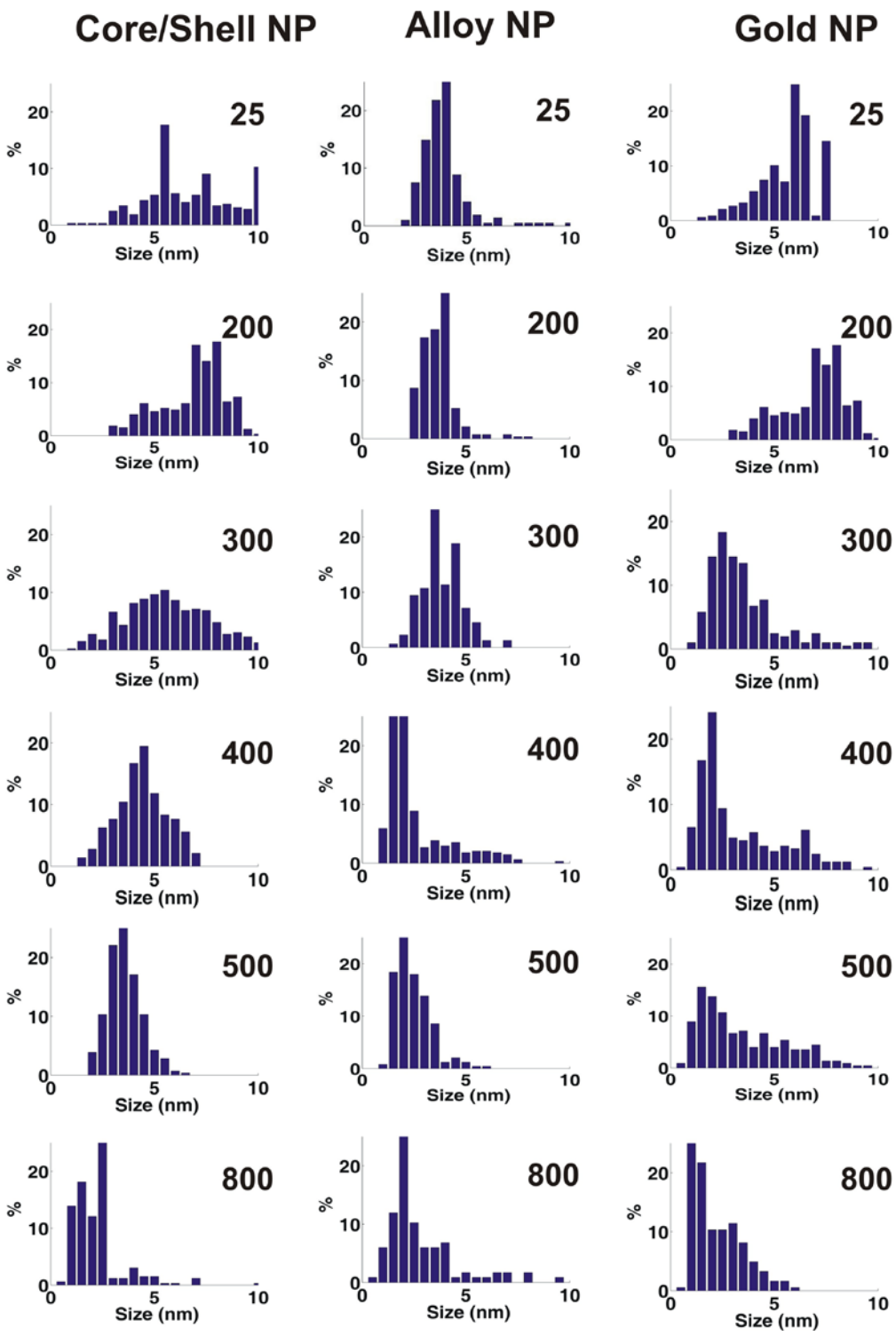

Figure S4 Histograms and corresponding height distributions of iron-gold core-shell, alloy and gold nanoparticles heated at 25, 200, 300, 400, 500, and 800°C in vacuum on silicon (111) substrate

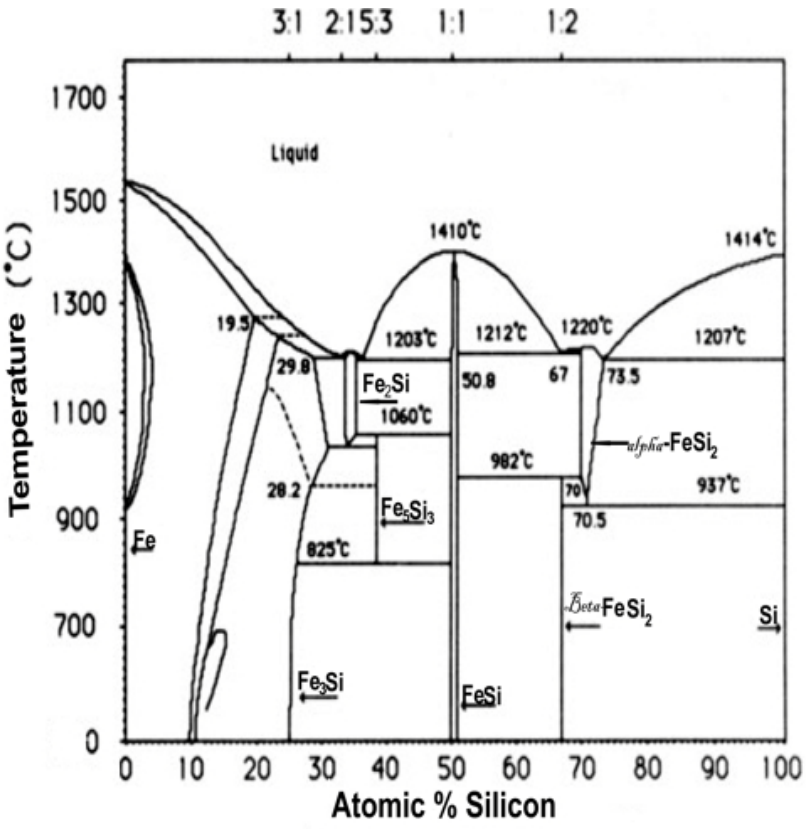

Figure S5 Iron-silicon phase diagram. Figure is reprinted from reference no.17 in main manuscript. The iron to silicon ratios of different silicide are indicated in upper horizontal axis.

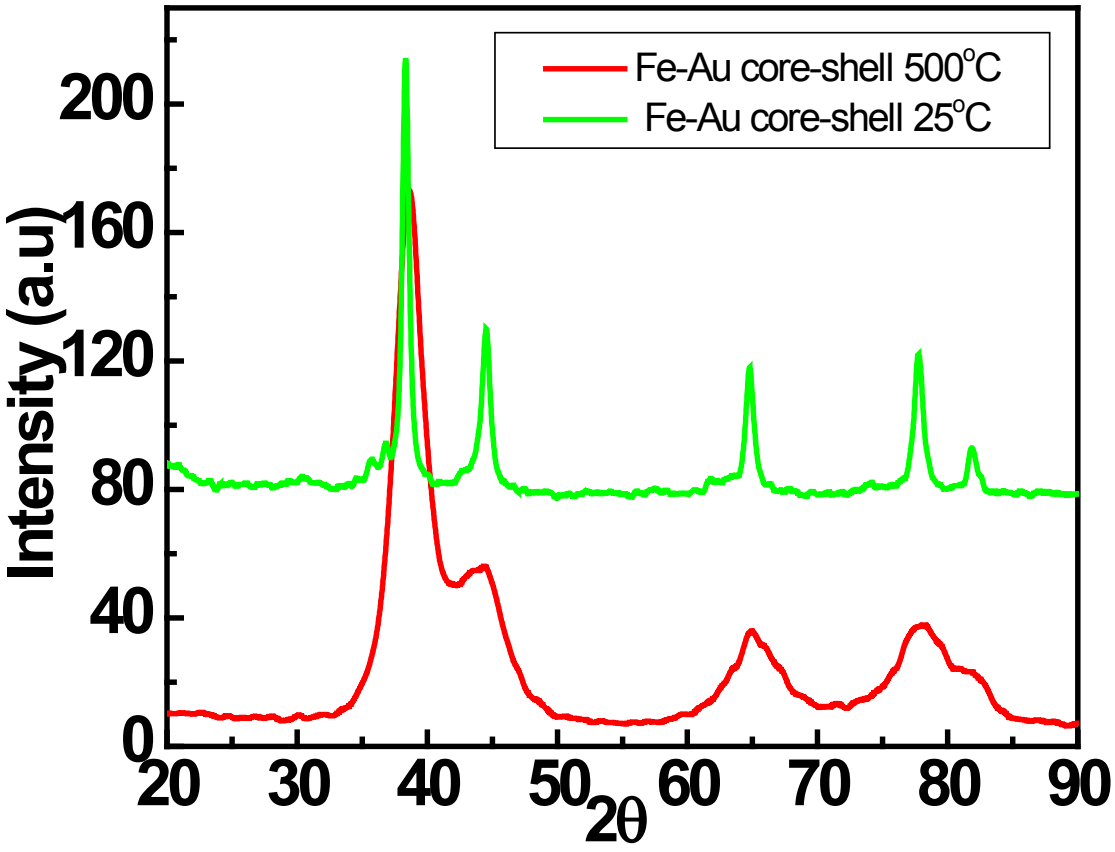

Figure S6 XRD patterns of Fe-Au core-shell nanoparticles at 25 and 500 ^{o}C. The figure shows a small peak of Fe_3O_4 at 34.4^{o} 2θ while heating the nanoparticles at 500 ^{o}C. The results indicate that most of the iron atoms remain protected by the gold shell.

References

1. Selim, S., *Angew. Chem. Int. Edit.* 2001, 40, (2), 312-329.
2. Kim, B. J.; Tersoff, J.; Kodambaka, S.; Reuter, M. C.; Stach, E. A.; Ross, F. M., *Science* 2008, 322, (5904), 1070-1073.
3. Wang, W.; Lu, X. L.; Zhang, T.; Zhang, G. Q.; Jiang, W. J.; Li, X. G.,. *J. Am. Chem. Soc.* 2007, 129, (21), 6702-+.
4. Wang, H. T.; Xie, Z. P.; Yang, W. Y.; Fang, J. Y.; An, L. N., *Crystal Growth Des.* 2008, 8, (11), 3893-3896.
5. Nagashima, K.; Yanagida, T.; Oka, K.; Tanaka, H.; Kawai, T., *Appl. Phys. Lett.* 2008, 93, (15).
6. Dick, K. A.; Deppert, K.; Karlsson, L. S.; Wallenberg, L. R.; Samuelson, L.; Seifert, W., *Adv. Fun. Mater.* 2005, 15, (10), 1603-1610.
7. Dai, Z. R.; Pan, Z. W.; Wang, Z. L., *Adv. Fun. Mater.* 2003, 13, (1), 9-24.
8. Kamat, P. V., *J. Phys. Chem. C* 2007, 111, (7), 2834-2860.
9. Buonassisi, T.; Istratov, A. A.; Marcus, M. A.; Lai, B.; Cai, Z. H.; Heald, S. M.; Weber, E. R., *Nat. Mater.* 2005, 4, (9), 676-679.
10. Brown, P.; Kamat, P. V., *J. Am. Chem. Soc.* 2008, 130, (28), 8890-+.
11. Farrow, B.; Kamat, P. V., *J. Am. Chem. Soc.* 2009, 131, (31), 11124-11131.
12. Jose, R.; Thavasi, V.; Ramakrishna, S., *J. Am. Ceramic Soc.* 2009, 92, (2), 289-301.
13. Christensen, N. E., *Phys. Rev. B* 1990, 42, (11), 7148.
14. Antonov, V. N.; Jepsen, O.; Henrion, W.; Rebien, M.; Stauss, P.; Lange, H., *Phys. Rev. B* 1998, 57, (15), 8934-8938.

15. Liu, Z. X.; Osamura, M.; Ootsuka, T.; Kuroda, R.; Makita, Y.; Tanoue, H.; Fukuzawa, Y.; Otogawa, N.; Nakayama, Y., *Thin Solid Films* 2006, 515, (4), 1532-1538.

16. Matsumoto, M.; Sugie, K.; Kawauchi, T.; Fukutani, K.; Okano, T., *Jap. J. Appl. Phys.* 2006, 45, (3B), 2390-2394.

17. Hansen, M. P. A., Krernat.; *Constitution of Binary Alloys*. Second ed.; McGraw- Hill Book Company: 1958 , page no.713.

18. Gross, E.; Riffel, M.; Stohrer, U., *J. Mater. Rese.* 1995, 10, (1), 34-40.

19. Birkholz, U.; Finkenra.H; Naegele, J.; Uhle, N., *Phys. Status Solidi* 1968, 30, (1), K81-&.

20. Kojima, T., *Phys. Status Solidi A* 1989, 111, (1), 233-242.

21. Herz, K.; Powalla, M., *Appl. Surf. Sci.* 1995, 91, (1-4), 87-92.

22. Won, J.; Kovacs, A.; Naito, M.; Ishimaru, M.; Hirotsu, Y., *J. Appl. Phys.* 2007, 102, (10).

23. Takakura, K.; Ohyama, H.; Takarabe, K.; Suemasu, T.; Hasegawa, F., *J. Appl. Phys.* 2005, 97, (9).

24. Komabayashi, M.; Hijikata, K.; Ido, S., *Jap. J.Appl. Phys.* 1991, 30, (2), 331-334.

25. Heinrich, A.; Griessmann, H.; Behr, G.; Ivanenko, K.; Schumann, J.; Vinzelberg, H., *Thin Solid Films* 2001, 381, (2), 287-295.

26. Yoshitake, T.; Nakagauchi, D.; Nagayama, K., *Jap. J. Appl. Phys.* 2003, 42, (7B), L849-L851.

27. Yoshitake, T.; Nagamoto, T.; Nagayama, K., *Thin Solid Films* 2001, 381, (2), 236-243.

28. Yoshitake, T.; Nagamoto, T.; Nagayama, K., *Mater. Sci. Eng. B* 2000, 72, (2-3), 124-127.

29. Lefki, K.; Muret, P.; Cherief, N.; Cinti, R. C., *J. Appl. Phys.* 1991, 69, (1), 352-357.

30. Gallego, J. M.; Miranda, R., *J. Appl. Phys.* 1991, 69, (3), 1377-1383.

31. Kataoka, K.; Hattori, K.; Miyatake, Y.; Daimon, H., *Phys. Rev. B* 2006, 74, (15).

32. Yoshiaki, N.; Yasushi, N.; Sung-Pyo, C.; Nobuo, T.; Masakazu, I., *J. Appl. Phys.* 2006, 100, (4), 044313.

33. Peale, D. R.; Haight, R.; Ott, J., *Appl. Phys. Lett.* 1993, 62, (12), 1402-1404.

34. Zybill, C. E.; Huang, W., *Inorg. Chimica Acta* 1999, 291, (1-2), 380-387.

35. Wang, L.; Luo, J.; Maye, M. M.; Fan, Q.; Rendeng, Q.; Engelhard, M. H.; Wang, C.; Lin, Y.; Zhong, C.-J., *J. Mater. Chem.* 2005, 15, (18), 1821-1832.

36. Dahal, N.; Chikan, V.; Jasinski, J.; Leppert, V. J., *Chem. Mater.* 2008, 20, (20), 6389-6395.

37. Robinson, J. T.; Evans, P. G.; Liddle, J. A.; Dubon, O. D., *Nano Lett.* 2007, 7, (7), 2009-2013.

38. Baumann, F. H.; Schroter, W., *Phys. Rev. B* 1991, 43, (8), 6510-6519.

39. Hiraki, A.; Nicolet, M. A.; Mayer, J. W., *Appl. Phys. Lett.* 1971, 18, (5), 178-181.

40. Paulose, M.; Varghese, O. K.; Grimes, C. A., *J. Nanosci. and Nanotech.* 2003, 3, (4), 341-346.

41. Wolffenbuttel, R. F., *Sensors and Actuators A* 1997, 62, (1-3), 680-686.

42. Zichichi, A., *Silicides Fundamentals and Applications,World Scientific Publishing Co.Pte.Ltd. Singapore*. 2000.

43. Ashtikar, M. S.; Sharma, G. L., *Jap. J. Appl. Phys.* 1995, 34, (10), 5520-5526.

44. Cates, M.; Miller, D. R., *Phys. Rev. B* 1983, 28, (6), 3615.

45. Hiraki, A.; Kim, S. C.; Imura, T.; Iwami, M., *Jap. J. Appl. Phys.* 1979, 18, (9), 1767-1772.

46. Sundaravel, B.; Sekar, K.; Kuri, G.; Satyam, P. V.; Dev, B. N.; Bera, S.; Narasimhan, S. V.; Chakraborty, P.; Caccavale, F., *Appl. Surf. Sci.* 1999, 137, (1-4), 103-112.

47. Prabhakaran, K.; Sumitomo, K.; Ogino, T., *Appl. Phys. Lett.* 1996, 68, (9), 1241-1243.

48. Brause, M.; Braun, B.; Ochs, D.; Maus-Friedrichs, W.; Kempter, V., *Surf. Sci.* 1998, 398, (1-2), 184-194.

49. Kishi, K.; Ikeda, S., *J. Phys. Chem.* 1974, 78, (2), 107-112.

50. Comrie, C. M.; Falepin, A.; Richard, O.; Bender, H.; Vantomme, A., *J. Appl. Phys.* 2004, 95, (5), 2365-2370.

51. Khalfaoui, R.; Benazzouz, C.; Guittoum, A.; Tabet, N.; Tobbeche, S., *Vacuum* 2006, 81, (1), 45-48.

52. Tsaur, B. Y.; Mayer, J. W., *Philo. Magazine A* 1981, 43, (2), 345 - 361.

53. [77].

54. Esaka, F.; Yamamoto, H.; Matsubayashi, N.; Yamada, Y.; Sasase, M.; Yamaguchi, K.; Shamoto, S.; Magara, M.; Kimura, T., *Appl. Surf. Sci.* 256, (10), 3155-3159.

55. Miquita, D. R.; Gonzalez, J. C.; da Silva, M. I. N.; Rodrigues, W. N.; Moreira, M. V. B.; Paniago, R.; Ribeiro-Andrade, R.; Magalhaes-Paniago, R.; Pfannes, H. D.; de Oliveira, A. G., *J. Vacuum Sci. Technol. A* 2008, 26, (5), 1138-1148.

56. Egert, B.; Panzner, G., *Phy. Rev. B* 1984, 29, (4), 2091.

57. Alayoglu, S.; Nilekar, A. U.; Mavrikakis, M.; Eichhorn, B., *Nat. Mater.* 2008, 7, (4), 333-338.

58. Pastor, C. J.; Limones, C.; Hinarejos, J. J.; Garcia, J. M.; Miranda, R.; GomezGoni, J.; Ortega, J. E.; Abruna, H. D., *Surf. Sci.* 1996, 364, (1), L505-L510.

59. Hara, S.; Izumi, S.; Kumagai, T.; Sakai, S., *Surf. Sci.* 2005, 585, (1-2), 17-24.

60. Palasantzas, G.; Vystavel, T.; Koch, S. A.; De Hosson, J. T. M., *J. Appl. Phys.* 2006, 99, (2).

61. Green, A. K.; Bauer, E., *J. Appl. Phys.* 1976, 47, (4), 1284-1291.

62. Yoshitake, T.; Yatabe, M.; Itakura, M.; Kuwano, N.; Tomokiyo, Y.; *Appl. Phys .Lett.* 2003, 83, (15), 3057-3059.

63. Wan, Q.; Wang, T. H.; Lin, C. L., *Appl. Phys. Lett.* 2003, 82, (19), 3224-3226.

64. Udono, H.; Kikuma, I., *Jap. J. Appl. Phys.* 2001, 40, (3A), 1367-1369.

65. Pan, S. S.; Ye, C.; Teng, X. M.; Fan, H. T.; Li, G. H., *Phys. Status Solidi A* 2007, 204, (10), 3316-3320.

66. Muret, P.; Ali, I.; Brunel, M., *Semicond. Sci. Technol.* 1998, 13, (10), 1170-1179.

67. Liu, Z.; Osamura, M.; Ootsuka, T.; Kuroda, R.; Makita, Y.; Tanoue, H.; Fukuzawa, Y.; Otogawa, N.; Nakayama, Y., *Thin Solid Films* 2006, 515, (4), 1532-1538.

68. Kakemoto, H.; Makita, Y.; Sakuragi, S.; Tsukamoto, T., *Jap. J. Appl. Phys.* 1999, 38, (9A), 5192-5199.

69. Datta, A.; Kal, S.; Basu, S.; Nayak, M.; Nath, A. K., *J. Mater. Sci.* 1999, 10, (9), 627-631.

70. Bayazitov, R. M.; Batalov, R. I., *J. Phys-Cond. Matter* 2001, 13, (5), L113-L118.

71. Brotherton, S. D.; Bradley, P.; Gill, A., *J. Appl. Phys.* 1985, 57, (6), 1783-1790.

72. Liu, Z., Wang, S., Otogawa, N., Osamura, M., Ootsuka, T., Mise, T., Suzuki, Y., Fukuzawa, Y., Nakayama, Y.,Tanoue, H., Makita, Y., *3rd World conference on Photovoltaic Energy Conversion May 11-18, 2003 Osaka, Japan* 2003, poster 126-129.